Maximizing power output of heat engines through design optimization: Geothermal power plants and novel exhaust heat recovery systems

Thèse

Noémie Chagnon-Lessard

Doctorat en génie mécanique
Philosophiæ doctor (Ph. D.)

Québec, Canada

© Noémie Chagnon-Lessard, 2020

Maximizing power output of heat engines through design optimization: Geothermal power plants and novel exhaust heat recovery systems

Thèse

Noémie Chagnon-Lessard

Sous la direction de :

François Mathieu-Potvin, directeur de recherche
Louis Gosselin, codirecteur de recherche

Résumé

Le design de machines thermiques menant à une puissance maximale dépend souvent des températures de la source chaude et de la source froide. C'est pourquoi dégager des lignes directrices à partir des designs optimaux de ces machines selon diverses températures d'opération peut faciliter leur conception. Une telle étude est proposée par cette thèse pour deux types de systèmes thermiques.

En premier lieu, le cycle de Rankine organique (ORC) est un cycle thermodynamique de puissance utilisé entre autres dans les centrales géothermiques exploitant des réservoirs à basse température. Depuis quelques années, ce type de centrales suscite un vif intérêt à travers le monde, étant un des modes de production de puissance parmi les plus respectueux de l'environnement. Il s'agit de pomper un géofluide du sol pour transférer sa chaleur à un fluide de travail qui opère en cycle fermé, et de le réinjecter ensuite dans le bassin géologique. Les chercheurs tentent actuellement de mieux caractériser le potentiel géothermique de divers environnements géologiques. Le sous-sol du Québec est relativement froid, alors des études essaient de déterminer s'il serait possible d'y exploiter de manière rentable des centrales géothermiques. Une autre question de recherche importante est de savoir, pour un contexte donné, quel est le design optimal d'une centrale géothermique et quelle est la puissance que l'on peut espérer produire.

Pour répondre à cette question, les cycles de Rankine organiques de base (de type sous-critique ou transcritique) sont dans un premier temps simulés et optimisés pour des températures du géofluide de 80 à 180°C et pour des températures de condensation du fluide de travail de 0.1 à 50°C. Trente-six (36) fluides pures sont investigués pour toutes les combinaisons de températures.

Par la suite, des cycles de Rankine organiques plus avancés sont aussi investigués (ajout d'une tour de refroidissement, d'un système de récupération, et d'une contrainte sur la température de réinjection du géofluide). Les ORCs avec deux pressions de chauffage sous-critique et transcritique sont aussi simulés et optimisés. Les optimisations sont faites pour

20 fluides de travail selon la même plage de température du géofluide et selon des températures du thermomètre mouillé de l’air ambient de 10 à 32°C.

En second lieu, le cycle de Brayton inversé (IBC) est un cycle thermodynamique qui pourrait être utilisé comme système de récupération de la chaleur perdue dans les gaz d’échappement de moteurs. Il s’agit d’un cycle ouvert comprenant dans sa configuration de base une turbine à gaz, un échangeur de chaleur et un compresseur. Il existe une configuration où l’eau qui se condense lors du refroidissement des gaz est évacuée avant le compresseur pour réduire le débit massique et améliorer le rendement global du système. Le Powertrain and Vehicle Research Centre (PVRC) de l’University of Bath s’est intéressé à savoir si certaines variantes de l’IBC découlant de cette configuration seraient des options viables.

Ces variantes ont mené à la création de trois nouveaux cycles thermodynamiques couplant l’IBC avec (i) une turbine à vapeur, (ii) un cycle de réfrigération, et (iii) ces deux ajouts. En comptant les deux cycles déjà existants décrits au paragraphe précédent, cinq configurations de l’IBC sont simulées et optimisées pour des températures de gaz d’échappement de 600 à 1200 K et températures de la source froide de 280 à 340 K.

La finalité de cette thèse est d’offrir un outil aidant les ingénieurs à concevoir les systèmes introduits précédemment (ORC et IBC) de sorte qu’ils aient un travail spécifique net maximisé. Sous forme d’un ensemble de diagrammes, cet outil peut ainsi être utilisé pour une large plage de température de la source chaude (géofluide ou gaz d’échappement) et de température de la source froide.

Abstract

Heat engines design leading to maximum power output often depends on the hot source temperature and the cold source temperature. This is why drawing guidelines from optimal designs of these machines according to diverse operating temperatures may facilitate their conception. Such a study is proposed by this thesis for two types of heat engines.

In the first instance, the Organic Rankine Cycle (ORC) is a power thermodynamic cycle used among others in geothermal power plants exploiting low-temperature reservoirs. This type of power plants raises keen interest around the world for being one the most environmentally friendly power production modes. In these power plants, a geofluid is pumped from the ground to transfer its heat to a working fluid operating in a closed cycle. The geofluid is then reinjected in the geological basin. Researchers are currently attempting to characterize in a better way the geothermal potential of diverse geological environments. Considering the province of Québec's relatively cold underground, studies try to determinate whether it is possible to profitably operate geothermal power plants. Another important research question is to determine, for a given context, the optimal geothermal power plant design, and the amount of power that could be generated.

To answer this question, Organic Rankine Cycles (subcritical and transcritical) are first simulated and optimized for geofluid temperatures from 80 to 180°C and for condensing temperatures of the working fluid from 0.1 to 50°C. Thirty-six (36) pure fluids are investigated for each temperature combination.

Next, cycles models are improved by adding a cooling tower, a recuperative system and a constraint on the minimum reinjection temperature. ORCs with dual-pressure heater are simulated and optimized as well. Optimization runs are performed considering 20 working fluids for the same range of geofluid temperature and for ambient air wet bulb temperature from 10 to 32°C.

In the second instance, the Inverted Brayton Cycle (IBC) is a thermodynamic cycle that could be used as a waste heat recovery system for engines exhaust gases. This is an open

cycle which includes a gas turbine, a heat exchanger and a compressor as a basic layout. There is a configuration where the water condensed during the cooling of the gases is evacuated upstream of the compressor in order to reduce the mass flow rate and improve the system global efficiency. The Powertrain and Vehicle Research Centre (PVRC) of the University of Bath is interested in finding out whether particular IBC variants arising from this configuration could be viable options.

These variants led to the creation of three novel thermodynamic cycles that couple the IBC with (i) a steam turbine, (ii) a refrigeration cycle, and (iii) both additions. Including both already existing cycles described in the preceding paragraph, five IBC layouts are simulated and optimized for exhaust gases temperatures from 600 to 1200 K and for heat sink temperatures from 280 to 340 K.

The purpose of this thesis is to offer a tool that help engineers designing the systems previously introduced (ORC and IBC), so that they produced a maximized specific work output. As a set of charts, this tool can be used for a large range of hot source temperature (geofluid or exhaust gases) and of heat sink temperature.

Contents

Table contents

Figure contents

Nomenclature

Variables

c_p	specific heat, $\text{kJ kg}^{-1}\ \text{K}^{-1}$
F	fluid
h	enthalpy, kJ kg^{-1}
h_f°	enthalpy of formation, kJ kg^{-1}
M	molar mass, g mol^{-1}
$\dot{m}$	mass flow rate, kg s^{-1}
mf	mass fraction
N	number of moles, mol
P	pressure, kPa
q	specific heat transfer rate, kJ kg^{-1}
$\dot{Q}$	heat transfer rate, kW
R	gas constant, $\text{kJ kg}^{-1}\ \text{K}^{-1}$
s	entropy, $\text{kJ kg}^{-1}\ \text{K}^{-1}$
s_f°	entropy of formation, $\text{kJ kg}^{-1}\ \text{K}^{-1}$
sh	specific humidity
T	temperature, °C, K
U_R	refrigeration utilization rate
V	volume, m^3
W	work, kJ
w	specific power output or specific work output, kJ kg^{-1}
x	vapor quality
y	molar fraction

Greek letters

ε	heat exchanger effectiveness
ϕ	relative humidity
η	efficiency
ρ	density

Subscripts

atm	atmospheric
B	Baumann
b	brine
bf	best-fit
c	condenser
cr	critical
db	dry bulb
env	environment
f,g	saturated liquid and saturated gas states
fg	evaporation (change form liquid to vapor)
H	high pressure
hex	heat exchangers
i	stage number, species
in	inlet
j	increment
j	iteration number
liq	liquid state
M	medium pressure
$\max$	maximum
$\min$	minimum
opt	optimal
out	outlet
pp	pinch point
ref	reference
s	isentropic
sat	saturated
sw	supplied liquid water
tol	tolerance
tot	total
vap	vapor state
w	cooling fluid

wb	wet bulb
wf	working fluid

Abbreviations

CO	condenser
CP	compressor
D	dual-pressure heater
D	related to drainage
EC	economizer
EV	evaporator
HE	heat exchanger
HP	high pressure
GT	gas turbine
IBC	Inverted Brayton Cycle
IC	internal combustion
MP	medium pressure
ORC	Organic Rankine Cycle
PP	pump
R	related to refrigeration cycle
RE	recuperator
S	single-pressure heater
S	related to open Rankine cycle
SC	subcritical
SH	superheater
ST	steam turbine
TB	turbine
TC	transcritical cycle
VA	valve
WCT	wet cooling tower

Personne n'ignore que la chaleur peut être la cause du mouvement, qu'elle possède même une grande puissance motrice : les machines à vapeur, aujourd'hui si répandues, en sont une preuve parlant à tous les yeux. […] Développer cette puissance, l'approprier à notre usage, tel est l'objet des machines à feu. L'étude de ces machines est du plus haut intérêt, leur importance est immense, leur emploi s'accroit tous les jours. Elles paraissent destinées à produire une grande révolution dans le monde civilisé.

- Sadi Carnot, 1824

It is time that we engineers reclaim our own field – thermodynamics – so that we may expand its deterministic powers in the direction of naturally organized, living and not living systems. We are the ones to do this work because nature is engineered.

- Adrian Bejan, 1996

Remerciements

La première personne qui a rendu possible cet accomplissement est celle qui l'a initiée. Merci à Louis Gosselin, mon codirecteur, pour m'avoir tout bonnement proposé une maîtrise lorsque j'étais allée lui quémander de l'aide à l'été 2013 dans le cadre de mon stage au REGAL. Merci de m'avoir fait confiance malgré mes notes du baccalauréat, et de m'avoir laissé choisir le projet qui était le moins sûr de fonctionner. À l'entente du mot géothermie, il était impossible de me faire changer d'avis !

La deuxième personne que je tiens à remercier est mon directeur François Mathieu-Potvin. Ton écoute, ta perspicacité et ta rigueur m'ont toujours fait sentir bien encadrée et apte à faire le travail nécessaire. Nos réunions n'ont pas seulement servi à faire le suivi des avancements et répondre à mes questions. Elles se sont aussi traduites en discussions enrichissantes sur le « comment » et le « pourquoi » de curieux phénomènes physiques. En fin de compte, mon projet est devenu un terrain de jeu où tout était possible pour satisfaire ma curiosité insatiable sur la thermodynamique. François et Louis, vous avez été les meilleurs directeurs qui soient : compétents, respectueux, drôles, compréhensifs et motivants.

Merci à mes parents Sylvie et Denis pour avoir toujours été là pour moi. Dans mes moments de « syndrome de l'imposteur », vous m'avez fait sentir que j'étais assez intelligente, assez compétente pour mériter le titre de « docteur » en génie mécanique. Vous êtes également des modèles pour moi et m'avez appris à développer ma pensée critique, à persévérer et à garder l'esprit ouvert.

Merci à Laurent, mon partenaire de vie que j'ai rencontré à mi-parcours de cette (longue) étape de vie. Ta bonne humeur, tes encouragements, les soirs où tu as fait la vaisselle tout seul, et tes bruits de chèvre m'ont clairement aidé à passer au travers, surtout pendant les derniers miles. Merci de m'avoir écoutée et rappelée à l'ordre après la catastrophe du concours de vulgarisation et la réception des innombrables commentaires des évaluateurs du deuxième article (chapitre 3 de la thèse).

Merci à Mireille, qui était en rédaction en même temps que moi, et avec qui j'ai pu me changer les idées et partager mes inquiétudes par rapport aux études graduées. Sans elle, je n'aurais sûrement pas eu la motivation de travailler autant les soirs et les fins de semaine.

Dans un autre ordre d'idées, ce projet a été financé par l'Institut de recherche d'Hydro-Québec (IREQ) et par le Conseil de recherches en sciences naturelles et en génie du Canada (CRSNG). De plus, le programme des Bourses canadiennes du jubilé de diamant de la reine Elizabeth II (BRE) et le Bureau international de l'Université Laval (BI) m'ont donné des bourses qui m'ont permis d'effectuer un stage de recherche à l'University of Bath durant l'été 2017. J'aimerais souligner l'apport de Colin Copeland qui m'a supervisé durant ce stage et m'a offert d'ajouter à ma thèse un axe de recherche très intéressant.

Avant-propos

Cette thèse présente les travaux de recherche réalisés lors de la maîtrise et du doctorat en génie mécanique de mai 2014 à juillet 2019. Le passage accéléré au doctorat a été effectué à l'été 2016. Les différents sujets abordés sont mis en contexte dans l'introduction, suivi de leurs objectifs respectifs. Trois publications pour des journaux scientifiques internationaux (Chapitres 1, 2 et 3) forment le corps de la thèse. Ils sont listés ci-dessous, avec des informations concernant leur statut de publication en date du 7 février 2020, leur contexte de recherche, mes contributions et les modifications par rapport à la version publiée.

CHAPITRE 1 :

N. Chagnon-Lessard, F. Mathieu-Potvin and L. Gosselin, "Geothermal power plants with maximized specific power output: Optimal working fluid and operating conditions of subcritical and transcritical Organic Rankine Cycles," *Geothermics*, vol. 64, pp. 111–124, DOI: 10.1016/j.geothermics.2016.04.002, Novembre 2016 (publié).

<u>Notes</u> : Article rédigé par N. Chagnon-Lessard (moi-même) et F. Mathieu-Potvin et révisé par L. Gosselin. Le travail a été réalisé sous la supervision de F. Mathieu-Potvin et L. Gosselin au Laboratoire de Transfert Thermique et d'Énergétique (LaTTÉ) de l'Université Laval. J'ai participé à l'élaboration des modèles de cycles thermodynamiques et à l'analyse d'ordre de grandeur. J'ai écrit les scripts de simulation numérique sur MATLAB, effectué les optimisations et réalisé les figures. Finalement, j'ai aidé à dégager les conclusions. Les modifications par rapport à la version publiée concernent le changement de système de références pour l'uniformisation de la thèse et quelques changements mineurs.

CHAPITRE 2 :

N. Chagnon-Lessard, F. Mathieu-Potvin and L. Gosselin, "Optimal design of geothermal power plants: A comparison of single-pressure and dual-pressure organic Rankine cycles," *Geothermics*, vol. 86, DOI: 10.1016/j.geothermics.2019.101787, Juillet 2020 (disponible en ligne).

Notes : Article rédigé par N. Chagnon-Lessard (moi-même) et révisé par L. Gosselin et F. Mathieu-Potvin. Le travail a été réalisé sous la supervision de F. Mathieu-Potvin et L. Gosselin au LaTTÉ de l'Université Laval. J'ai élaboré les modèles de cycles, écrit les scripts de simulation numérique et d'optimisation sur MATLAB, effectué les optimisations, réalisé les figures et dégagé les conclusions. Les modifications par rapport à la version publiée concernent le changement de système de références pour l'uniformisation de la thèse et certaines sections conservées de la première version soumise.

CHAPITRE 3 :

N. Chagnon-Lessard, C. Copeland, F. Mathieu-Potvin and L. Gosselin, "Maximizing specific work output extracted from engine exhaust with novel inverted Brayton cycles over a large range of operating conditions" *Energy*, vol. 191, DOI: 10.1016/j.energy.2019.116350, Janvier 2020 (publié).

Notes : Article rédigé par N. Chagnon-Lessard (moi-même) et révisé par l'ensemble des co-auteurs. Le travail a été réalisé en premier lieu sous la supervision de C. Copeland au Powertrain and Vehicle Research Center (PVRC), lors d'un stage à l'University of Bath au Royaume-Uni. Il a ensuite été complété sous la supervision de F. Mathieu-Potvin et L. Gosselin au LaTTÉ de l'Université Laval. L'article se base sur des cycles déjà existants dans la littérature et propose des nouvelles variantes. C. Copeland a proposé ces variantes originales et j'ai aidé à améliorer leur concept. J'ai écrit les scripts de simulation numérique et d'optimisation sur MATLAB, effectué les optimisations, réalisé les figures et participé à tirer les conclusions. La version présentée comprend les modifications apportées après la révision par les évaluateurs. Cependant, la version publiée a été écourtée pour répondre aux exigences de l'éditeur. Il s'agit donc de la version antérieure à la réduction du nombre de mots.

Introduction

Mise en contexte

L’énergie est un pilier sur lequel repose notre société. Afin de réduire son coût et son impact sur l’environnement, de plus en plus d’efforts sont consacrés à améliorer la manière dont elle est convertie. La chaleur est une importante forme d’énergie permettant de produire de l’énergie mécanique pouvant directement servir dans l’industrie et comme moyen de déplacement ou pour être ensuite convertie en électricité par des centrales thermiques. Les efforts de recherche se concentrent entre autres sur les modes alternatifs de production d’électricité, ainsi que sur des systèmes permettant de récupérer la chaleur perdue lors de procédés impliquant une conversion d’énergie.

Les normes de plus en plus sévères sur la réduction des gaz à effet de serre ouvrent la voie au développement de centrales électriques plus propres. Parmi les options sérieusement considérées et déjà implémentées dans certaines parties du monde se trouve la production d’électricité à partir de réservoirs géothermiques à basse température. L’exploitation de la chaleur de la Terre à haute température se fait de manière efficace avec l’utilisation de centrales géothermiques de types « flash » et « dry », notamment en Islande et en Californie, régions comportant des bassins naturels d’eau chaude à haute pression sous forme liquide ou gazeuse. Pour les régions ayant un sous-sol à plutôt basse température (en bas de 200°C), il est parfois impraticable d’exploiter une centrale géothermique de manière rentable, compte tenu de l’état actuel des connaissances.

Au Canada en 2019, il n’y a pas encore de centrale géothermique en opération. En effet, la majorité de son territoire comporte des roches chaudes, mais elles sont à plusieurs kilomètres de profondeur. Il faudrait donc recourir à la géothermie profonde stimulée par fracturation hydraulique pour exploiter cette ressource énergétique. Afin de développer les connaissances et expertises nécessaires à la réalisation d’un projet expérimental sur la géothermie profonde au Québec, l’Institut de recherche d’Hydro-Québec (IREQ) a initié le projet intitulé *Intégration de la géothermie profonde dans le portefeuille énergétique canadien*. Bénéficiant du financement du programme Initiative écoÉnergie sur l’innovation du gouvernement du Canada, ce projet multidisciplinaire concerne l'évaluation et l'exploration des ressources géothermiques, l'ingénierie des réservoirs, les aspects sociaux et environnementaux, la fracturation et l'ingénierie de la production de puissance [1].

Dans le cadre de cette initiative, l'aspect de la production de puissance s'articule autour du projet INGÉOPRO : *Développement de modèles avancés pour l'ingénierie de la production de la puissance à partir de la géothermie profonde*. Le volet A de ce projet s'intéresse à la simulation numérique et l'optimisation de centrales géothermiques. Les questions apportées par ce projet sont :

a) Quels sont les types de centrales géothermiques les mieux adaptés aux conditions de la province de Québec ?
b) Quelles sont les meilleures configurations de centrales ?
c) Quels sont les paramètres d'opération optimaux de la centrale, et ce, pour les diverses possibilités de température de l'eau géothermale ?
d) À quelles valeurs de puissance nette produite devrait-on s'attendre en considérant le climat froid de la province ?

En effet, puisque les cycles thermodynamiques utilisés pour convertir la chaleur à basse température s'avèrent relativement inefficaces, le choix du modèle de centrale est crucial. Dans le présent cas, il faut fracturer le sol pour y injecter un fluide géothermique (« brine » en anglais, ou géofluide en français) sous pression pour recevoir la chaleur de la roche sèche en se déplaçant du puits d'injection aux puits de récupération. Le géofluide entre ensuite dans une centrale dite « binaire » pour transférer sa chaleur à un fluide de travail qui effectue un cycle thermodynamique fermé de puissance, et est ensuite réinjecté dans le sol.

Le cycle de puissance en question peut être choisi parmi plusieurs options. Cependant, seulement deux sont typiquement considérés aptes à être appliqués à la géothermie [2] : le cycle de Kalina [3] et le cycle de Rankine organique. Le cycle de Kalina est un cycle combiné utilisant un mélange eau-ammoniac qui s'évapore et se condense avec un important glissement de température [4], c'est-à-dire avec une hausse/baisse de température pendant un changement de phase liquide-gaz. Cependant, le cycle de Rankine organique lui est préféré dans ce projet puisque qu'il a une performance énergétique généralement plus élevé pour des réservoirs à basse température [5] et comporte un vaste choix de fluides de travail pouvant être étudiés.

Le cycle de Rankine, un cycle thermodynamique se rapprochant du cycle de Carnot [6], correspond à une centrale thermique élémentaire [7] utilisant habituellement l'eau comme fluide moteur. Il comprend quatre composantes de base : (i) une pompe pour amener l'eau à la pression désirée, (ii) une chaudière (ou échangeur de chaleur) pour chauffer et évaporer l'eau à pression constante, (iii) une turbine à vapeur qui détend l'eau gazeuse, et (iv) un condenseur qui évacue la chaleur latente de l'eau à pression constante. L'utilisation de fluides organiques comme le R134a au lieu de l'eau permet d'exploiter une source de chaleur à plus basse température de manière plus efficace grâce à leur température d'ébullition généralement plus faible [8]. Le cycle se nomme alors le cycle de Rankine organique, ou ORC (Organic Rankine Cycle). La première centrale géothermique comportant un ORC a été construite en 1967 dans la Kamchatka Peninsula en Russie et utilisait le R12 comme fluide de travail [9].

Selon les dernières études sur le sujet ainsi qu'en se basant sur les centrales en opération à travers le monde, la question (a) est répondue d'emblée par la centrale binaire comportant un ORC. Cependant les questions (b), (c) et (d) requièrent une étude plus approfondie. Le rendement thermique de l'ORC étant tout de même plutôt faible, le design de la centrale doit être soigneusement optimisée pour produire un maximum de puissance et être économiquement viable. Le design comprend la configuration du cycle, les paramètres d'opérations (pressions et débits par exemple) et le choix du fluide de travail.

Les questions apportées par Hydro-Québec concernant le design optimal d'une centrale géothermique ont permis, dans le cadre de cette thèse, le développement d'une méthodologie globale d'analyse de cycle thermodynamiques (i.e., modélisation mathématique, implémentation numérique, optimisation numérique, et finalement présentation des résultats sous forme de chartes de conception). Cette méthodologie peut être appliquée à d'autres machines thermiques pour maximiser leur performance. Par exemple, le Powertrain and Vehicle Research Centre (PVRC) de l'University of Bath au Royaume-Uni s'est intéressé au Cycle de Brayton Inversé (IBC pour Inverted Brayton Cycle) comme alternative au turbo chargeur. L'IBC est un cycle ouvert qui utilise la chaleur des gaz de produits de combustion afin de créer de la puissance mécanique. L'IBC comporte trois composantes principales (une turbine à gaz, un échangeur de chaleur et un compresseur), et diverses variantes peuvent être appliquées à cette configuration de base. Des questions similaires à celles postulées pour les centrales géothermiques sont soulevées :

e) Quels sont les types de système IBC les mieux adaptés aux diverses températures possibles des gaz d'échappement et du puits de chaleur ?
f) Quelles sont les meilleures configurations du système IBC ?
g) Quels sont les paramètres d'opération optimaux du système IBC, et ce, pour les diverses possibilités de températures d'opération ?
h) À quelles valeurs de puissance nette produite devrait-on s'attendre en considérant les diverses possibilités de températures d'opération ?

Les questions pour les systèmes IBC (questions e à h) sont similaires aux questions pour les centrales géothermiques (questions a à d), et elles pourront donc être traitées par la même méthodologie dans le cadre de cette thèse.

Objectifs

L'objectif principal de cette thèse est d'offrir un outil permettant aux ingénieurs de concevoir des systèmes de récupération de la chaleur présentant un travail spécifique net maximisée. Sous forme d'un ensemble de diagrammes, cet outil peut être utilisé pour une large plage de température de la source chaude (géofluide ou gaz d'échappement) et de température du puits de chaleur (la source froide). La thèse se concentre sur deux axes :

A1 : Le cycle de Rankine organique (ORC) employé dans une centrale géothermique

A2 : Le cycle de Brayton inversé (IBC) employé comme système de récupération de la chaleur des gaz d'échappement d'un moteur

Les objectifs secondaires communs aux deux axes sont les suivants :

1. Simuler numériquement plusieurs configurations pour chacun des cycles thermodynamiques avec le logiciel MATLAB.
2. Optimiser le design des cycles pour maximiser leur travail spécifique net selon une large gamme de température de la source chaude et une large gamme de température de la source froide.
3. Organiser les résultats sous forme de diagrammes présentant le travail spécifique net maximisé et les variables de design optimisées.
4. Déterminer les variantes des cycles les plus performantes en fonctions des températures d'opération.

Les objectifs spécifiques à l'axe 1 sont :

A1.1. Développer de nouvelles corrélations permettant de prédire le travail spécifique net d'une centrale géothermique avec ORC.

A1.2. Évaluer l'impact de la charge auxiliaire (pompes et système de refroidissement) sur le travail spécifique net en fonction des températures d'opération.

Finalement, les objectifs spécifiques à l'axe 2 sont :

A2.1 Comparer la performance des nouveaux IBCs avec celle des meilleurs systèmes utilisés à ce jour pour récupérer la chaleur des gaz d'échappement de moteurs.

A2.2 Déterminer les applications les plus appropriées pour ces nouveaux cycles.

CHAPITRE 1. GEOTHERMAL POWER PLANTS WITH MAXIMIZED SPECIFIC POWER OUTPUT: OPTIMAL WORKING FLUID AND OPERATING CONDITIONS OF SUBCRITICAL AND TRANSCRITICAL ORGANIC RANKINE CYCLES

1.1. Résumé

Dans cet article, la conception d'un cycle de Rankine organique (ORC) est optimisée au moyen de simulations numériques. Les systèmes d'intérêt sont les cycles thermodynamiques sous-critique et transcritique. Des optimisations sont exécutées avec l'objectif de déterminer la conception maximisant le travail spécifique net. Les variables de design incluent les paramètres d'opération (pressions, débits massiques), et les meilleurs fluides de travail sont déterminés en comparant la performance de 36 réfrigérants. Les optimisations sont réalisées pour une large gamme de températures du géofluide (de 80 à 180°C), et pour une large gamme de température de condensation (de 0.1 à 50°C). Les résultats sont consignés sous forme de diagrammes pouvant être utilisés comme des outils efficaces pour concevoir des centrales géothermiques optimales. Finalement, une analyse d'ordre de grandeur a permis de développer des nouvelles corrélations pour prédire le travail spécifique net maximal d'un ORC.

1.2. Abstract

In this paper, the design of an Organic Rankine Cycle (ORC) is optimized by means of numerical simulations. The systems of interest are the subcritical and transcritical thermodynamic cycles. Optimizations are performed with the objective of determining the design that maximizes the specific power output. The design variables include the operating parameters (pressures, mass flow rates), and the best working fluid is determined by comparing the performance of 36 refrigerants. Optimization runs are performed for a wide range of geofluid temperatures (from 80 to 180°C), and for a wide range of condenser temperature (from 0.1 to 50°C). The results are summarized in charts that may be used as efficient tools for designing optimal geothermal power plants. Finally, an approximate analysis allowed to develop new correlations for predicting the maximal specific power output of an ORC.

1.3. Introduction

The energy sector raises important issues in modern societies. With growing demand, depletion of fossil fuel reserves and global warming, more and more efforts are devoted to the development of renewable sources of energy. Among the various solutions, geothermal energy is one of the candidates for reducing GES emissions in the context of power generation. Indeed, the exploitation of the Earth's heat could provide 3.5% of the global generated electricity by 2050, according to the International Energy Agency. The race to secure and diversify the energy portfolio paves the way to Organic Rankine Cycle (ORC) geothermal power plants using low-temperature reservoirs.

Organic Ranking Cycles have a relatively low thermodynamic efficiency, and as a consequence, their designs must be carefully optimized to be economically viable. Indeed, Organic Rankine Cycles have been the subject of several studies in literature. For example, Wei et al. [10] analysed and optimized an ORC system using HFC-245fa as a working fluid. Dai et al. [11] optimized the performance of ORC with 10 different working fluids, for a single fixed value of heat source temperature. A multicriteria approach has been used by Toffolo et al. [12] in order to perform the optimal selection of design parameters in ORC. The impact of turbine efficiency on ORC net power output calculations was investigated by Pan and Wang [5]. Binary ORC power plants exploiting low-temperature geothermal heat sources have been studied through design analysis [13]; [14]; [15] and through design optimization [16], [17], [18]. A comparison of a few working fluids was performed by Hung [19] and also by Drescher and Brüggemann [20]. Transcritical cycles are analysed for a case of high brine inlet temperature using three working fluids in [21]. A transcritical cycle using R125 is compared with three other fluids in subcritical cycle for a case with low brine temperature in [22]. Performance and economical comparison of optimized subcritical and transcritical cycles is made in [23] using 12 working fluids for one low brine temperature. An exhaustive review of thermodynamic cycles used to perform the conversion of low-grade heat have been performed by Chen et al. [24], and a world-wide review of geothermal power plant efficiency has been done by Zarrouk and Moon [25].

By looking at the abovementioned references and in literature, it can be seen that there are few texts that provide clear guidelines or rules of thumbs to design an ORC geothermal plant providing maximal power output. However, Clarke and McLeskey Jr. [26] recently performed a multi-objective optimization of subcritical ORC geothermal power plants by considering 17 working fluids. More specifically, they identified optimal designs for three fixed values of dry air temperatures and six fixed values of brine temperatures. Their results allow to identify the best working fluid and operating conditions in order to get the highest specific power output from a geothermal power plant. Hence, it can be seen that there is a call to develop design guidelines for ORC geothermal power plants. In the present paper, the authors propose to develop new design charts for the preliminary design of geothermal power plants, by extending the work performed by Clarke and McLeskey Jr. [26]. More specifically, several additional features are included in this study, such as: (i) the investigation of transcritical cycles, (ii) the comparison of 36 different working fluids, (iii) the analyses of a continuous set of combination of condenser temperatures and brine temperatures, and (iv) the development of a new approximate theoretical approach for optimal ORC design.

The main goals of the work presented here are: (i) to develop a numerical simulation tool that predicts subcritical and transcritical ORC performance, (ii) to develop optimization algorithms to identify the best ORC designs, and (iii) to establish new charts that provide guidelines for designing optimal ORC geothermal power plants. The analysis presented in this paper covers a large set of operating conditions, i.e., a geofluid temperature from 80 to 180°C, and a condenser temperature (condensing temperature of the working fluid) from 0.1 to 50°C. The objective function to maximize is the specific power output w, and the design variables are the pressure P_2 that prevails in the heat exchangers, the mass flow rate ratio $R_{b,w}$ between the geofluid and the working fluid, and the superheater efficiency ε_{SH}. The analysis involves 36 different working fluids.

The paper is structured as follows: Section 1.4 describes the methodology for calculating the thermodynamic performance of two ORCs of interest; Section 1.5 describes the optimization problem; Sections 1.6 – 1.9 present results of the optimization runs and provide new charts for designing optimal ORC; Section 1.10 presents the development of new correlations; and finally, discussions and conclusions are provided in Sections 1.11 and 1.12.

1.4. Problem statement

A description of the thermodynamic cycles of interest is provided in this section. The systems considered in this paper are two variants of the Organic Rankine Cycles (ORC): (i) a subcritical cycle (turbine inlet pressure smaller than the working fluid critical pressure), and (ii) a transcritical cycle (turbine inlet pressure larger than the working fluid critical pressure). The subcritical and transcritical systems are illustrated in Fig. 1.1a and 1.1c, while their corresponding temperature-entropy diagrams ($T - s$) are illustrated in Fig. 1.1b and 1.1d, respectively.

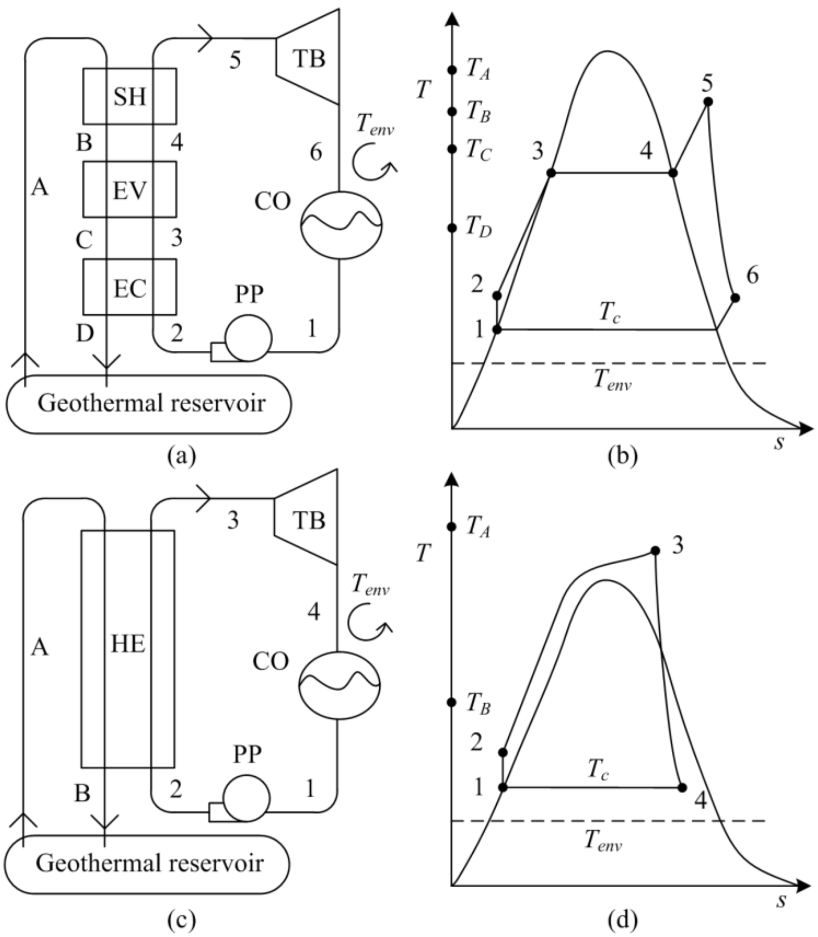

Figure 1.1. Organic Rankine Cycle designs. (a) Subcritical cycle equipment architecture. (b) Subcritical cycle thermodynamic diagram. (c) Transcritical cycle equipment architecture. (d) Transcritical cycle thermodynamic diagram.

1.4.1. *Subcritical cycle*

The subcritical ORC possesses two circuits (see Fig. 1.1a), i.e., the primary and secondary circuits. The primary circuit is dedicated to the geothermal brine. For instance, the geofluid is pumped from the reservoir and enters the plant at state {A}. Then, it passes through three heat exchangers, each with exit conditions corresponding to states {B}, {C} and {D}, respectively. It is also possible to use only one heat exchanger [27] instead of three separated heat exchangers; however, only the configuration with three heat exchangers (as shown in Fig. 1.1a) is considered in this paper. Finally, the geofluid is reinjected in the ground. It should be noticed that the geothermal fluid typically contains dissolved gas and calcite. However, it is assumed in this paper that geothermal fluid properties may be approximated as equal to those of pure water, which is in line with recent literature (e.g., [28], [29] . The geofluid is considered to remain in a compressed liquid state, and it never undergoes evaporation during the whole process. The temperature of the geofluid at states {A}, {B}, {C} and {D} are identified by black dots on the temperature axis of Fig. 1.1b for comparison purpose.

The secondary circuit (a closed loop) is dedicated to the working fluid (see states {1} to {6} in Figs. 1.1a and 1.1b). The working fluid receives heat from the primary circuit by means of three heat exchangers that act as a boiler for the working fluid. Typically, the working fluid is an organic fluid having a low boiling point, and it is made of refrigerant, alkane or other hydrocarbons [17]. The working fluid enters a pump (PP) as saturated liquid at the condenser pressure (state {1} in Fig. 1.1b), and it leaves that pump at the desired subcritical pressure (state {2}). It is then heated at constant pressure in an economizer (EC) to obtain a state of saturated liquid (state {3}). An evaporator (EV) brings the working fluid to a saturated vapor state (state {4}) and involves a thermodynamic evolution at constant temperature and constant pressure. Furthermore, a superheater (SH) provides the necessary amount of heat to reach state {5} at constant pressure. In limiting cases, states {4} and {5} can overlie, which means that the working fluid enters the turbine as saturated vapor and the superheater transfers no heat. The minimal temperature difference for heat exchange between the geofluid and the working fluid (pinch-point) has been set to be larger or equal to 5°C in the present work. After state {5}, the working fluid produces work in the turbine

(TB), and leaves it at state {6}. Finally, the fluid rejects heat to the environment at constant pressure by means of a condenser (CO), and leaves it at state {1}.

1.4.2. *Transcritical cycle*

The transcritical cycle is similar to the subcritical cycle, see Figs. 1.1c and 1.1d. The difference lies in the heat transfer between the two fluids. For instance, the hot geofluid in the primary circuit enters the plant at state {A} and transfers its heat to the working fluid through one exchanger (HE) instead of three. The cycle is equipped with only one heat exchanger because there is no definite difference between liquid and vapor phases when the working fluid is heated. The geofluid is then reinjected in the reservoir at state {B}. The relative temperature of the geofluid at states {A} and {B} are identified by black dots on the temperature axis of Fig. 1.1d for comparison purpose.

The working fluid in the secondary circuit begins its path as saturated liquid at condenser pressure (state {1} in Fig. 1.1c) and passes through a pump (PP) to obtain the desired supercritical pressure (state {2}). Then, the working fluid is heated at constant pressure by the geofluid in the heat exchanger (HE) so as to reach the turbine inlet as superheated vapor (state {3}). The fluid expands in the turbine (TB), leaves it at state {4}, and enters the condenser (CO) to reject heat to the surroundings at constant pressure. While there is no definite location for a pinch point in the heat exchanger (HE), it is required to impose a minimal temperature difference in that piece of equipment to ensure that the relative temperature of both fluids is valid for heat transfer. The method used to verify the relative temperatures in the heat exchanger is presented in Section 1.4.5.

1.4.3. *Classes of working fluids*

The working fluids used in this paper are pure fluids (i.e., no mixture) and they can be categorized by their shape in a $T - s$ diagram [24]. More specifically, fluids are labelled as “normal” when the slope of the saturation line is negative (e.g. propane) for all entropy s values larger than the entropy at the critical point (s_{cr}), see an illustration in Fig. 1.2a. On the other hand, fluids are labelled as “retrograde” when the slope of the saturation line is positive (e.g. octane) for some values of entropy s larger than the entropy at the critical point (s_{cr}), see Fig. 1.2b. The labels "normal" and "retrograde" are often used in literature (e.g., [2]). It should be noticed that other authors use the labels "wet" and "dry" instead of "normal" and "retrograde", respectively.

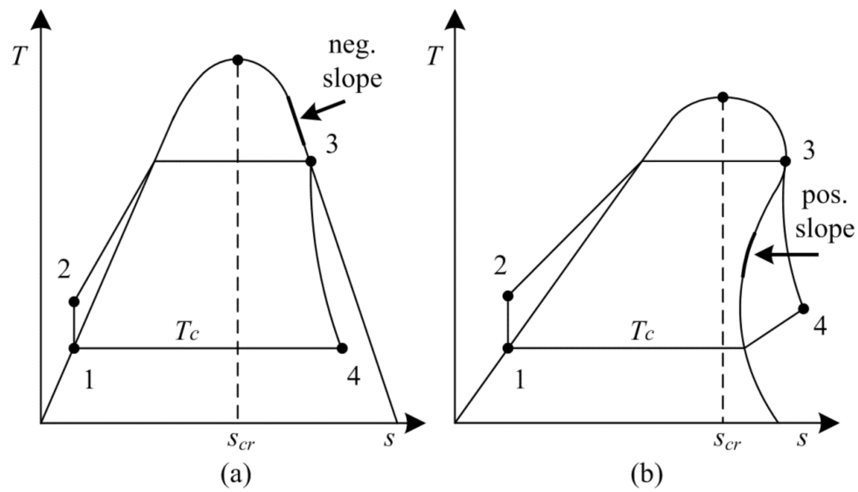

Figure 1.2. Simplified thermodynamic diagrams. (a) Normal fluid. (b) Retrograde fluid.

In practice, *normal* fluids typically have to be superheated so as to reduce liquid droplets appearance during expansion in turbines, whereas this is usually not a requirement for the *retrograde* fluids. Indeed, retrograde fluids in turbines typically remain in superheated state during expansion in turbines, as it can be seen in Fig. 1.2b. It should be emphasized that the categories "normal" or "retrograde" correspond to a fluid *property* that is independent of the thermodynamic cycle itself. The thermodynamic evolutions {1}-{2}-{3}-{4} are present in Fig. 1.2 for the sole purpose of illustrating the behaviour of the fluid in a typical turbine (between states {3} and {4}). Normal and retrograde fluids will be both considered in the analysis performed in this paper.

1.4.4. *Turbine differential modeling*

A schematic representation of the working fluid thermodynamic evolution in the turbine (between states {3} and {4}) is provided in Fig. 1.3. Notice that while that figure illustrates the use of a retrograde fluid in a transcritical cycle, the methodology explained here is also systematically used for any kind of cycles (subcritical or transcritical) and any category of fluid (normal or retrograde) investigated in this paper.

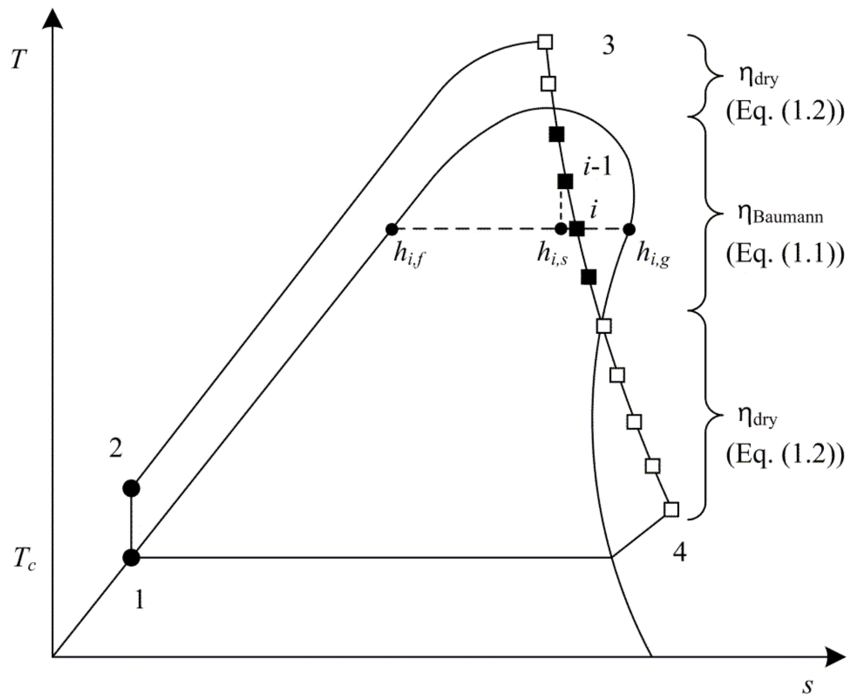

Figure 1.3. Calculation principle of turbine efficiency on thermodynamic diagram of a retrograde fluid.

It can be seen in this $T-s$ diagram that for some ranges of pressure between states {3} and {4}, the working fluid is at superheated vapor state, which requires the use of the turbines dry efficiency η_{dry} [2] for calculating the intermediary thermodynamic states in the turbine (see open squares in Fig. 1.3). However, the fluid may be in saturated mixture states for other ranges of pressure (see black squares in Fig. 1.3), which requires the use of the Baumann efficiency $\eta_{Baumann}$ [30]; [2] to take into account the decrease of the turbine efficiency due to the presence of liquid droplets (a decrease inversely proportional to the vapor quality). Thus, a method based on differential thermodynamic evolution has been developed to model the evolution from state {3} to state {4}. It consists in representing the turbine into several virtual small turbines (i.e., into several stages). Each stage has its own efficiency expression (i.e., dry efficiency or Baumann efficiency expressions), and deals with a small part $\left(\Delta P_i\right)$ of the total pressure drop $\left(P_3 - P_4\right)$. In other words, the pressure drop is discretized so as to calculate the enthalpy at the end of each stage. The liquid content is calculated at each stage, which allows to identify the appropriate efficiency expression to use.

Thus, when the fluid that enters a turbine stage i contains a saturated mixture, the enthalpy h_i at the outlet of that stage can be calculated by using the Baumann expression as follows:

$$h_i = \frac{h_{i-1} - A\left(x_i - h_{i,f} \Big/ \left(h_{i,g} - h_{i,f}\right)\right)}{1 + A \Big/ \left(h_{i,g} - h_{i,f}\right)}$$
$$A = \frac{\eta_{dry}}{2}\left(h_{i-1} - h_{i,s}\right) \tag{1.1}$$

where subscript i indicates the actual stage, and subscript $i-1$ the previous stage. The variable $h_{i,s}$ is the enthalpy after a small pressure drop when the expansion in a stage is assumed to be isentropic.

In the case where the fluid that enters a turbine stage i does not contain liquid phase, the enthalpy h_i at the outlet of that stage can be expressed as:

$$h_i = h_{i-1} - \eta_{dry}(h_{i-1} - h_{i,s}) \tag{1.2}$$

The enthalpy calculated at the last pressure stage corresponds to the enthalpy at state {4}, and it is used in the calculation of the power plant specific output power. The variables $h_{i,f}$, $h_{i,g}$ and $h_{i,s}$ are identified in Fig. 1.3.

1.4.5. *Heat exchanger modeling*

The heat transfer process in the heat exchangers has to be carefully investigated to ensure the thermodynamic and physical validity of a design. As explained earlier, it is necessary to verify the temperature of both fluids throughout the *entire* length of the heat exchanger in transcritical cycles, because there is no preferred position for the occurrence of the pinch point. Even for subcritical designs (Fig. 1.1a), the pinch point may not be located at the evaporator inlet when the pressure P_3 is close to the critical pressure. Hence, a general methodology for identifying the pinch point in the heat exchangers was developed and applied to subcritical and transcritical designs.

The idea is to represent the heat exchanger in a large number of virtual heat exchangers, each one involving a small part $d\dot{Q}$ of the total heat transfer $\dot{Q}$ (see an example of the heat exchanger in a transcritical cycle in Fig. 1.4). Then, the temperature T_b of the geofluid (subscript b for "brine") and the temperature T_w of the working fluid may be calculated at each stage i:

$$
\begin{aligned}
T_{b,i} &= T_{b,i-1} + \frac{d\dot{Q}}{\dot{m}_b c_b} \\
h_{w,i} &= h_{w,i-1} + \frac{d\dot{Q}}{\dot{m}_w} \\
T_{w,i} &= T\left(h_{w,i}, P_{hex}\right)
\end{aligned}
\tag{1.3}
$$

where subscript i indicates the actual stage, subscript $i-1$ the previous stage, $d\dot{Q}$ the differential heat transfer, and P_{hex} the pressure in the heat exchangers. The variable c_b is the liquid specific heat of the geofluid, $\dot{m}_b$ the brine mass flow rate and $\dot{m}_w$ the working fluid mass flow rate. With this approach, it is possible to identify the pinch-point temperature difference ΔT_{pp}, and to verify the constraint associated to that parameter (i.e., ΔT_{pp} must be larger or equal than 5°C). That method was used for analysing heat transfer in the heat exchangers shown in Figs. 1.1a and 1.1c.

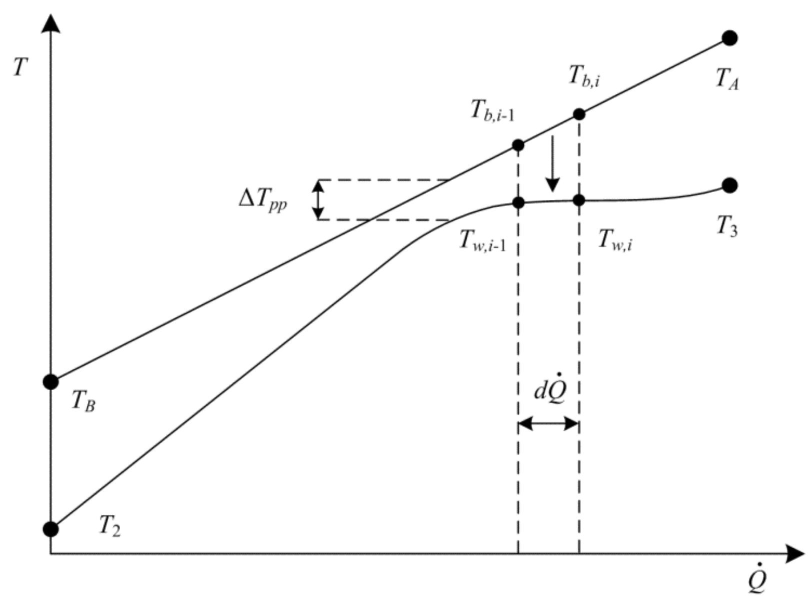

Figure 1.4. Temperature evolution of both fluids in heat exchangers.

1.4.6. *Numerical simulations*

Several numerical tools exist for simulating thermodynamic cycles, such as AxCYCLE™ [31] or Thermoptim™ [4], and many software allow the calculation of thermodynamic properties, such as CoolProp [32], and XSteam [33]. The option selected in this work for modeling the thermodynamic cycles of interest consists in using a commercial software REFPROP [34] along with the programming script language MATLAB® [35]. More specifically, the commercial software is used to evaluate fluid properties and to calculate thermodynamic states, while our in-house script computes energy balances and the specific power output of the thermodynamic cycles. The numerical model developed in this paper has been validated by simulating a binary cycle already analysed in [2]. For instance, the required brine and isopentane mass flow rates obtained from the numerical model differed by less than 0.3% with those presented in [2]. Hence, the numerical model was assumed to be valid.

1.5. Optimization methodology

The objective of this paper is to maximize the geothermal power plants performance. The definitions of the objective function, of the design variables, and of the constraints for both cycles are provided in the following sections. Various algorithms have been used to optimize thermodynamic cycles (e.g. [36]). In the present work, the optimization problems are solved by using the Optimization Toolbox™ of the programming software MATLAB [37]. More specifically, the function *fmincon.m* is used with an “interior-point” algorithm [38]. That algorithm has already been used in the context of thermodynamic cycle optimization in literature (e.g., [39]).

1.5.1. *Subcritical cycle optimization*

The objective function selected in this study is the power plant specific power output w. Specific power output has been used for various analyses of ORC in literature (e.g., [16]; [5]; [17], and it represents the amount of energy (kJ) produced for each kg of geofluid extracted from the ground. The three design variables are the pressure P_2 that prevails in the heat exchangers, the mass flow rate ratio $R_{b,w} = \dot{m}_b / \dot{m}_w$ between the geofluid and the working fluid, and the efficiency ε_{SH} of the superheater (see SH in Fig. 1.1a). Indeed, by considering this efficiency (ε_{SH}) as a design variable, it is possible to obtain a wide range of possible temperature values for state {5} in the superheated state. The optimization statement of the subcritical cycle can be summarized as:

$$\begin{aligned}
&\text{maximize}\left(w\right)\\
&\text{optimizing}\left(P_2, R_{b,w}, \varepsilon_{SH}\right)\\
&\text{respecting}\begin{cases} h_5 \geq h_{g@P_2}, & \varepsilon_{EV} \leq \varepsilon_{\max} \\ x_{\min} \geq x_{tol}, & T_b - T_w \geq \Delta T_{tol} \\ \varepsilon_{EC} \leq \varepsilon_{\max}, & \end{cases}\\
&\text{fixed values}\begin{cases} T_A, T_c, x_{tol}, \Delta T_{tol} \\ \eta_p, \eta_{dry}, \varepsilon_{\max} \end{cases}
\end{aligned} \tag{1.4}$$

Five constraints are defined in Eq. (1.4). First, the working fluid at state {5} must be superheated ($h_5 \geq h_{g@P_2}$). Next, the minimal vapor quality reported in the turbine $x_{\min}$ has to be greater than a tolerance quality $\left(x_{tol} = 0.85\right)$ during the entire expansion process in the turbine, so as to avoid excessive blade wear [7]. The value of $x_{\min}$ is obtained with the methodology explained in Section 1.4.4. Furthermore, efficiencies of the evaporator ε_{EV} and of the economizer ε_{EC} are not fixed but determined by post-treatment and they are not allowed to exceed an imposed maximum value $\left(\varepsilon_{\max} = 0.85\right)$. Finally, the difference between the geofluid temperature T_b and the working fluid temperature T_w at any stage (see Fig. 1.4) must be greater than a minimum value $\left(\Delta T_{tol} = 5°\text{C}\right)$. That last constraint can be verified by using the methodology explained in Section 1.4.5. The value of the pump efficiency is assumed to be $\eta_p = 0.80$, and that of the turbine dry efficiency is assumed to be $\eta_{dry} = 0.85$.

1.5.2. *Transcritical cycle optimization*

A transcritical cycle can be used when the brine temperature is sufficiently high and when enough heat is provided to the working fluid, so as to obtain a vapor state at the turbine inlet at a pressure greater than the working fluid critical pressure. The objective function is the specific power output w, and the number of design variable decreases from three to two, because the heat exchange now occurs in only one heat exchanger with a single fixed efficiency ε_{HE}. The optimization problem of a transcritical cycle may be stated as:

$$\begin{aligned}
&\text{maximize}\left(w\right)\\
&\text{optimizing}\left(P_2, R_{b,w}\right)\\
&\text{respecting}\begin{cases} T_3 \geq T_{cr} \\ x_{\min} \geq x_{tol} \\ T_b - T_w \geq \Delta T_{tol} \end{cases}\\
&\text{fixed values}\begin{cases} T_A, T_c, x_{tol}, \Delta T_{tol} \\ \eta_p, \eta_{dry}, \varepsilon_{HE} \end{cases}
\end{aligned} \tag{1.5}$$

This optimization is simpler than the previous one because the constraints concerning heat exchanger efficiencies are not needed. Indeed, in this paper, the efficiency of the heat exchanger (HE) shown in Fig. 1.1c is set to a fixed value $\varepsilon_{HE} = 0.85$, which is a typical value for preliminary analyses of ORC heat exchangers [40].

The optimization problem stated in Eq. (1.5) involves three constraints. First, the working fluid at state {3} must be superheated; second, the minimal vapor quality reported in the turbine $x_{\min}$ has to be greater than x_{tol} in the entire expansion in this turbine; and third, the temperature difference between the two fluids in the heat exchanger has to be larger than a minimum value ΔT_{tol}. The values of ΔT_{tol}, x_{tol}, η_p and η_{dry} are the same as those provided in Section 1.5.1. It is worth mentioning that no minimum limit is imposed on the reinjection temperature for both optimization problems (state {D} or state {B}).

1.5.3. *Starting points*

It was observed by the authors that the optimization results may depend on the initial values of the design variables (i.e., the optimization starting points). Each optimization is systematically performed four times, i.e., with four different starting points. The initial values of the design variables are determined randomly, but it is verified that a starting point respects the constraints stated in Eqs. (1.4) and (1.5). Launching four optimization runs with their own starting point increases the odds of obtaining a result that: (i) is close to the global optimal design, and (ii), that respects the constraints stated in Eqs. (1.4) or (1.5). The highest value of the four maximized specific output w was considered as the best performance.

To summarize, for a given set of fluid, condenser temperature T_c and geofluid temperature T_A, the optimization of the subcritical design (Eq. (1.4)) is performed with four different initial points, and the optimization of the transcritical design (Eq. (1.5)) is also performed with four different initial points. Finally, the best system (either subcritical or transcritical system) is identified by comparing the maximal specific output obtained from the optimization of both systems. The algorithm describing the optimization is illustrated in Fig. 1.5.

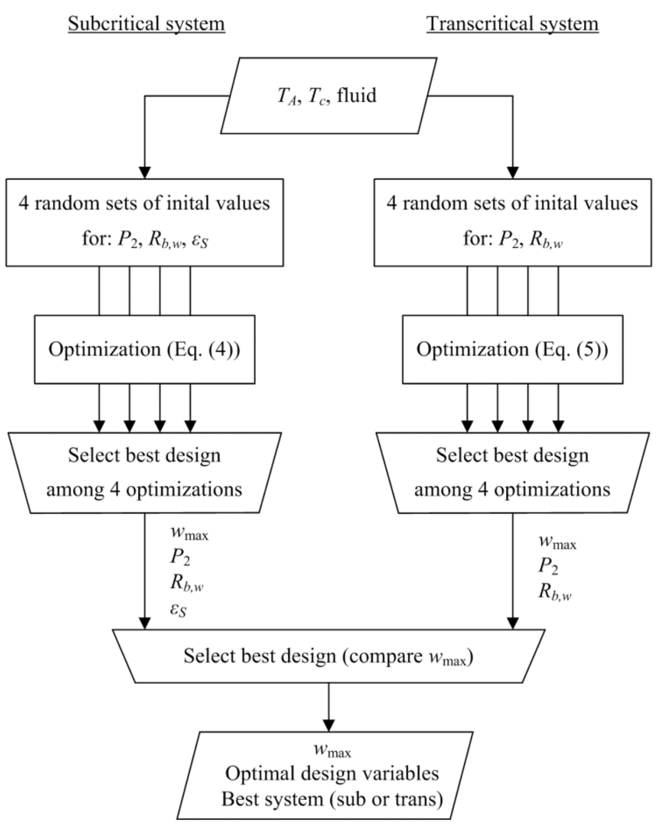

Figure 1.5. Algorithm for optimizing ORC designs.

1.6. One-fluid optimization results

The optimization methodology presented in Fig. 1.5 is performed with one fluid at a time. More specifically, Section 1.6.1 presents optimization with isobutane as working fluid, and shows the behavior of the maximized objective function and of the corresponding optimized design variables with respect to the geofluid temperature. Section 1.6.2 presents the thermodynamic state of the working fluid at the turbine inlet, with respect to the geofluid temperature. For the sake of illustration, optimization results reported in this section were performed by using a condenser temperature fixed to 5°C.

1.6.1. *Optimization with isobutane*

Optimization runs were performed by using isobutane as the working fluid, for brine temperature between 80 and 180°C. The results are reported in Fig. 1.6. More specifically the maximized specific power is shown in Fig. 1.6a, the optimal pressure $P_{2(\mathrm{opt})}$ is shown in Fig. 1.6b, and the optimal mass flow ratio $R_{b,w(\mathrm{opt})}$ in Fig. 1.6c, with respect to T_A. In other words, each point in this figure is the results of a full optimization.

First of all, it can be seen in Fig. 1.6a that the maximized specific power increases with T_A, which is expected because there is more available energy in the geofluid as its temperature increases. The simulation results showed that the best system for geofluid temperature in the range $T_A \in [80,176]^\circ\mathrm{C}$ was the subcritical cycle (see the 'subcritical' label in Fig. 1.6a). Nonetheless, it can be seen that the shape of the curve in Fig. 1.6a is different between the interval $T_A \in [156,176]^\circ\mathrm{C}$. For the higher temperature range, i.e., $T_A \in [176,180]^\circ\mathrm{C}$, the best system was the transcritical system (see the 'transcritical' label in Fig. 1.6a). Indeed, it is expected that transcritical systems only work for the higher range of geofluid temperatures, because such cycles require a higher level of energy from the geofluid.

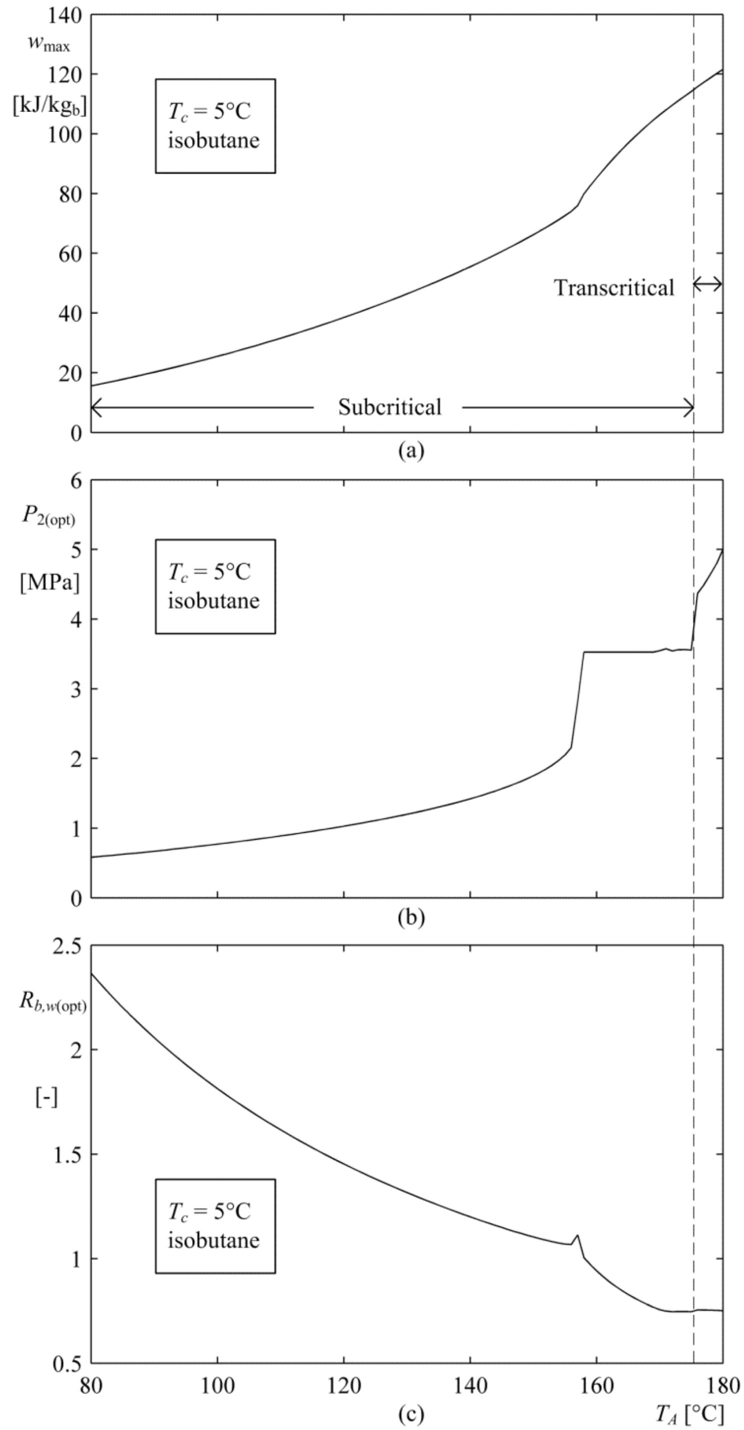

Figure 1.6. Optimization results for a condenser temperature of 5°C with isobutane with respect to brine inlet temperature. (a) Maximal specific power. (b) Optimized heat exchangers pressure. (c) Optimized mass flow ratio.

In Fig. 1.6b, it can be seen that the optimized pressure has a continuous trend until $T_A = 156°\text{C}$, where is undergoes a sharp increase. Indeed, the thermodynamic toolbox used in this work is very sensitive to pressure values that approach the critical pressure P_{cr} . It was observed that for temperature approaching 156 °C, the optimal pressure is very close to the critical pressure (see Fig. 1.6b), and the optimal pressure value of the subcritical design is thus limited by the critical pressure (the plateau observed in Fig. 1.6b). Reaching higher pressure was not possible for $T_A \in [156,176]°\text{C}$ because it would involve a transcritical system, and transcritical system as defined in Eq. (1.5) did not provide better results than the subcritical system for that temperature range $T_A \in [156,176]°\text{C}$. Finally, a sudden increase in pressure occurs at 176°C, because the transcritical system is selected and it requires supercritical pressures.

The optimized mass flow rate ratio $R_{b,w(\text{opt})}$ is shown in Fig. 1.6c. It can be seen that $R_{b,w(\text{opt})}$ decreases steadily until $T_A = 156°\text{C}$, where its trend changes due to the abrupt change of pressure shown previously in Fig. 1.6b. It is also observed that the optimized mass flow ratio becomes almost constant for temperature higher than 176°C, i.e., when the transcritical cycle provides the highest value of specific power.

1.6.2. *Optimization with Propylene and RC318*

A similar optimization was then performed with two other fluids, i.e., with propylene (a normal fluid), and then with RC318 (a retrograde fluid). However, the attention is now focused on the thermodynamic states of the working fluid at the entrance of the turbine (i.e., at state {5} for the subcritical system, and at state {3} for the transcritical system). An important question is whether the working fluid at the turbine inlet is saturated vapor or superheated vapor. In the former case, a superheater (SH in Fig. 1.1a) is not required, while in the latter case, the superheater is required in the system.

Figure 1.7a shows the turbine inlet states of the optimized design when propylene is used. That state is illustrated for various values of the brine inlet temperature T_A. Each square corresponds to the thermodynamic state after a full optimization. Indeed, it can be seen in that figure that the propylene is superheated when subcritical pressures are used, which means that a superheater is required to reach maximal power output. Furthermore, it can be seen in that figure that the temperature at the turbine inlet increases drastically when the best system uses supercritical pressures.

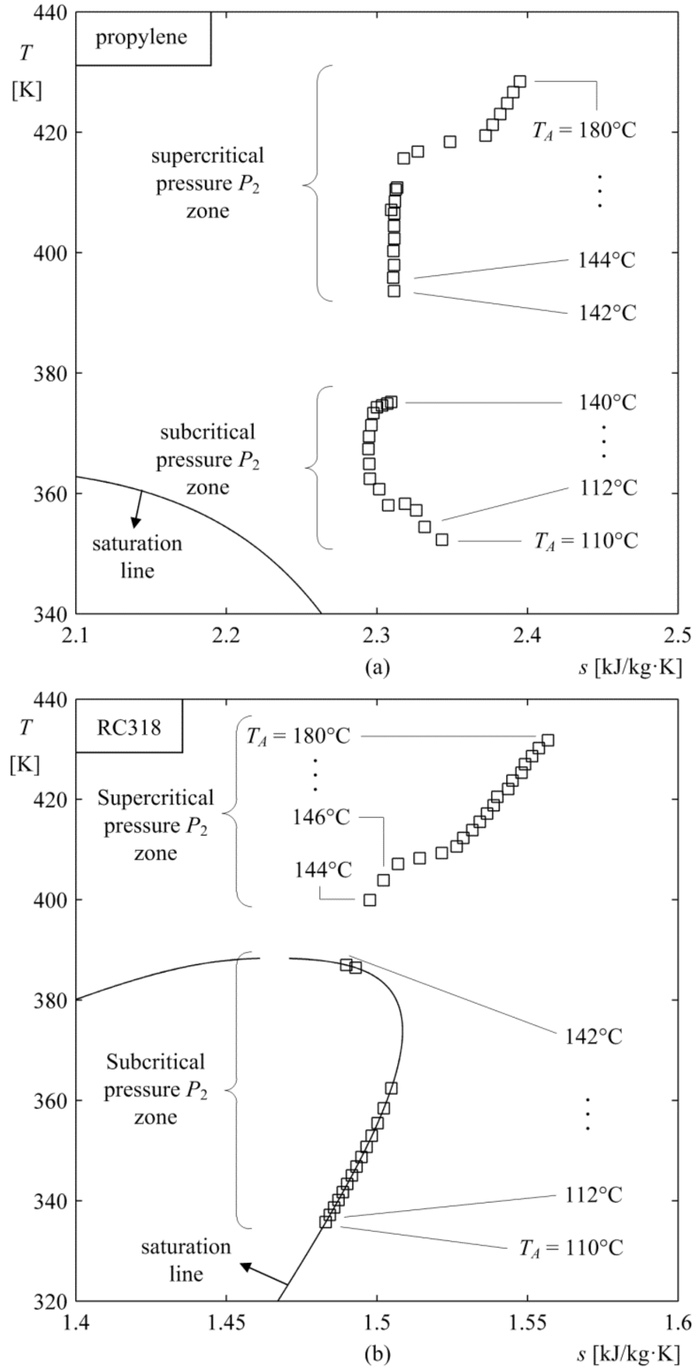

Figure 1.7. Thermodynamic states at turbine inlet in T – s diagram. (a) Propylene. (b) RC318.

The behaviour of the fluid at the turbine inlet differs widely between the various possible working fluids. For example, the optimization was also performed by using RC318 as the working fluid, and the results are reported in Fig. 1.7b. Indeed, it can be seen in that figure that the fluid at the turbine inlet is always saturated vapor for geofluid temperature up to 142°C, i.e., when the best system involves subcritical pressures. In other words, these designs do not require the superheater equipment to reach maximal specific power output. Finally, it can be seen in Fig. 1.7b that the temperature at the turbine inlet gradually increases with the geofluid temperature (T_A), which was also the case in Fig. 1.7a for the propylene. It is expected that the highest temperature in the thermodynamic cycle increases with the temperature of the geofluid, because more energy is available for heat transfer in the heat exchanger.

1.7. Multiple-fluid optimization results

The optimization methodology described in Fig. 1.5 was repeated for a total of 36 fluids (see Table 1.1), for geofluid temperature T_A between 80 and 180°C. The condenser temperature was assumed to be 30°C. For each value of geofluid temperature T_A, the best working fluid was identified (i.e., the fluid with the highest specific power output), and the corresponding objective function and design variables were reported in Fig. 1.8. More specifically, the maximum specific power $w_{\max}$ among all 36 working fluids is presented in Fig. 1.8a, the optimized pressure $P_{2(\mathrm{opt})}$ is presented in Fig. 1.8b, and the optimized mass flow ratio $R_{b,w(\mathrm{opt})}$ is presented in Fig. 1.8c. Each point in this figure represents the comparison of the optimization results for 36 fluids. The best fluid for each temperature range is identified above the figure.

Table 1.1. List of considered working fluids

Fluid	T_{crit} [K]	P_{crit} [kPa]	Fluid	T_{crit} [K]	P_{crit} [kPa]
Ammonia	405.40	11333.00	R1234yf	367.85	3382.20
Butane	425.13	3796.00	R1234ze	382.51	3634.90
Butene	419.29	4005.10	R124	395.43	3624.30
CF3I	396.44	3953.00	R125	339.17	3617.70
COS	378.77	6370.00	R134a	374.21	4059.28
Isobutane	407.81	3629.00	R141b	477.50	4212.00
Isobutene	418.09	4009.80	R152a	386.41	4516.75
Isohexane	497.70	3040.00	R218	345.02	2640.00
Isopentane	460.35	3378.00	R22	369.30	4990.00
Pentane	469.70	3370.00	R227ea	374.90	2925.00
Propane	369.89	4251.20	R236fa	398.07	3200.00
Propylene	364.21	4555.00	R245fa	427.16	3651.00
R11	471.11	4407.64	R32	351.26	5782.00
R113	487.21	3392.20	R365mfc	460.00	3266.00
R115	353.10	3129.00	RC318	388.38	2777.50
R12	385.12	4136.10	RE245cb2	406.81	2886.40
R123	456.83	3661.80	RE245fa2	444.88	3433.00
R1233zd	438.75	3572.60	RE347mcc	437.70	2476.20

It can be seen in Fig. 1.8a that each value of geofluid temperature (abscissa axis) is associated to a working fluid that provides maximal power output. For instance, for geofluid temperature T_A between 80 to 180°C, 10 different fluids are reported as optimal fluids. Moreover, for each fluid, a distinctive behaviour of the optimal design parameters can be observed in Fig. 1.8b and 1.8c. It was verified by the authors that most of the 10 fluids are actually retrograde, except the R125 and R134a. This is an anticipated result because a retrograde behavior allows to avoid the liquid/vapor mixture state and thus improves the turbine efficiency. For most of the temperature range (T_A) shown in Fig. 1.8, the optimal systems selected was the transcritical design (Fig. 1.1c). This design does not involve the superheater efficiency (ε_{SH}) as design variable (see Eq. (1.5)), and as a consequence, that parameter is not shown in Fig. 1.8. Only fluids R218 and R227ea involved the subcritical system, and the corresponding value of ε_{SH} was always below 0.33.

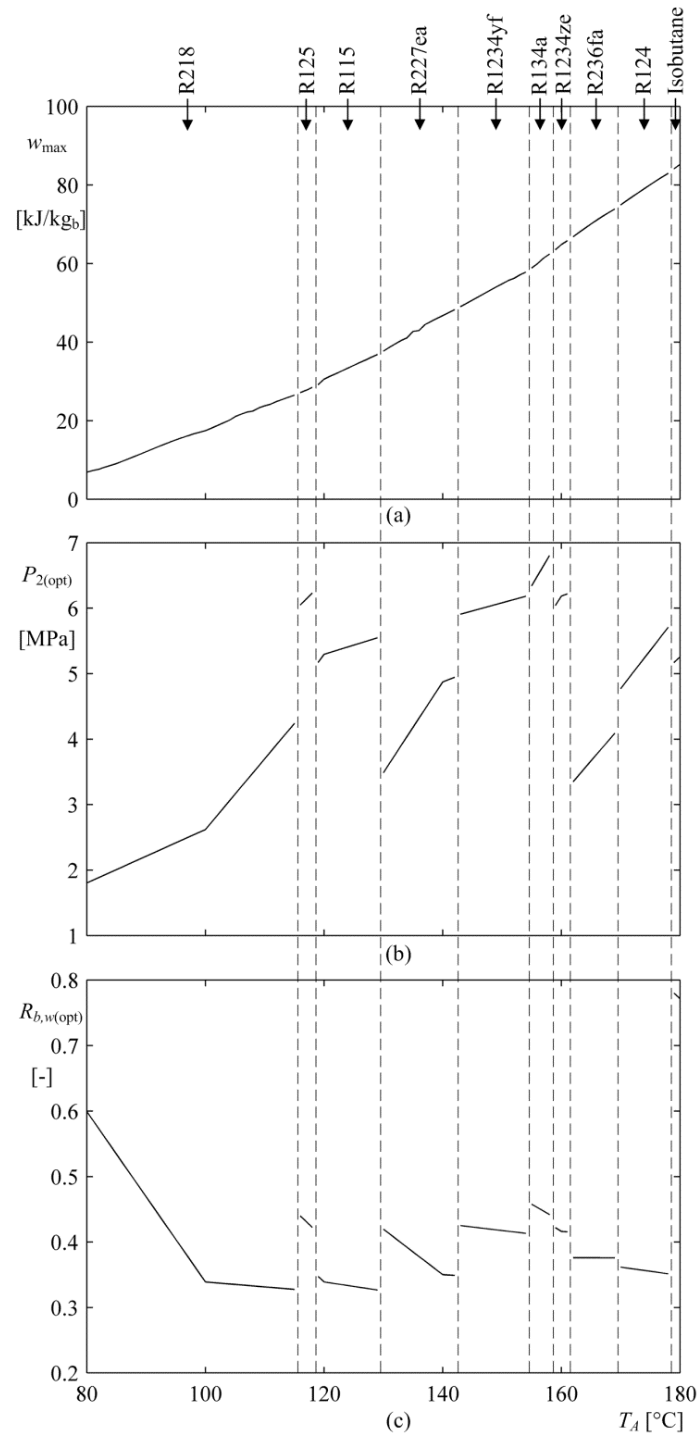

Figure 1.8. Optimization results with best fluids identified on top of the figure with respect to brine inlet temperature. (a) Maximal specific power. (b) Optimized heat exchangers pressure. (c) Optimized mass flow ratio.

1.8. Impact of condenser temperature

The temperature of the condenser (working fluid condensing temperature) in geothermal power plants may have different values depending on its location in the world. Indeed, the climate around a geothermal power plant dictates the outdoor temperature, which then dictates the temperature that is reachable in the condenser. For instance, outdoor temperature in California may be as high as 42°C (AccuWeather, 2015b), while the temperature in the province of Quebec (Canada) may be as low as –32°C (AccuWeather, 2015a). Hence, the optimization performed in Section 1.7 (with 36 fluids) was repeated for a wide range of condenser temperatures, and the results are reported in Figs. 1.9 to 1.12. This analysis allowed to develop design charts that are useful for a wide range of outdoor temperature and of geothermal fluid temperature.

The maximized specific power output $w_{\max}$ was reported with respect to the geofluid temperature T_A (abscissa) and to condenser temperature T_c (ordinate) in Fig. 1.9. Each point in that figure was obtained by optimizing the subcritical and transcritical designs for 36 different fluids, and then by selecting the fluid that provided the highest specific output value. It can be seen in this figure that for any fixed value of condenser temperature (ordinate axis), the maximized specific output $w_{\max}$ increases with the geofluid temperature. Moreover, for any fixed value of geofluid temperature (abscissa axis), the specific output increases when the condenser temperature decreases. These two behaviours are in line with the trends predicted by the ideal Carnot cycle [6]; [7], i.e., the performance can be increased by increasing the temperature of the hot reservoir and by reducing the temperature of the cold reservoir.

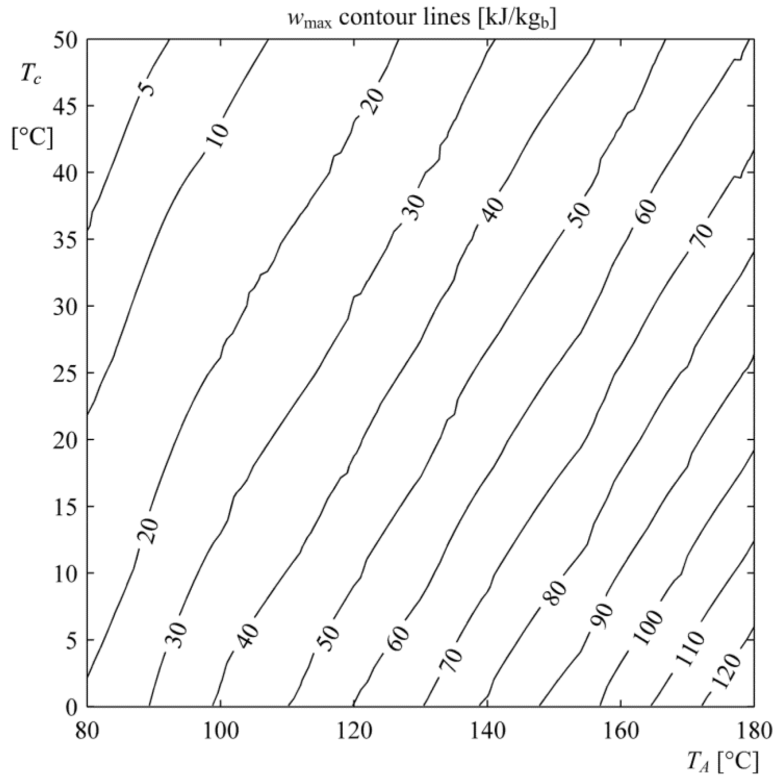

Figure 1.9. Maximal specific power contour lines with respect to brine temperature (x – axis) and to condenser temperature (y – axis).

The best fluids associated to each set of condenser temperature (ordinate) and of geofluid temperature (abscissa) are shown in Fig. 1.10. The best fluids are identified at the top and at the bottom of the figure. It can be seen that a total of 12 fluids (among the 36 listed in Table 1.1) are required to obtain the maximized specific power output for the various geofluid and condenser temperatures investigated in Fig. 1.10. This is a larger number of working fluid than that obtained in Section 1.7 (i.e., 10 fluids in Fig. 1.8). Indeed, the results presented previously in Fig. 1.8 were obtained for a condenser temperature of 30°C, which corresponds to the dashed line in Fig. 10. It can be seen that the 2 additional fluids present in Fig. 1.10 (i.e., RC318 and RE245cb2) are only involved for condenser temperatures higher than 30°C, which explains why they were not present in Fig. 1.8.

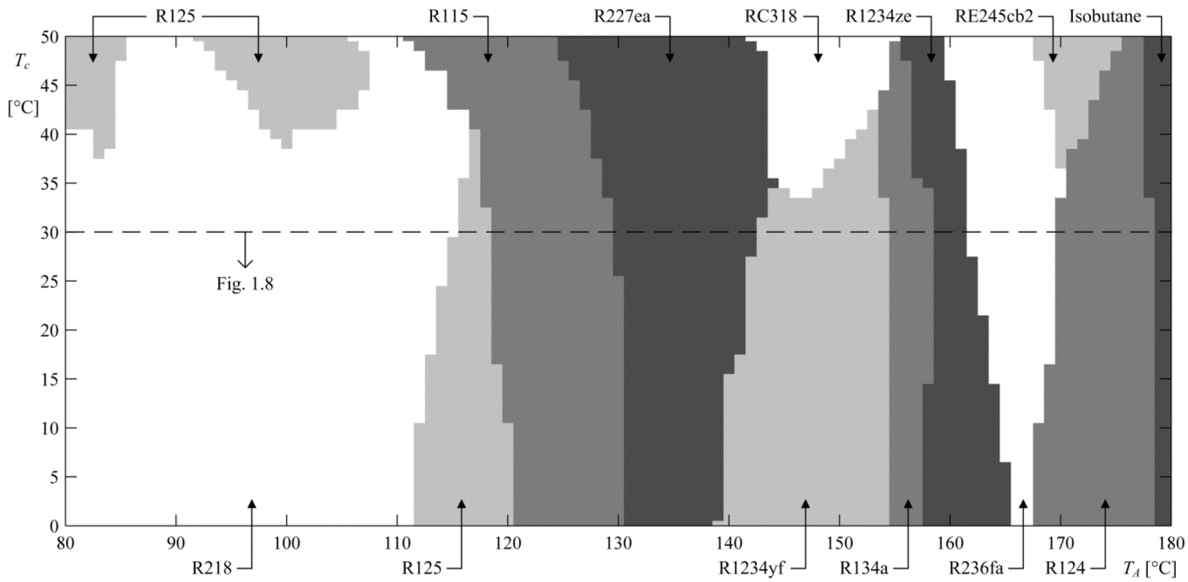

Figure 1.10. Diagram of optimal fluids with respect to brine temperature (x – axis) and to condenser temperature (y – axis).

Figures 1.11 and 1.12 present the contour lines of the corresponding values of the optimized heat exchangers pressure $P_{2(\text{opt})}$ and of the optimized mass flow ratio $R_{b,w(\text{opt})}$, respectively. In both figures, bold dotted lines define the boundaries between the different working fluids displayed in Fig. 1.10. It is therefore expected that the operating conditions strongly vary from one side to the other of these lines because they correspond to a change of working fluid. For most of the temperature ranges for T_A and T_c shown in Figs. 1.10 – 1.12, the optimal systems selected was the transcritical cycle (Fig. 1.1c). Since this design does not involve the superheater efficiency (ε_{SH}) as design variable (see Eq. (1.5)), that parameter is not shown in this section. Only fluids R218 and R227ea involved the subcritical system, and the corresponding value of ε_{SH} was always below 0.4.

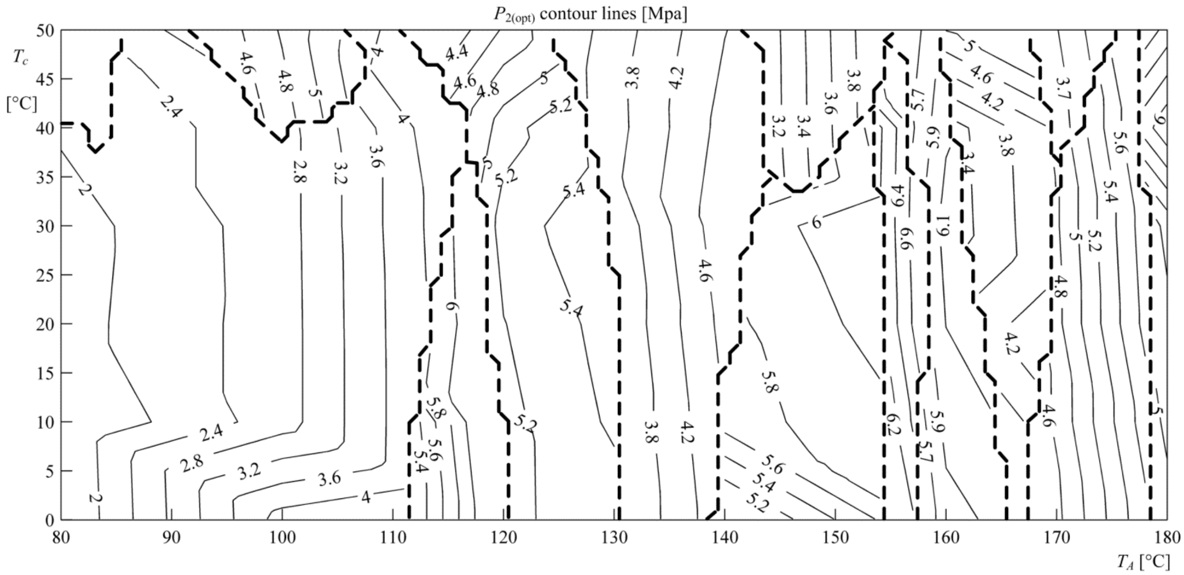

Figure 1.11. Optimized heat exchangers pressure contour lines with respect to brine temperature (x – axis) and to condenser temperature (y – axis).

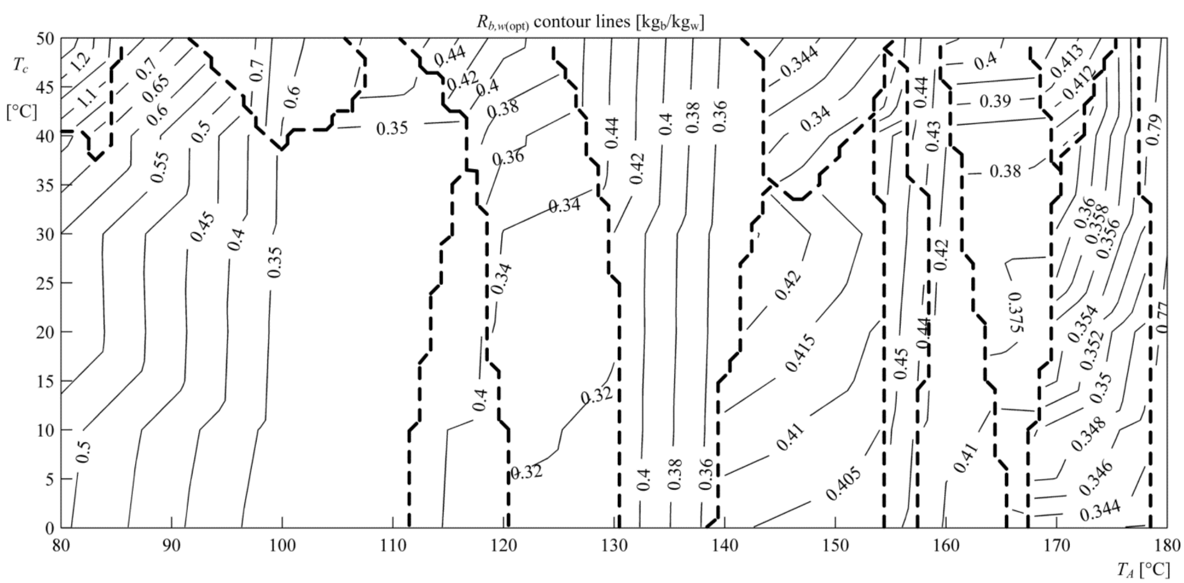

Figure 1.12. Optimized mass flow ratio contour lines with respect to brine temperature (x – axis) and to condenser temperature (y – axis).

Figures 1.10 to 1.12 represent efficient tools for the design of geothermal power plant in various climate conditions and for various geothermal fluid temperatures. They can provide the maximal power output that is achievable for specific conditions, the best choice of working fluid, and a good estimate of the design variable values that would be involved.

1.9. Near-optimal design

In practice, there may be several reasons for not being able to use the optimal fluid presented in Figure 1.10. Indeed, the fluid selection may not be only based on the criterion of geothermal power plant performance. For example, there can be environmental laws that forbid or discourage the use of some fluids. Other fluids may be dangerous for health in case of leaks or may be flammable. Some fluids may be scarce and their price may not be affordable. For these reasons, it is interesting to have a wider working fluid choice without sacrificing too much performance. Fig. 1.13 shows the conditions (i.e., geofluid temperature T_A and condenser temperature T_c) for which a working fluid can provide at least 95% of the maximal specific power reported in Figure 1.9. Among the 36 fluids considered in this paper, 20 respected that criterion for the range of geofluid and condenser temperatures investigated. The conditions at which each fluid allows to obtain 95% of the maximal power output are shaded in each graphics.

It can be seen that some fluids are only relevant for a very restricted range of operating conditions (see Figs. 1.13a, 1.13g, 1.13p). Furthermore, among the 20 fluids that can provide 95% of the maximal power output, only two are efficient for low geofluid temperatures (T_A close to 80°C), i.e., R125 (Fig. 1.13j) and R218 (Fig. 1.13m). On the other hand, 11 fluids are efficient at higher geofluid temperatures (T_A close to 180°C), i.e., Figs. 1.13b, 1.13c, 1.13d, 1.13e, 1.13f, 1.13i, 1.13k, 1.13l, 1.13o, 1.13r, and 1.13t. Hence, further work could involve optimization with a wider set of fluids, so as to obtain more choice for the selection of a working fluid at low geofluid temperatures. Finally, it can be seen that some of the most commonly analysed working fluids in literature (i.e., ammonia, pentane and R245fa) are not present in Fig. 1.13. Hence, the results provided in this section allow to identify fluids that have the potential to outperform the fluid commonly studied and used in practice.

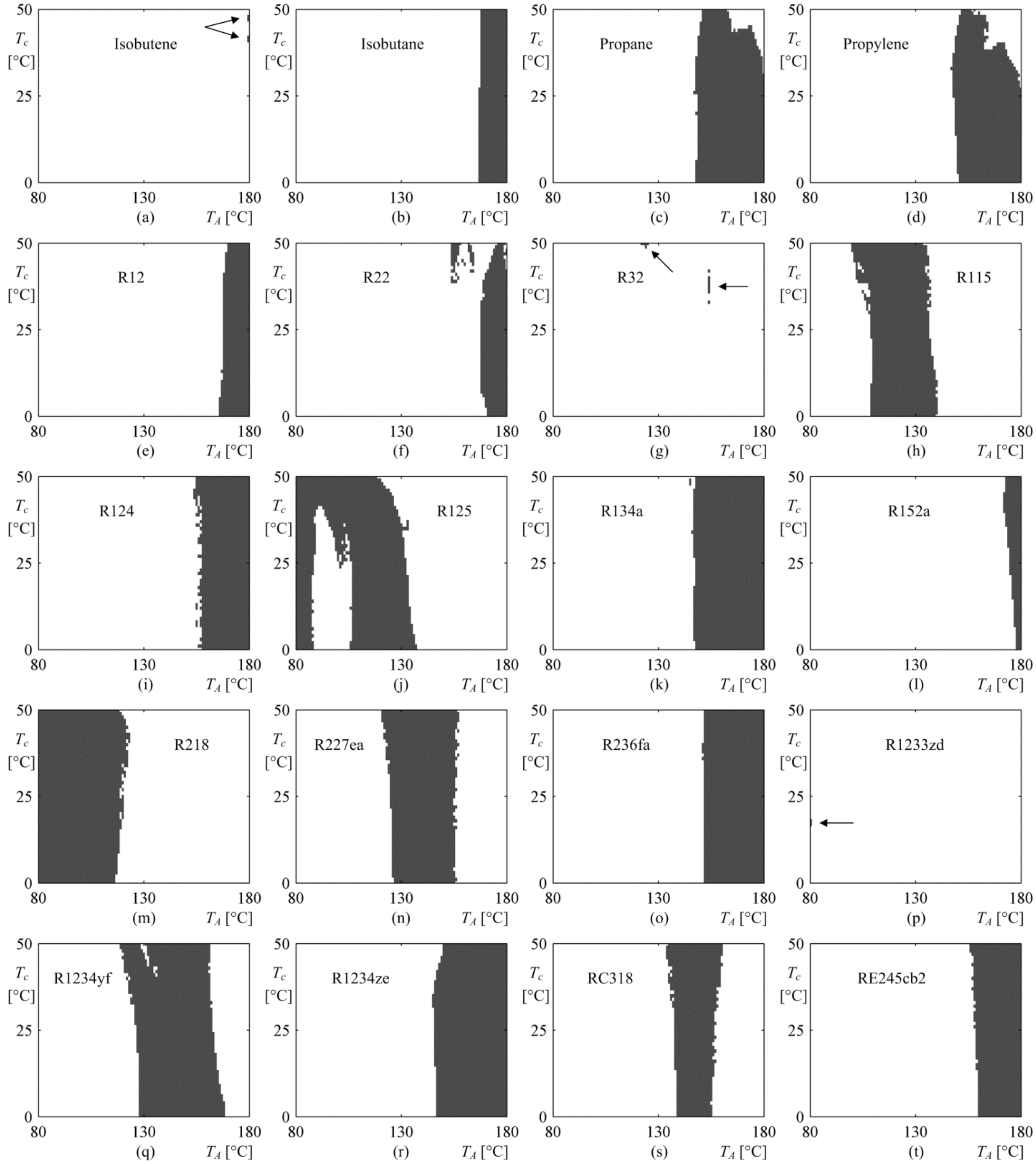

Figure 1.13. Identification of working fluids that can provide more than 95% of the specific power produced by the optimal fluid.

1.10. Theoretical analysis

In many cases, *approximate analyses* may help to explain tendencies observed in optimization results. This has been done for example by DiPippo [2] for identifying optimal separator temperatures that maximize the specific power output of a single-flash steam plant. In this section, it is proposed to use that kind of approximate analysis to develop a function that estimates the maximal possible specific power produced by an ORC, as a function of the operating conditions. Section 1.10.1 shows the theoretical method of the approximate analysis; interpretation of the results is provided in Section 1.10.2; and new correlations are proposed in Section 1.10.3.

1.10.1. *Approximate development*

The development begins with the formula that expresses the specific output power produced in the turbine of a subcritical cycle (see Fig. 1.1b):

$$w = \frac{\dot{W}}{\dot{m}_b} = \frac{\dot{m}_w\left(h_5 - h_6\right)}{\dot{m}_b} = \frac{1}{R_{b,w}}\left(h_5 - h_6\right) \tag{1.6}$$

In order to obtain an expression that depends on temperature, a few approximations have to be made. First, it is supposed that the working fluid enters the turbine at a state that is close to the saturated vapor state, so state {5} is assumed to be approximately equal to state {4}. Furthermore, state {6} is assumed to be relatively close to the saturated vapor state. That kind of assumption may appear to be very imprecise for various types of fluid, but it offers sufficient precision to perform reliable theoretical analyses of thermodynamic cycles (e.g., [2]. Moreover, enthalpy of state {2} is assumed to be approximately equal to that of state {1}. The working fluid enthalpy at the input and output of the turbine can now be expressed in terms of the evaporation enthalpy h_{fg} and in terms of h_3 and h_1, respectively.

$$h_5 \approx h_4 = h_3 + h_{fg} \tag{1.7}$$

$$h_6 \approx h_{g@P_c} = h_1 + h_{fg} \tag{1.8}$$

It is assumed that h_{fg} does not vary much with the pressure. Next, relying on the fact that $h_3 = h_1 + \left(h_3 - h_1\right)$, and assuming that the change of enthalpy between states {1} and {3} may be expressed as $c_w(T_3 - T_1)$, Eq. (1.7) becomes:

$$h_5 = h_1 + c_w(T_3 - T_c) + h_{fg} \tag{1.9}$$

where T_1 is equal to the condenser temperature T_c. Hence, by using Eqs. (1.7) and (1.8), the enthalpy drop present in Eq. (1.6) can be expressed in terms of temperature and specific heat of the working fluid:

$$\begin{aligned} h_5 - h_6 &\approx h_1 + c_w(T_3 - T_c) + h_{fg} - h_1 - h_{fg} \\ h_5 - h_6 &\approx c_w(T_3 - T_c) \end{aligned} \tag{1.10}$$

Hence, Eq. (1.6) becomes

$$w \approx \frac{c_w}{R_{b,w}}\left(T_3 - T_c\right) \tag{1.11}$$

Subsequently, for the purpose of expressing T_3 in terms of T_A, an energy balance in the evaporator (EV in Fig. 1.1a) is invoked. Indeed, the evaporation enthalpy between states {3} and {5} (approximately equal to h_{fg} by virtue of Eq. (1.7)) matches with the enthalpy drop of the geofluid from state {A} to state {C}, i.e.,

$$\begin{aligned} h_{fg} &= R_{b,w}\left(h_A - h_C\right) \\ h_{fg} &= R_{b,w}c_b\left(T_A - T_C\right) \end{aligned} \tag{1.12}$$

The value of T_C may be expressed in terms of T_3 by involving the pinch-point temperature difference, i.e.,

$$T_C \approx T_3 + \Delta T_{pp} \tag{1.13}$$

Combining Eq. (1.12) and Eq. (1.13), it is now possible to express T_3 in terms of the fluids properties and input parameters, i.e.,

$$\begin{aligned} h_{fg} &\approx R_{b,w}c_b\left(T_A - T_3 - \Delta T_{pp}\right) \\ T_3 &\approx T_A - \Delta T_{pp} - \frac{h_{fg}}{c_b R_{b,w}} \end{aligned} \tag{1.14}$$

The expression of T_3 in Eq. (1.14) can be included in Eq. (1.11), and the specific power output can be expressed by the following function:

$$w \approx \frac{c_w}{R_{b,w}}\left(T_A - \Delta T_{pp} - \frac{h_{fg}}{c_b R_{b,w}} - T_c\right)$$
$$w \approx \frac{c_w}{R_{b,w}}\left(T_A - T_c - \Delta T_{pp}\right) - \frac{c_w}{c_b}\frac{h_{fg}}{R_{b,w}{}^2} \tag{1.15}$$

This expression only depends on one design variable, $R_{b,w}$. Hence, to have an optimum, it is necessary to differentiate Eq. (1.15) with respect to $R_{b,w}$:

$$\frac{dw}{dR_{b,w}} = -\frac{c_w}{R_{b,w}{}^2}\left(T_A - T_c - \Delta T_{pp}\right) + \frac{2c_w h_{fg}}{c_b R_{b,w}{}^3} = 0 \tag{1.16}$$

The optimal value of the mass flow ratio is obtained solving for $R_{b,w}$:

$$R_{b,w(\mathrm{opt})} = \frac{2h_{fg}}{c_b\left(T_A - T_c - \Delta T_{pp}\right)} \tag{1.17}$$

The final step is to include that optimal value of $R_{b,w}$ in the specific output power function Eq. (1.15) :

$$w_{\max} = \frac{c_w c_b}{4h_{fg}}(T_A - T_c - \Delta T_{pp})^2 \text{ [J/kg]} \tag{1.18}$$

Equation (1.18) provides an approximate expression for predicting the maximal specific output $w_{\max}$ in terms of the geofluid and condenser temperatures (T_A and T_c), and in terms of the fluids properties (c_w, c_b, h_{fg}).

1.10.2. *Interpretation*

The approximate function obtained in Section 1.10.1 (Eq. (1.18)) predicts some interesting trends. First, the expression is divided in two parts: (i) a coefficient representing the properties of the brine and of the working fluid, and (ii) a squared temperature difference.

The coefficient shows that the maximal specific output power is proportional to the working fluid c_w at liquid state; the greater it is the more power is produced by the plant. Furthermore, it may be observed that the working fluid evaporation enthalpy h_{fg} has an inversely proportional influence on power output in Eq. (1.18). This indicates that a working fluid having a “thin” bell shape in its $T-s$ diagram may provide better geothermal power plant performance. That statement is corroborated by the results of Fig. 1.10, where the majority of working fluids identified are retrograde, i.e., have thin bell shape (Fig. 1.2b) compared to normal fluid (Fig. 1.2a). Overall, from Eq. (1.18), the relevant fluid properties of the working fluid are its specific heat at liquid state and its evaporation enthalpy. Furthermore, from Eq. (1.18), it can be observed that the most influential property of the geofluid is its specific heat, due to its importance during the heat transfer in the heat exchanger EV in Fig. 1.1a.

The second term of the approximate function (the squared temperature difference) involves the temperatures T_A and T_c. Indeed, Eq. (1.18) shows that increasing the condenser temperature T_c for a fixed value of T_A results in a decreases of $w_{\max}$, and that increasing the geofluid temperature T_A for a fixed value of T_c results in an increase of $w_{\max}$, which is corroborated by the numerical results obtained in Fig. 1.9. Overall, the approximate function Eq. (1.18) is able to capture important tendencies observed in the optimization results.

1.10.3. *Correlation development*

The *form* of the approximate equation presented in Eq. (1.18) is used in order to develop a correlation that can predict the trends shown in Fig. 1.9. The idea then consists in performing a best-fit on the numerical results that were used to generate Fig. 1.9. To make the work easier, a change of variable is performed:

$$\begin{aligned} x &= T_A - T_c \\ a &= \frac{c_b c_w}{4h_{fg}} \\ b &= \Delta T_{pp} \end{aligned} \tag{1.19}$$

Equation (1.18) can now be expressed in a quadratic form:

$$w_{\max} = a(x-b)^2 = ax^2 - 2abx + ab^2 \tag{1.20}$$

Then, a second change of variable is performed, i.e., $A = a$ and $B = ab$, which leads to

$$w_{\max} = Ax^2 - 2Bx + B^2/A \tag{1.21}$$

Equation (1.21) represents the expected form of a correlation that matches with the numerical results shown in Fig. 1.9. Hence, a best fit is done by finding the value of coefficients A and B that leads to the lowest difference with the optimization results shown in Fig. 1.9. It is carried out by using the Optimization Toolbox$^{\text{TM}}$ of MATLAB [37]. The values of the coefficients found and their corresponding physical meaning are presented below:

$$\begin{aligned} A_{bf} &= a = \frac{c_w c_b}{4h_{fg}} = 4.3016 \text{ [J/K}^2 \cdot \text{kg]} \\ B_{bf} &= ab = 26.410 \text{ [J/K} \cdot \text{kg]} \\ b_{bf} &= \Delta T_{tol} = 6.140 \text{ [K]} \end{aligned} \tag{1.22}$$

The relative error between the best-fit function w_{bf} and the numerical results $w_{\max}$ is 4%, with a maximum error of 21% for the lowest value of brine temperature.

It should be observed that a best-fit value of 6.140 K is found for the minimum imposed temperature difference ΔT_{tol}, which is very close to the assumed minimum value of 5.0 K that was imposed in the numerical optimization.

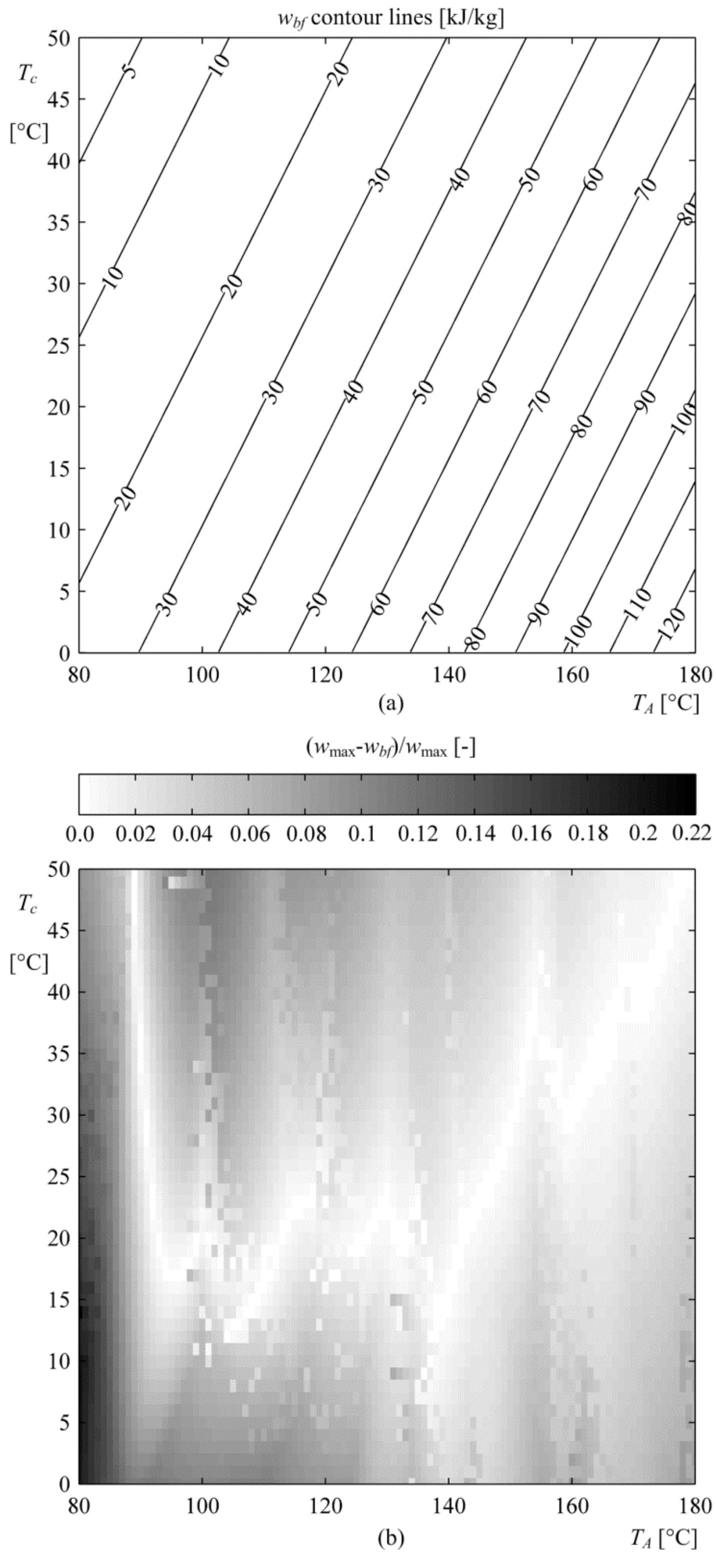

Figure 1.14. Illustration of the best-fit correlation (Eqs. (1.21)-(1.22)) obtained from approximate analysis. (a) Specific power output best-fit contour lines with respect to brine temperature (x – axis) and to condenser temperature (y – axis). (b) Relative error with numerical results.

Figure 1.14a illustrates the best fit function w_{bf} (Eq. (1.21)) obtained with the values of A_{bf} and B_{bf} reported in Eq. (1.22), and Fig. 1.14b illustrates the relative error with the original optimization results (Fig. 1.9), both with respect to the brine inlet temperature T_A on the x – axis and to the condenser temperature T_c on the y – axis. The values shown in Fig. 14a are clearly very similar to those shown in of Fig. 1.9, which shows that the approximate analysis can provide a correct form of correlation for expressing the maximal power output $w_{\max}$. In other words, the approximate analysis performed in Section 1.10.1 correctly captured the relevant phenomena present in the thermodynamic cycle investigated in this paper.

1.11. Discussion

Diagrams presented in Sections 1.8 and 1.9 (i.e., Figs. 1.9 – 1.13) are meant to be used as tools to design the Organic Rankine Cycle of a geothermal power plant. They provide some “rules of thumb” to select the optimal design that maximizes the specific output power of a geothermal power plant. For instance, the optimal working fluid and operating parameters ($P_{2(\mathrm{opt})}$, $R_{b,w(\mathrm{opt})}$) can be determined by knowing the operating conditions (T_A and T_c).

To use the results of this paper is quite simple. The brine inlet temperature and the condenser temperature become coordinates of a point in Figs 1.9 – 1.13 that gives the estimated maximal specific power, the best working fluid, the optimized turbine inlet pressure, the optimized mass flow ratio, and the alternatives working fluids, respectively. For example, if a region has a geothermal reservoir with brine that reaches 165°C at the surface, and a climate that leads to a condenser temperature of 30°C, the maximum specific power is 70 kJ/kg (see Fig. 1.9). The best fluid would be R236fa (see Fig. 1.10), while its optimal operating conditions would be a pressure of 3.67 MPa (see Fig. 1.11) and a mass flow ratio of 0.376 (see Fig. 1.12). At the operating conditions mentioned above ($T_A = 165°\mathrm{C}$ and $T_c = 30°\mathrm{C}$), Fig. 1.13 shows that there are 7 alternatives for R236fa among the 36 fluids analysed: R1234ze (Fig. 1.13r), R124 (Fig. 1.13i), R134a (Fig. 1.13k), R236fa (Fig. 1.13o), RE245cb2 (Fig. 1.13t), propane (Fig. 1.13c) and propylene (Fig. 1.13d).

Naturally, if one of these fluids is chosen instead of the optimal one shown in Fig. 1.10, the optimal operating parameters will differ from those shown in Figs. 1.11 and 1.12.

1.12. Conclusion

In this paper, subcritical and transcritical Organic Rankine Cycles for geothermal power plant are numerically simulated and then optimized with respect to brine inlet temperature and condenser temperature. New elements of modeling were introduced: a method based on differential thermodynamic evolution to calculate the turbine efficiency, and a technique to assert that the minimal pinch point constraint is respected in heat exchangers. Thirty-six (36) working fluids were considered in the optimization. The objective function was the power plant specific output, and the design variables were the turbine inlet pressure, the mass flow ratio between the geofluid and the working fluid, and the superheater efficiency (only for the subcritical cycle). Optimization was performed numerically for a range of brine inlet temperature from 80 to 180°C and a range of condenser temperature from 0.1 to 50°C.

The work described in this paper proposes two new results. First, it introduces a predesign decision-making tool (Figs. 1.9 – 1.13) for thermodynamic cycle design of low-temperature reservoir geothermal plants, which takes the form of charts. These new charts widen the guidelines provided in a previous work by Clarke and McLeskey Jr. [26]. Second, a new correlation allows to predict the maximal specific output (Eqs. (1.21)-(1.22)).

Further studies could extend the analysis performed in this paper. Other cycle configurations can be modeled and optimized, such as an ORC with dual-pressure heating, resuperheating, and steam extraction. Moreover, the cooling system could be added to the model so that optimization could involve the thermodynamics of cooling tower instead of a simple condenser temperature. The performance of the geothermal thermodynamic cycle could be assessed in the context of off-design operating conditions during the whole lifespan of the power plant. Finally, the list of working fluid candidates (Table 1.1) could be extended by taking account more fluids and mixtures of fluids.

CHAPITRE 2. OPTIMAL DESIGN OF GEOTHERMAL POWER PLANTS: A COMPARISON OF SINGLE-PRESSURE AND DUAL-PRESSURE ORGANIC RANKINE CYCLES

2.1. Résumé

Quatre variantes du cycle de Rankine organique (ORC) appliqué à des centrales géothermiques sont optimisées au moyen d'outils numériques. Ces variantes sont : (i) l'ORC sous-critique avec chauffage à pression unique (ORC/S/SC), (ii) l'ORC transcritique avec chauffage à pression unique (ORC/S/TC), (iii) l'ORC sous-critique avec chauffage à deux pressions (ORC/D/SC), et (iv) l'ORC transcritique avec chauffage à deux pressions (ORC/D/TC). Tous les systèmes incluent un système de récupération interne de la chaleur et une tour de refroidissement à voie humide. La fonction objectif est le travail spécifique net et les variables de design comprennent les pressions d'opération, les ratio de débits massiques entre le géofluide et le fluide de travail, l'efficacité des surchauffeurs et l'écart de température dans la tour de refroidissement. Les systèmes sont optimisés pour chacun des 20 fluides de travail potentiels. L'optimisation est effectuée pour des températures d'entrée du géofluide de 80 à 180°C, et pour des températures du thermomètre mouillé de l'air ambient de 10 à 32°C. Les résultats montrent : (i) la supériorité de l'ORC/D/TC pour la plupart des cas, (ii) la pertinence d'utiliser un chauffage à deux pressions lorsque la température du puits de chaleur est haute et la température du géofluide est basse, et (iii) l'importance du choix de l'écart de température de la tour de refroidissement pour un design de centrale optimal.

2.2. Abstract

Four variants of the Organic Rankine Cycle (ORC) applied to geothermal power plants are optimized by means of numerical tools. These variants are: (i) the subcritical ORC with single-pressure heater (ORC/S/SC), (ii) the transcritical ORC with single-pressure heater (ORC/S/TC), (iii) the subcritical ORC with dual-pressure heater (ORC/D/SC), and (iv) the transcritical ORC with dual-pressure heater (ORC/D/TC). All the systems are recuperative and include a wet cooling tower. The objective function is the specific work output and design variables include operating pressures, mass flow ratios between the brine and the working fluid, superheaters effectiveness and cooling tower range. The systems are optimized for 20 different potential working fluids. The optimization is performed for inlet brine temperatures from 80 to 180°C, and for ambient air wet bulb temperatures from 10 to

32°C. The results show: (i) the superiority of ORC/D/TC for most of the cases, (ii) the relevance of using a dual-pressure heater at high sink temperature and low brine temperature, and (iii) the importance of choosing the right cooling tower range for an optimal power plant design.

2.3. Introduction

Finding energy alternatives to fossil fuels is required to reduce greenhouse gases emissions. In recent years, research on geothermal power plants generated a lot of interest worldwide. Increasing their efficiency gives the opportunity to regions of the world with low-temperature geothermal reservoirs to produce power from Earth's heat in a cost-effective way. In this context, the Organic Rankine Cycle (ORC) is the most appropriate system to convert low-grade heat to electricity [43]. The ORC has become a relatively mature technology over the last decade, but there is still a challenge to improve its thermodynamic performance and competitiveness [44].

Various studies were performed on the ORC to determine optimal design guidelines, like Astolfi et al. [17], Clarke and McLeskey Jr. [26], Chagnon-lessard et al. [45], Park et al. [46] and Uusitalo et al. [47], just to name a few. Cycle variants are also investigated in order to improve performance. First, more and more investigations are devoted to transcritical regime [48]–[51], in which a greater enthalpy drop could be achieved in the turbines. Then, energy recovery within the system can be set up to increase the overall thermal efficiency, which can be accomplished by using regeneration [52]–[54] or recuperation [55]–[57], for example. Even if both techniques help preheating the working fluid, they are significantly different: energy recovery is accomplished by mass transfer (vapor extracted from the turbine at an intermediate pressure) when using regeneration, whereas it relies on heat transfer (from the turbine outlet) when using recuperation. Concerning the latter, Oyewunmi et al. [58] concluded that for maximum power production, a recuperator is necessary for ORCs with constraints imposed on their evaporation and condensation pressures. Moreover, Astolfi et al. [17] determined that recuperation is profitable if a constraint on reinjection temperature is assumed. Furthermore, a dual-pressure heater may be employed, in which the working fluid is divided in two distinct flows to evaporate them at two different pressures, which may lead to a better heat utilization. Recent research development on this ORC variant demonstrated potential benefits when considering low and medium-grade heat sources.

For example, a notable study on dual-pressure heater ORC was made by Li et al. [59], where the authors optimized evaporation pressures and turbines inlet temperatures considering a general heat source temperature from 100 to 200°C with a fixed inlet cooling water temperature. Based on the design optimization for nine pure fluids, they found that the net power of dual-pressure heater ORCs can increase by 21.4 to 26.7% compared to an ORC with a single-pressure heater. Manente et al. [60] suggested a guideline stating that a dual-pressure heater yields no power gain when the heat source inlet is more than 40°C above the working fluid critical temperature. When the latter is similar or higher than the heat source inlet temperature, the gain in power output is in the order of 20% and more. Employing isobutane, Wang et al. [61] determined that a dual-pressure heater can significantly increase the ORC net power output, without decreasing its thermo-economic performance, though there is no power gain when heat source temperature is above 177.2°C (which corresponds to 42.54°C above its critical temperature). Dual-pressure heater ORC presents two typical turbine layouts, i.e., the separate turbine layout and the induction turbine layout: Li et al. [62] concluded that the induction turbine layout was the one leading to the greater power output.

Finally, one of the most recent developments in the field of ORC with multi-pressure heaters was done by Li et al. [63] who proposed a novel ORC configuration where the highest evaporating pressure is supercritical while the lowest one stays subcritical. Using R1234ze(E), the maximum net power output of this new cycle is the largest for heat source temperatures above approximately 135 °C. The authors wrote that “it can increase by 19.9%, 49.8%, and 20.4% at most compared with those of the conventional subcritical, transcritical, and dual-pressure evaporation cycles, respectively.”

The paper mentioned above provided important insights on the potential benefits of using a multi-pressure ORC over the single-pressure ORC, and to the authors’ opinion, new questions arise from this body of work: (i) What is the best design of ORC (single or dual-pressure) when considering various possible combinations of geothermal fluid temperature and outdoor conditions? (ii) What is the corresponding optimal working fluid? (iii) What are the corresponding optimal design variable values? Similar questions were raised in a previous work [45], and the results were synthetized in the form of design charts. However, that paper was only investigating single pressure ORC, cooling system was not explicitly considered, there was no constraint on the reinjection temperature, and energy recuperation system was not present.

Hence, in this paper, the ideas presented in Chagnon-Lessard et al. [45] (i.e., performing numerical optimization of ORC cycles and presenting the results in the form of charts) is improved by considering the most recent developments in ORC designs. Upgrades include the addition of the subcritical and transcritical dual-pressure heater ORC (in the ORC/D/SC and ORC/D/TC systems), the implementation of a wet cooling tower as cooling system, a minimum reinjection temperature, and the addition of a recuperator in the cycle.

In other words, the goal of this work is to optimize and compare four variants of ORC: (i) the subcritical ORC with single-pressure heater (ORC/S/SC), (ii) the transcritical ORC with single-pressure heater (ORC/S/TC), (iii) the subcritical ORC with dual-pressure heater (ORC/D/SC), and (iv) the transcritical ORC with dual-pressure heater (ORC/D/TC). All the systems are recuperative and include a wet cooling tower. The objective function is the specific work output and design variables include operating pressures, mass flow ratios between the brine and the working fluid, superheaters effectiveness and cooling tower range. A total of 20 different potential working fluids are considered. The optimization is performed for inlet brine temperatures from 80 to 180°C, and for ambient air wet bulb temperatures from 10 to 32°C.

The paper is organized as follows: Section 2.4 describes the four ORCs of interest and the approach to perform the numerical simulations; Section 2.5 formulates the optimization problems; Section 2.6 presents the results of this work with discussions; and Section 2.7 provides the conclusions.

2.4. Problem statement

The four power cycles are described in Sections 2.4.1 to 2.4.4. The systems considered in this paper are (i) a subcritical Organic Rankine Cycle (ORC) with single-pressure heater (ORC/S/SC), (ii) a transcritical ORC with single-pressure heater (ORC/S/TC), (iii) a subcritical ORC with dual-pressure heater, and (iv) a transcritical ORC with dual-pressure heater (ORC/D/TC). The selected cooling system is presented in Section 2.4.5 and details on the numerical simulations are provided in Section 2.4.6.

2.4.1 *Single-pressure heater subcritical Organic Rankine Cycle (ORC/S/SC)*

A binary geothermal power plant possesses two main circuits, i.e., the primary and secondary circuits (see Fig. 2.1a). The primary circuit is an open cycle where the geothermal brine, or geofluid, is first pumped from the reservoir and enters the plant at state {A}. Then, it flows through either one heat exchanger [27] or a series of three heat exchangers. The latter configuration is considered in this paper for subcritical regime, where the geofluid exit conditions of each exchanger correspond to states {B}, {C} and {D}, respectively. The circuit ends with the geofluid reinjection in the reservoir at state {D}. Although the geothermal fluid typically contains dissolved gas and calcite, it is assumed in this work that its properties may be approximated as equal to those of pure water, which is in line with recent literature, e.g., [28], [29].

In this study, the secondary circuit of the first system (ORC/S/SC) corresponds to the ORC with recuperation, which consists of a closed cycle performed by the working fluid (see states {1} to {6'} in Figs. 2.1a and 2.1b). Fluid at state {1}, a saturated liquid at the condenser pressure, enters the pump (PP) to reach the desired subcritical pressure at turbine inlet P_H (state {2}). Then, it receives heat from the turbine outlet (state {6}) in the recuperator (RE) to achieve state {2'}. Recuperation in power cycles must not be confused with regeneration, e.g. see Chapter 3 of [64] for more explanations on the recuperator. Next, the working fluid is heated at constant pressure by the geofluid circulating in the primary circuit: the fluid becomes a saturated liquid (state {3}) in the economizer (EC), then it is fully evaporated to reach the state of saturated vapor (state {4}) in the evaporator (EV), and finally it turns to superheated vapor (state {5}) at the superheater outlet (SH).

See Fig. 2.1c for the T-Q diagram of this heat exchange. States {4} and {5} overlie (as well as states {A} and {B}) when there is no heat transfer in the superheater, and as a consequence, the fluid enters the turbine as saturated vapor. The fluid then leaves the turbine (TB) at the condensing pressure (state {6}) and passes through the recuperator so as to transfer heat to the fluid leaving the pump outlet when the temperature difference is sufficient. Lastly, the working fluid rejects heat to the water used in the cooling system and returns to state {1} as saturated liquid. See Appendix A for the step-by-step calculation model used to determine the specific work output.

2.4.2 *Single-pressure heater transcritical Organic Rankine Cycle (ORC/S/TC)*

Figures 2.1d and 2.1e show the ORC/S/TC, i.e., the second system studied in this work. Its only difference with the ORC/S/SC is that its pressure P_H in the heater is supercritical, making the cycle transcritical. The fluid at state {2'} leaving the recuperator (RE) is heated at constant pressure by the geofluid in a single heat exchanger (HE) instead of three, and it becomes superheated (state {3}). From state {A}, the geofluid is thus cooled to state {B} before being reinjected in the reservoir (see Fig. 2.1f for the T-Q diagram).

This system can be used solely if the working fluid critical temperature is sufficiently lower than the geofluid inlet temperature (state {A}) and also lower than its maximum temperature of applicability (identified as $T_{\max}$ in Table 2.6, where values are given by the National Institute of Standards and Technology [34]). Above a certain temperature, organic fluids may experience chemical decomposition due to the loss of their thermal stability. Therefore, some working fluids cannot be safely used in a transcritical cycle, like R236fa, with its critical temperature being practically the same as its maximum temperature of applicability. Finally, the calculation method for predicting the specific work output of this system is similar to that shown previously in Appendix A.

2.4.3 *Dual-pressure heater subcritical Organic Rankine Cycle (ORC/D/SC)*

Having a multi-pressure heater in an ORC can improve the use of the geothermal energy by achieving a smaller average temperature difference between the two fluids, thus reducing the thermodynamic losses in the heat exchangers [65]. The ORC/D/SC integrates this concept by including a second set of heat exchangers, pump, and turbine or turbine stage (see Figs. 2.1g and 2.1h). The working fluid route begins at state {1} where it enters in the first pump (PP/MP) to reach the medium subcritical pressure P_M at state {2} and passes through the recuperator (RE) to reach the conditional state {2'}. It receives the geofluid heat in the medium-pressure economizer (EC/MP) to attain the state of saturated liquid (state {3}). At the outlet, the fluid is split into two streams. One of them pursues its way in the medium-pressure evaporator (EV/MP) leaving it at saturated vapor (state {4}) and then the medium-pressure superheater (SH/MP) brings it to state {5}. The other stream is compressed to state {6} at the subcritical heating pressure P_H by means of the second pump (PP/HP). Then, it is heated by the higher-grade geothermal energy in the second heat exchangers set. The high-pressure economizer (EC/HP) brings this working fluid fraction to saturated liquid (state {7}), the high-pressure evaporator (EV/HP) to saturated vapor (state {8}), and the high-pressure superheater (SH/HP) to the high-pressure turbine (TB/HP) inlet at state {9}, see Fig. 2.1i for the T-Q diagram. From state {A}, the geofluid passes through six heat exchangers, which are assumed to be in series, and is reinjected at state {G}. The high-pressure working fluid fraction leaves the turbine at the medium pressure P_M (state {10}) to be mixed with the other fraction at state {5}, creating state {11}. The total working fluid flow is then admitted in the medium-pressure turbine (TB/MP), exiting at the condensing pressure (state {12}). This turbine arrangement corresponds to an induction turbine layout [62]. Finally, it reaches the conditional state {12'} in the recuperator and returns to state {1} as saturated liquid in the condenser (CO), cooled at constant pressure by the water from the cooling system.

Figure 2.1i illustrates how the geofluid heat can be used more efficiently in the ORC/D/SC than in the ORC/S/SC. Evaporating the working fluid at two different temperatures allows each fraction to absorb a portion of the heat with a smaller average temperature difference. In other words, the geofluid line in a T-Q diagram (the dashed line) is closer to the working fluid line (the solid line). The global area between the brine and working fluid in a T-Q diagram is therefore reduced and less exergy is lost in the heat exchange process.

Finally, the calculation method for predicting the specific work output of this system follow the same ideas as those shown previously in Appendix A, but it is not included here for conciseness of the paper.

2.4.4 *Dual-pressure heater transcritical Organic Rankine Cycle (ORC/D/TC)*

The ORC/D/TC shares most of its states with the ORC/D/SC, see Figs. 2.1j and 2.1k. Their difference resides in the replacement of the high-pressure series of heat exchangers (EC/HP, EV/HP, SH/HP in Fig. 2.1g) by one supercritical heat exchanger (HE). The working fluid portion at state {6} receives the higher-grade heat from the geofluid at the desired supercritical pressure P_H and is admitted in the high-pressure turbine (TB/HP) at state {7}. Figure 1l shows the geofluid going from state {A} to state {B} while circulating in the supercritical heat exchanger, and to states {C}, {D} and {E} after passing through each medium-pressure heat exchanger, before being reinjected in the ground. Note that the fluid is not supercritical at the inlet of the second turbine stage (state {9}), since the medium pressure was assumed to be subcritical.

As for the ORC/S/TC, the conditions of utilization are a geofluid inlet temperature (state {A}) and a working fluid's maximum temperature of applicability sufficiently higher than the working fluid's critical temperature.

Again, the calculation method for predicting the specific work output of this system follow the same ideas as those shown previously in Appendix A, but it is not included here for conciseness of the paper.

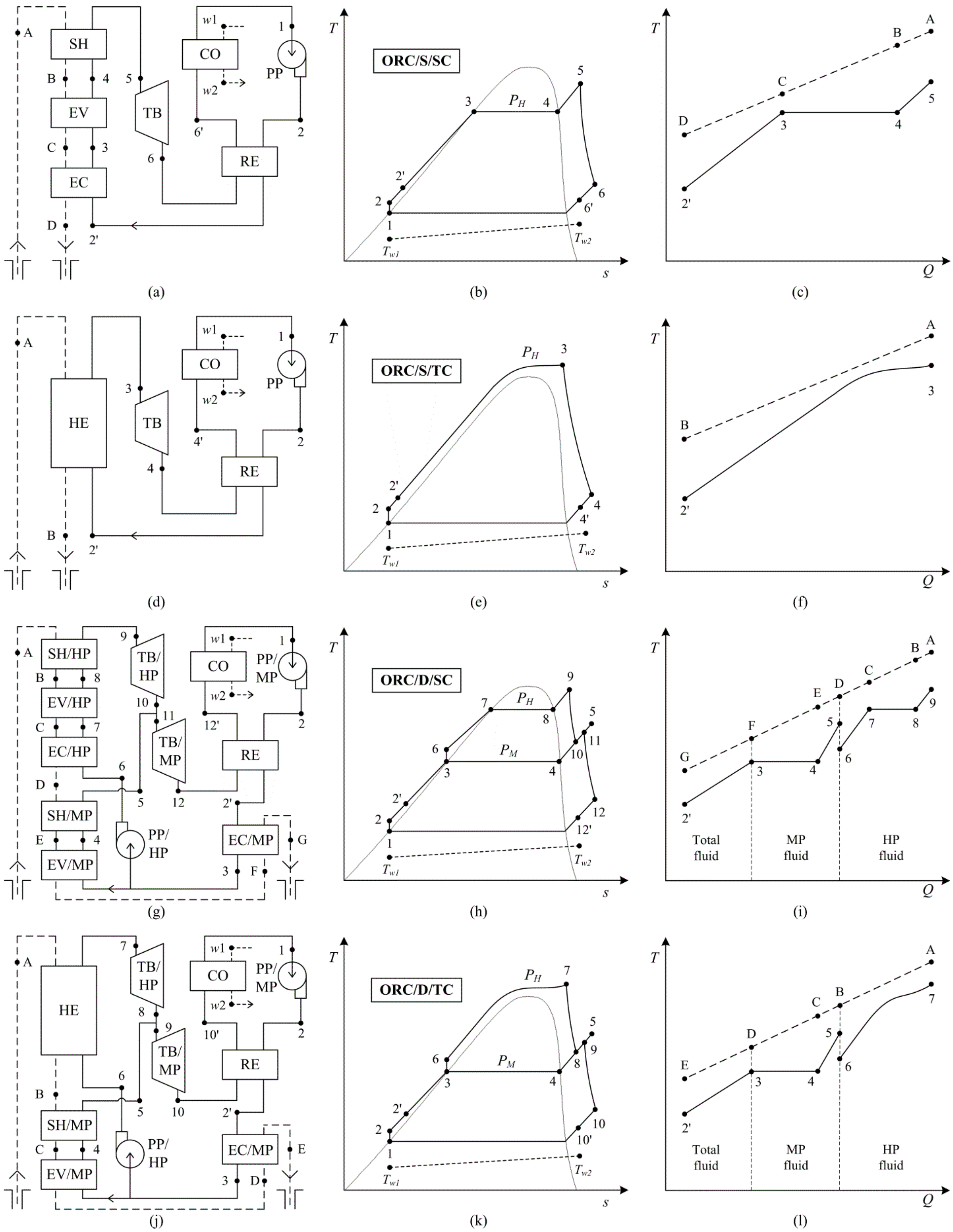

Figure 2.1. Organic Rankine Cycle designs. ORC/S/SC (a) equipment architecture. (b) thermodynamic diagram. (c) heat exchange. ORC/S/TC (d) equipment architecture. (e) thermodynamic diagram. (f) heat exchange. ORC/D/SC (g) equipment architecture. (h) thermodynamic diagram. (i) heat exchange. ORC/D/TC (j) equipment architecture. (k) thermodynamic diagram. (l) heat exchange.

2.4.5 *Cooling system*

The simulated cooling system used for all cycles presented in this work is a wet cooling tower (WCT) with induced draught, conceptualized in Fig. 2.2. A cooling tower discharges heat in the surrounding air in the form of sensible heat and latent heat by increasing the moisture content of the air draught (Chapter 15.8 in [4]). This cooling system was chosen for its compactness, its close control of cold water temperature and its assured supply of required air.

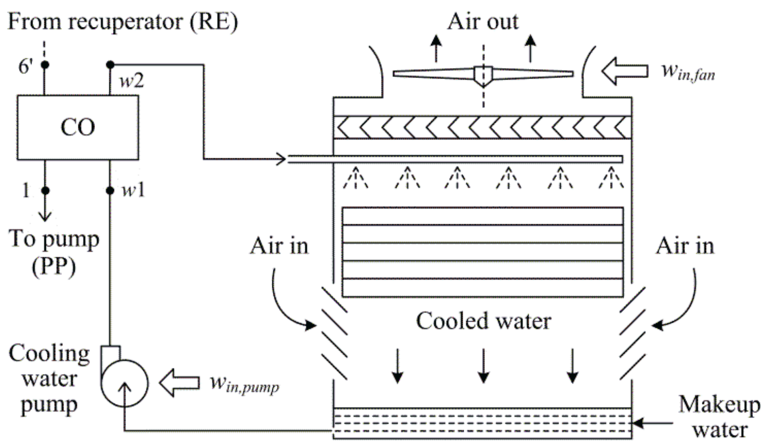

Figure 2.2. Representation of the cooling system layout.

The WCT performance depends on the ambient air wet bulb temperature T_{wb}, as well as on two design parameters, i.e., the approach A and the range r. This work thus employs T_{wb} as the "cold source temperature", because other cold temperatures (such as the condensing temperature or the surrounding dry bulb temperature) would be less convenient in the calculations and in the presentation of the results. Here, the working fluid condensing temperature is determined by the evolution of the cold water temperature, as depicted by the dotted line in Figs. 2.1b, 2.1e, 2.1h and 2.1k, where minimum temperature difference (pinch point) and condenser effectiveness constraints are applied.

Figure 2.2 shows the cooling water trajectory in the ORC/S/SC, as an example. Starting from state {w1}, where $T_{w1} = T_{wb} + A$, the cooling water enters the condenser to absorb the working fluid heat and leaves it at state {w2}, with $T_{w2} = T_{w1} + r$. It then reaches the tower where it is sprayed in fine droplets. The fan at the tower top induces an upwards air flow in which the heat is discharged. The remaining liquid water falls in the basin to be mixed with makeup water and pumped to the condenser again. A WTC requires auxiliary energy consumption due to its fan and cooling water pump, and the calculation method used for predicting the operating specific work is provided in Appendix A.

2.4.6 *Numerical simulations*

The numerical simulations in this work are performed with in-house scripts coded with the programming software MATLAB® [35]. The commercial software REFPROP [34] was used to calculate fluids thermodynamic states. Thorough verifications of the numerical models have been done by calculating specific cases of the four cycles. More specifically, the verifications were performed by comparing the results obtained from the numerical code with those obtained manually. Furthermore, validation of the numerical code was achieved by comparing both subcritical cycles (ORC/S/SC and ORC/D/SC) with other authors' results using the same context.

Table 2.1 lists the inputs required to calculate the specific work output for each cycle and shows the relative difference between the numerical and manually calculated results. Sources of discrepancy include the less precise iterative technique to find the condensing pressure and the states properties during the manual calculation, i.e., thermodynamic tables (Appendix A in [7]) and the "refrigerant calculator" from the software CoolPack [66]. Relative differences of the specific work output δw of less than 4% are obtained for all cycles, justifying that the numerical model works as expected.

Table 2.1. Verification of numerical scripts

Cycle			ORC/S/SC	ORC/S/TC	ORC/D/SC	ORC/D/TC
Input	Fluid		R134a	R134a	R134a	R134a
	T_A	[°C]	150	150	150	150
	T_{wb}	[°C]	20	20	20	20
	P_H	$[\mathrm{MPa}]$	4	5.5	4	5.5
	R_H	$[\mathrm{kg_b/kg_{wf}}]$	0.55	0.55	0.65	0.65
	ε_H	$[-]$	0.75	N/A	0.75	N/A
	P_M	$[\mathrm{MPa}]$	N/A	N/A	2	2
	R_M	$[\mathrm{kg_b/kg_{wf}}]$	N/A	N/A	3.5	3.5
	ε_M	$[-]$	N/A	N/A	0.6	0.6
	r	[°C]	7	7	7	7
	A	[°C]	5	5	5	5
	η_{dry}	$[-]$	0.85	0.85	0.85	0.85
	η_{PP}	$[-]$	0.8	0.8	0.8	0.8
Output	w_{num}	$[\mathrm{kJ/kg_b}]$	37.1169	33.8048	33.4232	32.7357
	w_{hand}	$[\mathrm{kJ/kg_b}]$	36.9262	32.6382	33.2041	33.6412
	δw	$[\%]$	0.51	3.5	0.66	2.8

The model validation (see Table 2.2) is done by comparing model results of Guzović et al. [65] for the example of the potential geothermal field Velika Ciglena (Croatia). The last four inputs of the current model are for the WCT calculations, so they are not used in the work of Guzović et al. (they used a dry cooling system). The mean value of Bjelovar's (main city near the field) relative humidity [67] is chosen to calculate the ambient air wet bulb temperature for the validation. Cooling system power is not considered in the current model specific output for the sake of comparison, since it was not accounted for in [65]. Relative differences between outputs are 22% and 28% for the ORC/S/SC and ORC/D/SC, respectively. The large difference can be explained by the different cooling system and by using the condenser effectiveness ε_{CO} in addition to a minimal approach to dictate P_{CO}. The last hypothesis was confirmed by employing in the present model the same P_{CO} as in [65]: relative differences between models of 2% and 5% for the ORC/S/SC and ORC/D/SC are then calculated. The concordance between the present model and that from the work of Guzović et al. can thus be qualified of acceptable.

Table 2.2. Comparison with the work of Guzović et al., 2014

Cycle			ORC/S/SC	ORC/D/SC
Input	Fluid		Isopentane	Isopentane
	T_A	[°C]	175	175
	T_{db}	[°C]	15	15
	P_H	$[\text{MPa}]$	0.9	1.0864
	P_M	$[\text{MPa}]$	N/A	0.3
	$\dot{m}_{wf,HP}$	$[\text{kg}_{wf}/s]$	80.13	71.9
	$\dot{m}_{wf,MP}$	$[\text{kg}_{wf}/s]$	N/A	28.5
	$\dot{m}_b$	$[\text{kg}_b/s]$	83	83
	η_{dry}	$[-]$	0.85	0.85
	η_{PP}	$[-]$	0.75	0.75
	ϕ	[%]	75	75
	T_{wb}	[°C]	12.46	12.46
	r	[°C]	7	7
	A	[°C]	5	5
Output (Guzović et al.)	P_{CO}	$[\text{MPa}]$	0.11	0.1092
	w	$[\text{kJ/kg}_b]$	63.494	76.759
Output (current model)	P_{CO}	$[\text{MPa}]$	0.169	0.168
	w	$[\text{kJ/kg}_b]$	49.654	55.575

2.5. Optimization

The objective function selected in this study is the power plant specific work output w. It represents the net amount of energy (kJ) produced for each kg of geofluid extracted from the ground. The previous work of Chagnon-lessard et al. [45] uses the term 'specific *power* output' to designate the same physical quantity, but this work employs 'specific *work* output' to be more in line with previous literature. This is the net specific work, where the working fluid feed pump(s) and cooling tower work are subtracted from the turbine(s) work.

Section 2.5.1 provides the definition of the design variables and of the constraints for the four systems, while Section 2.5.2 presents the variables bounds and fixed values and Section 2.5.3 describes the selected optimization algorithm.

2.5.1 *Optimization problem*

Each studied system has its own optimization problem summarized in Table 2.3. The number of design variables varies from three (ORC/S/TC) to seven (ORC/D/SC). They are: (i) the pressure at first turbine inlet P_H, (ii) the mass flow ratio R_H between the brine and the high-pressure working fluid, (iii) the high-pressure superheater effectiveness ε_H, (iv) the pressure at second turbine inlet P_M, (v) the mass flow ratio R_M between the brine and the medium-pressure working fluid, (vi) the medium-pressure superheater effectiveness ε_M, and (vii) the cooling tower range r. Making ε_H and ε_M design variables instead of turbines inlet temperature gives more latitude on the enthalpy of states {5} and {9} and ensures that the value of the effectiveness of the heat exchanger is physically possible.

Several constraints limit the design optimization. Five of them are applied for all ORC designs. First, approach temperatures (pinch point) $\Delta T_{pp,H}$ in the high pressure heater and $\Delta T_{pp,CO}$ in the condenser must be greater than a minimum value ($\Delta T_{tol} = 5\text{ K}$). Next, the effectiveness of the condenser ε_{CO} needs to be lower than a maximum value ($\varepsilon_{\max} = 0.85$). Then, the vapor quality in the turbine must remain above a tolerance value (x_{tol}=0.9) in order to prevent excess blade wear [2]. Finally, the temperature of the geofluid leaving the cycle at state {D}, {B}, {G} or {E} has to be greater than a minimum reinjection temperature ($T_{inj} = 60°\text{C}$).

Other constraints concern specific systems. For cycles comprising a subcritical heater, the effectiveness of economizer(s) ε_{EC} and evaporator(s) ε_{EV} needs to be lower than a maximum value ($\varepsilon_{\max} = 0.85$). For transcritical cycles, a restriction is added to only admit designs with a superheated vapor at the turbine inlet ($x_3 = 1$ and $x_7 = 1$). Last, cycles with dual-pressure heater must have a minimum temperature difference in the medium-pressure heater (EC/MP, EV/MP and SH/MP) $\Delta T_{pp,M}$ greater than ΔT_{tol}.

Table 2.3. Optimization problem of each system

System	Optimization problem	Eq.
ORC/S/SC	$\begin{cases} \text{maximize}(w) \\ \text{varying}(P_H, R_H, \varepsilon_H, r) \\ \text{respecting} \begin{cases} \Delta T_{pp,H} \geq \Delta T_{tol}, & \varepsilon_{EV} \leq \varepsilon_{\max} \\ \Delta T_{pp,CO} \geq \Delta T_{tol}, & x_{\min} \geq x_{tol} \\ \varepsilon_{CO} \leq \varepsilon_{\max}, & T_D \geq T_{inj} \\ \varepsilon_{EC} \leq \varepsilon_{\max} \end{cases} \\ \text{fixed parameters: see Table 2.4} \end{cases}$	(1)
ORC/S/TC	$\begin{cases} \text{maximize}(w) \\ \text{varying}(P_H, R_H, r) \\ \text{respecting} \begin{cases} \Delta T_{pp,H} \geq \Delta T_{tol}, & x_3 = 1 \\ \Delta T_{pp,CO} \geq \Delta T_{tol}, & x_{\min} \geq x_{tol} \\ \varepsilon_{CO} \leq \varepsilon_{\max}, & T_B \geq T_{inj} \end{cases} \\ \text{fixed parameters: see Table 2.4} \end{cases}$	(2)

ORC/D/SC	$\begin{cases} \text{maximize}(w) \\ \text{varying}(P_H, R_H, \varepsilon_H, P_M, R_M, \varepsilon_M, r) \\ \text{respecting} \begin{cases} \Delta T_{pp,H} \geq \Delta T_{tol}, & \varepsilon_{ECs} \leq \varepsilon_{\max} \\ \Delta T_{pp,M} \geq \Delta T_{tol}, & \varepsilon_{EVs} \leq \varepsilon_{\max} \\ \Delta T_{pp,CO} \geq \Delta T_{tol}, & x_{\min} \geq x_{tol} \\ \varepsilon_{CO} \leq \varepsilon_{\max}, & T_G \geq T_{inj} \end{cases} \\ \text{fixed parameters: see Table 2.4} \end{cases}$	(3)
ORC/D/TC	$\begin{cases} \text{maximize}(w) \\ \text{varying}(P_H, R_H, P_M, R_M, \varepsilon_M, r) \\ \text{respecting} \begin{cases} \Delta T_{pp,H} \geq \Delta T_{tol}, & \varepsilon_{EVs} \leq \varepsilon_{\max} \\ \Delta T_{pp,M} \geq \Delta T_{tol}, & x_7 = 1 \\ \Delta T_{pp,CO} \geq \Delta T_{tol}, & x_{\min} \geq x_{tol} \\ \varepsilon_{CO} \leq \varepsilon_{\max}, & T_E \geq T_{inj} \\ \varepsilon_{ECs} \leq \varepsilon_{\max} & \end{cases} \\ \text{fixed parameters: see Table 2.4} \end{cases}$	(4)

2.5.2 *Fixed parameters and design variables*

Table 2.4 presents the values of the fixed parameters, and the range of values for the operating conditions. These values are discussed in this paragraph. First, values for turbomachinery efficiencies, maximum heat exchanger effectiveness and minimum temperature difference are taken from [45]. The minimum tolerated vapor quality has been increased to 0.9 based on the selected value in [68] and on the limit usually applied to turbines [69]. The minimum reinjection temperature T_{inj} is often around 70°C, but this value is specific to the brine composition. A minimal reinjection temperature of 60°C was chosen in the present work to allow reasonable brine heat utilization at low T_A. For example, the Neustadt-Glewe power plant in Germany ($T_A = 99°\text{C}$) reinjects the brine at 60°C [70]. As stated in [71], the size of a cooling tower increases significantly when the approach is reduced. Hence, in this paper, the value of the approach was fixed to 5°C so as to avoid cooling tower that would be too large in practice. The range of the geofluid temperature investigated here corresponds to what could be expected in a low-grade geothermal reservoir. The range of wet bulb temperatures investigated here are the ones recommended by the Cooling Technology Institute (CTI) [72] for the operation of a wet cooling tower. Other assumptions concerning the WCT are not required for the calculation of its power consumption (see Appendix A).

Table 2.4. Values of the fixed parameters in this study

Parameter	Values
Turbines dry efficiency η_{TB}	0.85
Pumps efficiency η_{PP}	0.8
Minimum tolerated vapor quality x_{tol}	0.9
Maximum heat exchanger effectiveness $\varepsilon_{\max}$	0.85
Condenser exchanger effectiveness ε_{CO}	0.85
Supercritical heat exchanger effectiveness ε_{HE}	0.85
Minimum temperature difference ΔT_{tol}	5°C
Minimum reinjection temperature T_{inj}	60°C
Cooling tower approach A	5°C
Range of geofluid inlet temperature T_A	80 – 180°C
Range of ambient air wet bulb temperature T_{wb}	10 – 32°C
Working fluid F	See Table 2.6

Table 2.5 presents the assigned bounds in brackets for each design variable, for each cycle. Pressures are the variables having the largest amount of conditions to be respected in order to lead to viable designs. First, a pressure range of ±0.02 MPa is not allowed around the critical point to guarantee numerical stability in thermodynamic property calculations. Second, the lowest heating pressure inferior bound marked as $P_{\min}$ is the saturated pressure corresponding to 20°C above the heat sink temperature T_{wb}. Third, a range of 0.1 MPa must be respected between P_H and P_M to ensure a minimal amount of work in the high-pressure turbine.

The rest of the bounds are simpler. The ones for the mass flow ratios R_H and R_M were chosen based on observation of results from optimization tests. In each simulation, it was verified that the optimized flow ratios were always within these bounds. Superheaters effectiveness ε_H and ε_M can vary from zero (a saturated cycle) to the maximum value $\varepsilon_{\max}$ set for heat exchangers. Finally, the inferior bound of the cooling range r is the one recommended by the CTI [72], 2.2°C, rounded up to 3°C, and its superior bound of 10°C corresponds to what is recommended in Chapter 13 of [4].

Table 2.5. Bounds of design variables

Design variable		ORC/S/SC	ORC/S/TC	ORC/D/SC	ORC/D/TC
P_H	$[\mathrm{MPa}]$	$[P_{\min} : P_{cr} - 0.02]$	$[P_{cr} + 0.02 : 20]$	$[P_M + 0.1 : P_{cr} - 0.02]$	$[P_{cr} + 0.02 : 20]$
R_H	$[\mathrm{kg_b/kg_{wf}}]$	$[0.05 : 4]$	$[0.05 : 4]$	$[0.05 : 4]$	$[0.05 : 4]$
ε_H	$[-]$	$[0 : 0.85]$	N/A	$[0 : 0.85]$	N/A
P_M	$[\mathrm{MPa}]$	N/A	N/A	$[P_{\min} : P_H - 0.1]$	$[P_{\min} : P_{cr} - 0.02]$
R_M	$[\mathrm{kg_b/kg_{wf}}]$	N/A	N/A	$[0.5 : 7]$	$[0.5 : 7]$
ε_M	$[-]$	N/A	N/A	$[0 : 0.85]$	$[0 : 0.85]$
r	[°C]	$[3 : 10]$	$[3 : 10]$	$[3 : 10]$	$[3 : 10]$

2.5.3 *Optimization algorithm*

Two algorithms have been investigated as candidates for the optimization task. The first is the function *fmincon.m* with the "interior-point" algorithm from the Matlab Optimization Toolbox [37]. The second is an in-house function based on the Particle Swarm Optimization (PSO), a method rising in popularity in the field of thermodynamic cycles. The first algorithm (*fmincon.m*) failed to deliver global maxima due to its lack of exploratory capacity in a given situation. The second one (PSO) was able to find near-optimum solutions within three attempts, and thus, it is the method used for this work.

The PSO algorithm is a metaheuristic developed by Kennedy and Eberhart [73] recognized for its searching ability over a large space of contender solutions. This principle has been implemented in MATLAB with the help of Yarpiz tutorials [74]. The technique in Clarke et al. [36] was also used to ensure that constraints are respected in the optimal solution, i.e., by assigning to unfeasible designs a lower specific work output than the worst performing feasible design by post-treatment. The PSO control parameters used in this work are: (i) stop criterion: relative error of 10^{-5} between iterations j and $j-3$; (ii) maximum number of iterations: 40; (iii) swarm size: $7 \cdot n_{dv}{}^{2}$, where n_{dv} is the number of design variables; (iv) inertia coefficient: 1; (v) damping coefficient: 0.75; (vi) personal acceleration coefficient: 1; (vii) social acceleration coefficient 1.25. Three optimization runs were done systematically for each set of geofluid temperature T_A and wet bulb ambient air temperature T_{wb}, and in the end, the one with the highest maximized specific work was retained.

2.6. Results and discussion

The optimization methodology described in Section 2.5 was applied to the four systems presented in this paper, and for a large amount of operating conditions (i.e., a large amount of combination of T_A and T_{wb}). More specifically, optimization were performed for brine temperature T_A from 80 and 180°C (by 5°C increment), and for the ambient air wet bulb temperature T_{wb} from 10 to 32°C (by 2°C increment). The 20 working fluids investigated in this paper are listed in Table 2.6. These 20 fluids were chosen because they were the best performing fluids in a previous work [45]. Table 2.6 also provides their critical pressure, critical temperature, maximum temperature of applicability and Global Warming Potential (GWP-100 years values from the Fifth Assessment Report of the Intergovernmental Panel on Climate Change [75]). To summarize, a total of 15,864 scenarios (21 T_A values × 12 T_{wb} values × 20 fluids × 4 cycles – 4296 infeasible cases) were optimized to obtain the figures presented below. Optimal designs calculated condensing pressure ranging from 3 to 16 atm, thus appropriate for technical implementation.

Table 2.6. Selected fluids and their properties

Fluid	P_{cr} [MPa]	T_{cr} [K]	$T_{\max}$ [K]	GWP
Isobutene	4.0098	418.09	550	< 3
Isobutane	3.6290	407.81	575	< 3
Propane	4.2512	369.89	650	< 3
Propylene	4.5550	364.21	575	< 3
R12	4.1361	385.12	525	10200
R22	4.9900	369.30	550	1760
R32	5.7820	351.26	435	677
R115	3.1290	353.10	550	7670
R124	3.6243	395.43	470	527
R125	3.6177	339.17	500	3170
R134a	4.0593	374.21	455	1300
R152a	4.5168	386.41	500	138
R218	2.6400	345.02	440	8900
R227ea	2.9250	374.90	475	3350
R236fa	3.2000	398.07	400	8060
R245fa	3.6510	427.16	440	858
R1234yf	3.3822	367.85	410	< 1
R1234ze(E)	3.6349	382.51	420	< 1
RC318	2.7775	388.38	623	9540
RE245cb2	2.8864	406.81	500	654

2.6.1 *ORC with single-pressure heater results*

This section displays the combined results of ORC/S/SC and ORC/S/TC. In other words, it presents the results of the best performing cycle for each combination of T_A and T_{wb} when considering only the single-pressure heater designs. Figure 2.3 shows the maximized specific work output $w_{\max}$ in the form of contour lines (Fig. 2.3a), the best working fluid (Fig. 2.3b) and the cycle leading to the highest $w_{\max}$ (Fig. 2.3c) all with respect to the brine inlet temperature (x-axis) and the ambient air wet bulb temperature (y-axis). Each datapoint or 'pixel' in the charts describes the output of the best fluid/cycle scenario.

Figure 2.3a shows an expected trend where more power is produced for a warmer hot source and a cooler cold source. As indicated in Section 8 of [45], it can be shown based on thermodynamics reasoning that $w_{\max}$ has a quadratic tendency with the form:

$$w_{\max} \cong a\left(x-b\right)^2 \qquad (2.5)$$

where x is the temperature difference between the hot source and the cold source. In, [45] $x = T_A - T_{condenser}$. However, in the present work, the driving temperature difference is $x = T_A - T_{wb}$. A best fit was done by finding the value of coefficients a and b in Eq. (5) that leads to the lowest difference with the numerical results of Fig. 2.3a. With a mean relative error of 4%, the following coefficients were found:

$$\begin{aligned} a &= 3.5709 \\ b &= 23.654 \end{aligned} \qquad (2.6)$$

Thus, the maximized specific work output of a single-pressure heater ORC employing a WCT (accounting for feed pump and WCT parasitic losses) can be estimated by the following equation:

$$w_{\max} \cong 3.5709\left(T_A - T_{wb} - 23.654\right)^2 \qquad (2.7)$$

Among the 20 candidate fluids listed in Table 2.6, Fig. 2.3b indicates that 13 of them lead to the highest specific work for at least one combination of T_A and T_{wb}: R218, R125, R115, R227ea, R32, R1234yf, RC318, R134a, R22, R12, R124, RE245cb2 and R152a. Among these 13 fluids, 7 are retrograde fluids (presence of positive saturated gas slope in their T-s diagram), and 6 are normal fluids (saturated gas slope negative everywhere in their T-s diagram). Normal and retrograde fluids are discussed in DiPippo [2], for example. It was observed that the critical temperature associated to the optimal fluid shown in Fig. 3b increases alongside the value of T_A, the lower being 66.02°C for R125 and the larger being 133.66°C for RE245cb2.

Figure 2.3c presents the best cycle between the ORC/S/SC and ORC/S/TC. The optimal regime for retrograde fluids (except for R115, R1234yf and 124) is subcritical, while normal fluids are best used with a transcritical regime (and also for R125, when T_A is sufficiently high). This phenomenon could be explained by looking at inlet and outlet turbine enthalpies, since their difference dictates the gross specific work of the plant.

It was generally observed that the optimal design for retrograde fluids in a subcritical cycle includes none to small superheater use. Indeed, keeping the turbine outlet state closer to the saturated gas line and reducing mass flow ratio is more advantageous. In the optimal design of transcritical cycles, the turbine inlet state has a greater temperature and entropy, but a not much higher enthalpy. The little gain in enthalpy then does not compensate for the much higher outlet enthalpy (since the entropy is greater), in comparison with the subcritical cycle. In the case of the three retrogrades optimal fluids used in transcritical cycle (i.e. R115, R1234yf and 124), they are less affected by this phenomenon due to their rather vertical (or isentropic) saturated gas slope in their T-s diagram. For normal fluids, a typical optimal design positions the turbine outlet right on the gas saturated line to avoid the efficiency loss caused by the liquid droplets. The enthalpy drop is then greater with a transcritical regime.

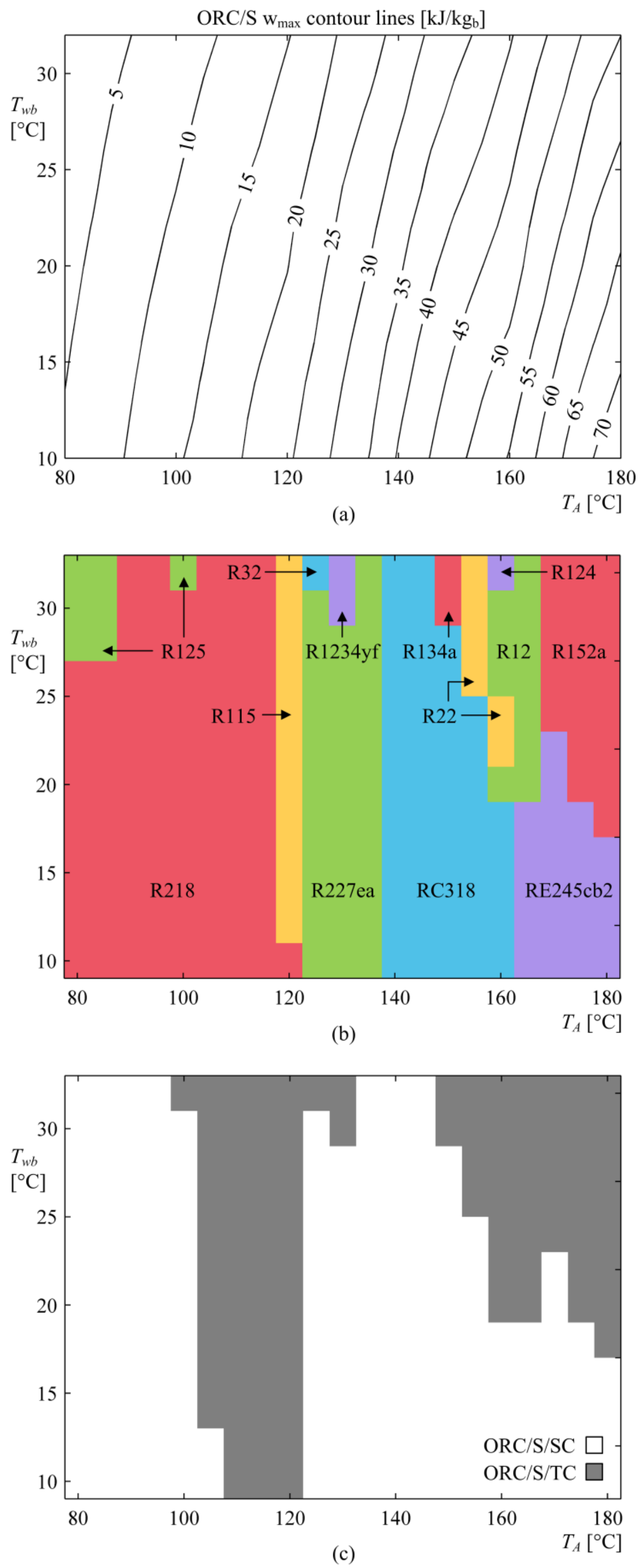

Figure 2.3. Optimization results of ORC/S/SC and ORC/S/TC with respect to brine temperature (x – axis) and to cold sink temperature (y – axis). (a) Maximal specific power contour lines. (b) Optimal working fluid. (c) Optimal regime.

Figure 2.4 presents the corresponding values of the four optimized design variables. The purpose of this figure is to reveal their orders of magnitude. Dotted lines mark the change of working fluid, where drastic behavior changes may occur. Other radical changes sometimes indicate the switch of optimal cycle type, which are not delineated for a greater visibility (please refer to Fig. 2.3c for the optimal cycles). Figs. 2.4a, 2.4b and 2.4c display straightforward results data for the optimized inlet turbine pressure, mass flow ratio and superheater efficiency. Figure 2.4d reveals that the best design does not always involve the maximum cooling tower range. For normal fluids (blue zone in the top right corner), or when T_{wb} is high, a lower range r allows the working fluid to exit the turbine at a lower pressure, where the additional enthalpy drop compensates the supplementary cooling tower load. Depending on the working fluid and operating temperatures, the range is thus a parameter to choose with care when employing a wet cooling tower.

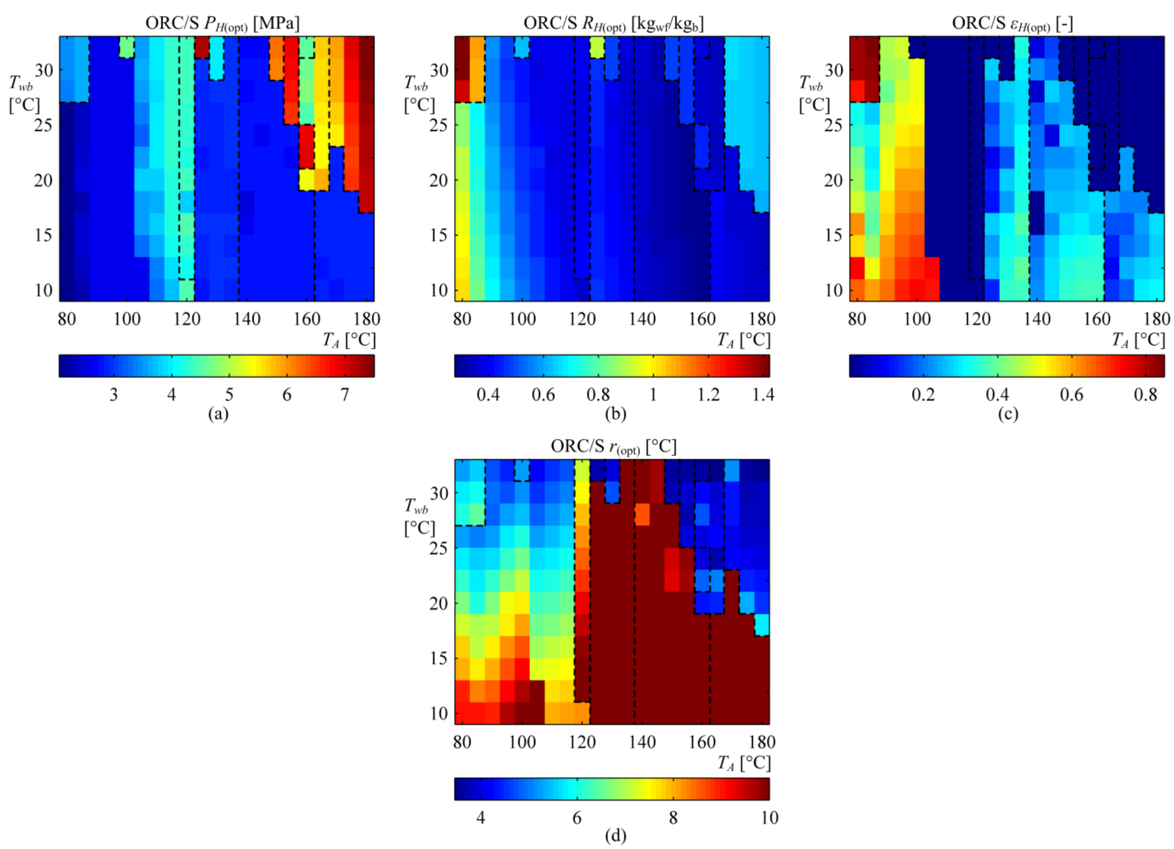

Figure 2.4. Optimized design variables contours lines for ORC/S/SC and ORC/S/TC with respect to brine temperature (x – axis) and to cold sink temperature (y – axis). (a) Turbine inlet pressure P_H. (b) Mass flow ratio R_H. (c) Superheater effectiveness ε_H. (d) Wet cooling tower range r.

2.6.2 *ORC with dual-pressure heater results*

This section displays the combined results of ORC/D/SC and ORC/D/TC. In other words, it presents the results of the best performing cycle for each combination of T_A and T_{wb} when considering only the dual-pressure heater designs.

Figure 2.5 presents the maximized specific work output $w_{\max}$ (Fig. 2.5a), the best working fluids (Fig. 2.5b) and the cycle leading to the highest $w_{\max}$ (Fig. 2.5c). The tendency of the maximized specific work output is once again quadratic. The best fit done to find coefficients of Eq. (2.5) with a mean relative error of 4% gives:

$$w_{\max} \cong 3.4527\left(T_A - T_{wb} - 20.564\right)^2 \tag{2.8}$$

Fig. 2.5b shows that only 5 fluids stand out by leading to the highest specific work for at least one combination of T_A and T_{wb}: R218, R115, R227ea, RC318 and RE245cb2. They all have a retrograde thermodynamic shape and the corresponding critical temperature increases with respect to the value of T_A. Their bell shapes in the T-s diagram of Fig. 2.6 (at scale) are overlapping and fairly similar.

The chart in Fig. 2.5c displays the corresponding optimal regime. When looking at Fig. 2.5b and 2.5c, it may be observed that for each given optimal fluid in Fig. 2.5b, the optimal regime passes from the subcritical regime to the transcritical regime as T_A (x-axis) increases in Fig. 2.5c. The exception is R115, which has an optimal design with a transcritical regime everywhere. This could be interpreted by its saturated gas T-s line being more isentropic than the others, and as discussed in Section 2.6.1, normal and isentropic fluids tend to perform better with a transcritical regime.

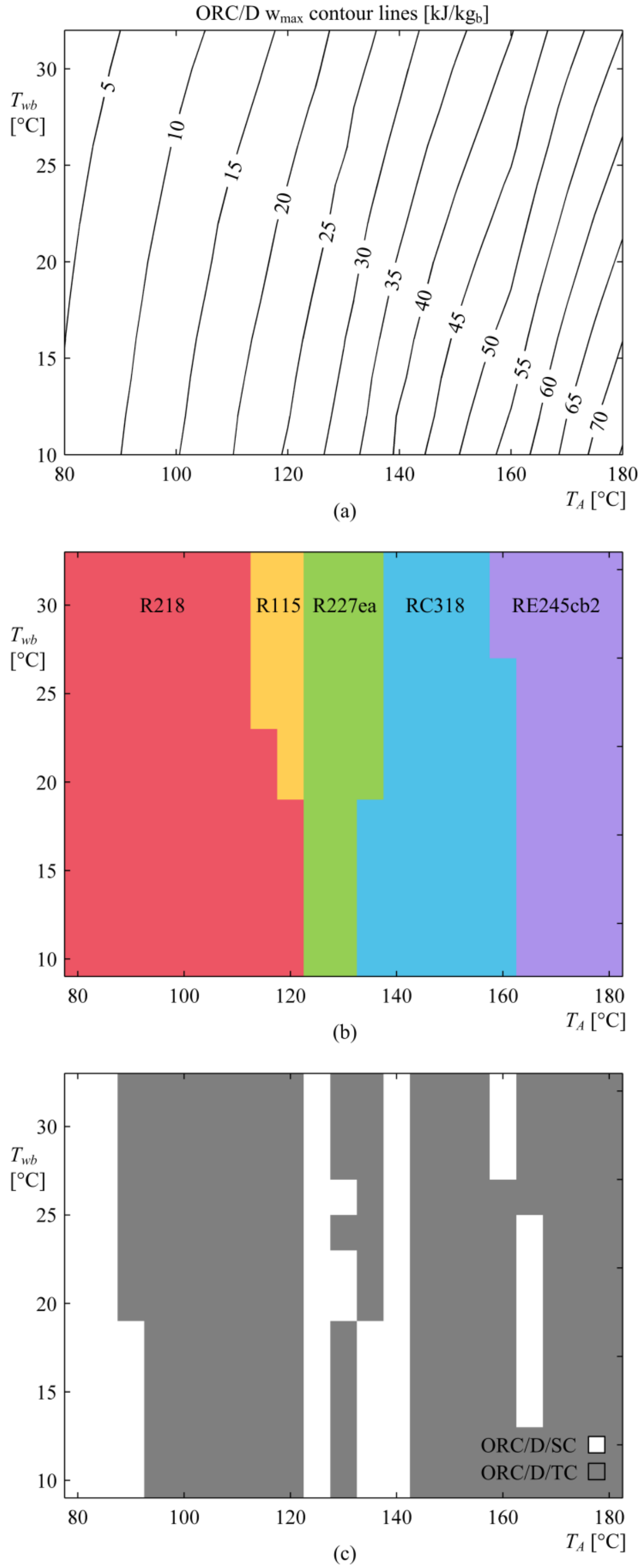

Figure 2.5. Optimization results of ORC/D/SC and ORC/D/TC with respect to brine temperature (x – axis) and to cold sink temperature (y – axis). (a) Maximal specific power contour lines. (b) Optimal working fluid. (c) Optimal regime.

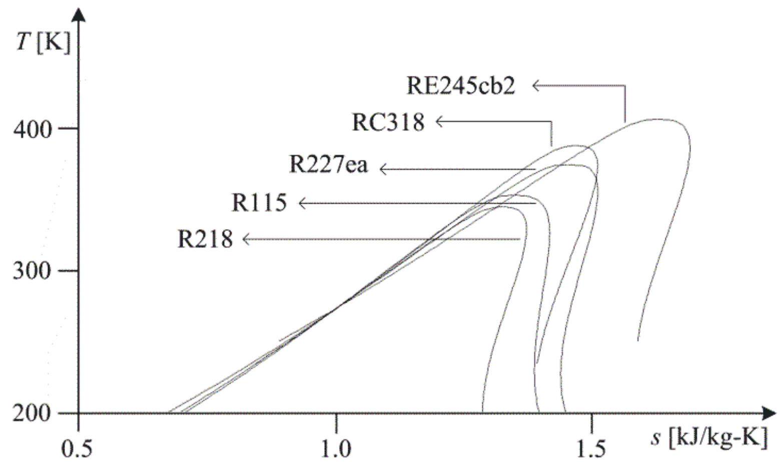

Figure 2.6. T-s diagram of the five optimal fluids for the dual-pressure ORC cycles of Fig. 2.5b.

Figure 2.7 gathers the corresponding values of the seven optimized design variables. Pressure at first turbine inlet (Fig. 2.7a) and mass flow ratio between brine and high-pressure working fluid (Fig. 2.7b) are linked together, that is, a pressure increase leads to a mass flow ratio increase since more heat from the brine is then needed (as a reminder, $R = \dot{m}_b / \dot{m}_{wf}$). High-pressure superheater effectiveness (Fig. 2.7c) is applicable only for the ORC/D/SC, thus the white area indicates there is no superheater in the cycle.

Figure 2.7f reporting the optimized medium-pressure superheater effectiveness is particularly 'pixelated' since this parameter has less impact on $w_{\max}$ than the other design variables. Indeed, for higher values of ε_M , the additional high-temperature heat transferred before the second turbine inlet increases its outlet temperature as well, when considering a retrograde fluid. Therefore, more heat is exchanged in the recuperator to increase state {2'} temperature, which allows a better use of the heat before the brine reaches T_{inj} . The inverse situation, a lower value of ε_M , is preferred when there is no recuperator in order to stay as close as possible to the saturated gas curve. Hence, the impact of the medium-pressure superheater on $w_{\max}$ is weak when recuperation is included in the cycle. Moreover, its effect is further reduced at high ratio brine/working fluid for the medium-pressure portion (low utilization of the medium-pressure heater), thus the small influence on the state at the second turbine inlet.

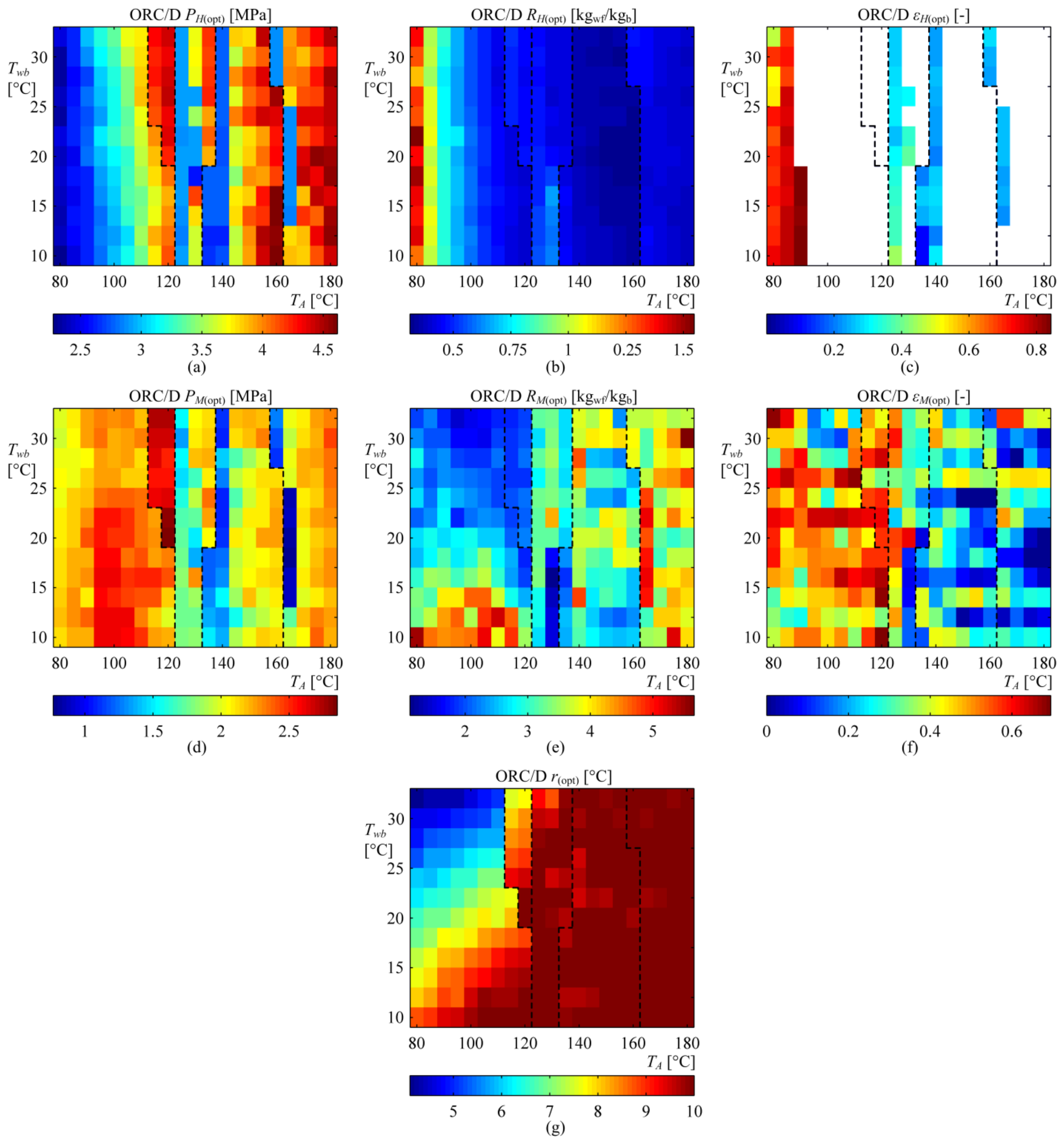

Figure 2.7. Optimized design variables contours lines for ORC/D/SC and ORC/D/TC with respect to brine temperature (x – axis) and to cold sink temperature (y – axis). (a) Pressure at first turbine inlet P_H. (b) Mass flow ratio R_H between brine and high-pressure working, (c) High-pressure superheater effectiveness ε_H. (d) Pressure at second turbine inlet P_M. (e) Mass flow ratio R_M between the brine and the medium-pressure working fluid. (f) Medium-pressure superheater effectiveness ε_M. (g) Cooling tower range *r*.

The optimized cooling tower range shown in Fig. 2.7g matches the superior bound for the best fluids starting from 125°C (R227ea, RC318 and RE245cb2). For R218 and R115, it follows a progression depending on both T_A and T_{wb} to eventually reach the maximum value at high T_A and low T_{wb}. This behavior encountered at low brine temperatures (see Section 2.6.1 for the interpretation) for dual-pressure heater ORCs confirms as well the pertinence of including the cooling tower range in the list of decision variables.

2.6.3 *Comparison of single versus dual-pressure results*

The purpose of this section is to evaluate the differences between the optimal results of Section 2.6.1 (single-pressure heater) and Section 2.6.2 (dual-pressure heater). First, Fig. 2.8a presents the best cycles by combining Fig. 2.3c and Fig. 2.5c. While the ORC/S/SC is not optimal for any temperature cases, the ORCs with dual-pressure heater dominate the figure, with ORC/D/TC being the best cycle for the majority of the cases. However, to what extent increasing the level of complexity (i.e., adding a set of heat exchangers, pump and turbine stage) is beneficial to the specific work output? Figure 2.8b reveals that for low values of T_A and high values of T_{wb} the difference between $w_{\max}$ of dual-pressure and single-pressure heater ORCs can be as high as 19%, while it drops below 4% for $T_A = 140°\text{C}$ and above. The lowest differences are at high values of T_A and T_{wb}, where the ORC/S/TC just barely surpasses the ORC/D/TC.

As a matter of fact, Fig. 2.7e is a good indicator of how much the dual-pressure system is utilized. The large relative difference in Fig. 2.8b at high values of T_{wb} and low values of T_A corresponds to low $R_{M\,(\text{opt})}$ (strong utilization). At high values of T_A, $R_{M\,(\text{opt})}$ is higher (weak utilization), which leads to a smaller relative difference. One could attempt to determine on the T_{wb} and T_A coordinates where the dual-pressure and single pressure heater ORCs offset each other, but the studied T_A range in the present work is not large enough to identify the shift for all T_{wb} values.

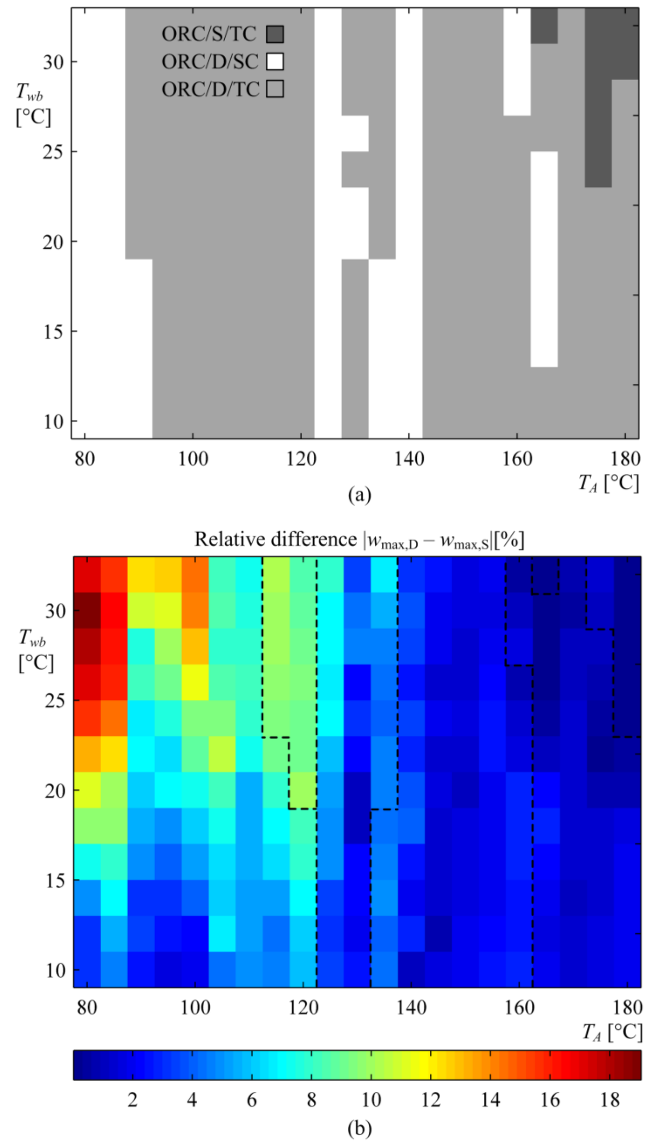

Figure 2.8. (a) Best ORC cycles among the ones studied in this paper. (b) Relative difference between maximized specific work output of ORC/D and ORC/S including both regimes.

What stands out when comparing Figs. 2.3b and 2.5b is the change in the number of optimal fluids (13 and 5 respectively). All normal and isentropic fluids in Fig. 2.3b situated at high values of T_{wb} are not found in Fig. 2.5b, making the dual-pressure heater ORCs optimal only with retrograde fluids. Indeed, what limits their performance in single-pressure heater ORCs is the greater sensible enthalpy of vapor between the turbine output state and the gas saturated state. Having a second turbine or turbine stage where the entropy can be reduced before its input thus shifts the expansion towards the gas saturated line (referring to the T-s diagram) and increases the enthalpy drop. Considering a larger set of working fluids could potentially lead to alternative results, since the twenty working fluids were chosen based on single-pressure heater ORCs results of a previous work [45]. Fluids with greater critical temperature would likely surpass RE245cb2 at high T_A values of the studied range, as proposed by Manente et al. [60].

2.6.4 *Impact of parasitic load*

Results presented in Figs. 2.3a and 2.5a are based on the net specific work and do not reveal the work consumed by the pump(s) and cooling system. Such work is subtracted from the gross power produced by the turbine(s), thus is called parasitic load. Figure 2.9 displays the proportion of the total parasitic load (includes feed pump(s), cooling water pump and tower fan) on the power plant gross power for the optimal designs. It should be noted that the geofluid pump work is not taken into account in the results. Behavior changes can be observed between fluids (separated by dotted lines) and regimes. For example, employing R227ea leads to relatively low parasitic load at $T_A = 125°\text{C}$, but it increases when the optimal regime switches to transcritical due to the rise of the pressure P_H. A similar behavior is seen for RC318 and RE245cb2. Moreover, for both regimes, the optimal strategy to handle the parasitic loads was highly dependent on the working fluid. Indeed, two opposite tendencies occur when moving up along the y-axis: the cooling system demands more input work while the feed pump(s) work is reduced since the pressure drop decreases as well. For some fluids, the increase of the condensation pressure P_{CO} when the cold sink is warmer (i.e. high T_{wb}) is significant enough to nearly offset the change in cooling load. On the other hand, for fluids with lower average pressure drop (R218 and R125) the increase of the cooling system work is more important than the reduction of the pump(s) work. However, despite their higher cooling load, these fluids remain the optimal choice among the twenty fluids studied for brine temperatures values up to 120°C.

The model used effectiveness in heat exchangers calculations, but limiting heat transfer areas for economic reasons would change results. Considering pressures losses, which become larger for an increased heat transfer area, would raise the feed pump(s) work consumption and thus affect the net specific work, particularly for low geofluid temperature cases where the parasitic losses are the most significant.

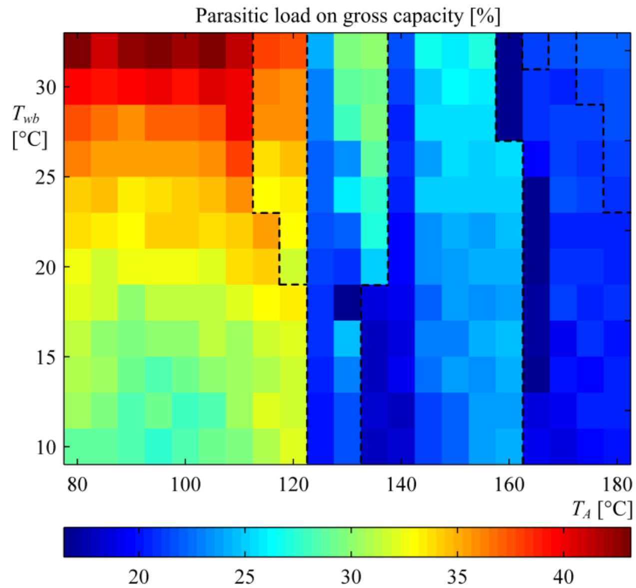

Figure 2.9. Parasitic load over the gross capacity with respect to brine temperature and to cold sink temperature.

2.7. Conclusion

In this paper, four different Organic Rankine Cycles applied to geothermal power plants were numerically simulated and optimized for various operating conditions (inlet brine temperature and ambient air wet bulb temperature): the single-pressure heater ORCs, ORC/S/SC (subcritical) and ORC/S/TC (transcritical), and the dual-pressure heater ORCs, ORC/D/SC (subcritical) and ORC/D/TC (transcritical). Each system includes recuperation of the outlet turbine heat and a wet cooling tower as a cooling system. The objective function was the specific work output, and the design variables depended on the cycle, including operating pressures, mass flows ratios, superheaters effectiveness and the cooling tower range. A total of 20 working fluids were tested in the optimization of each case.

The outputs of the optimization are reported in the form of charts, where one can find the maximized specific work output, best fluids, best regimes, and optimized design variables for the single-pressure heater ORCs and dual-pressure heater ORCs. While a mix of retrograde, normal and isentropic fluids are optimal for single-pressure heater cycles, exclusively retrograde fluids are optimal for dual-pressure heater cycles. Charts presenting the best cycles and the relative difference between a dual-pressure heater and a single-pressure heater in ORCs were also developed. They revealed the dominance of the ORC/D/TC and the pertinence of a dual-pressure heater at low brine temperature and high cold sink temperature. The maximized specific work output was increased by a maximum of 19% compared to ORCs with single-pressure heater, while the difference drops to less than 4% at a brine temperature above 140°C. Finally, the study of the parasitic loads revealed that the best strategy to maximize the net work output varies among working fluids, emphasizing the importance of choosing carefully the cooling tower range.

The work presented in this paper could be extended in various ways. First, the minimum reinjection temperature remained fixed, but other values could be considered to evaluate its impact on the maximized specific work output. While solely a wet cooling tower has been employed here, it would be interesting to simulate natural and dry cooling towers, as well as using complete tower analysis for a more detailed modeling. As seen in Section 2.4.6, a slight difference on the condensing pressure has a great influence on the output, which means the condenser effectiveness is a crucial parameter. A sensitivity analysis could help to find the best cost/performance trade-off. Zeotropic mixtures of fluids could be investigated for more efficient heat absorption, as studied by Noriega Sanchez et al. [76]. Finally, considering other configurations of the heat exchanger network (e.g., parallel heating) could lead to higher maximized work for dual-pressure heater cycles.

2.8. Appendix A: Calculation details for single-pressure heater subcritical organic Rankine cycle

This appendix describes how the net specific output w of the ORC/S/SC was obtained. It should the noted that w does not take into account pressure losses in heat exchangers and electrical losses in the generator. The required inputs include two types of data: the imposed parameters (see Table 2.4) and the design variables (see Table 2.5). This system needs the value of four design variables to calculate the objective function w: (i) the turbine inlet pressure P_H, (ii) the mass flow ratio R_H between the brine and the working fluid, (iii) the superheater effectiveness ε_H, and (iv) the cooling tower range r.

The geofluid enthalpy at state {A} can be obtained from thermodynamic libraries:

State {A}: $$\left.\begin{matrix} T_A \\ \text{sat. liq.} \end{matrix}\right\} \rightarrow h_A \tag{2.9}$$

The first working fluid state that may be calculated is state {4} at the evaporator (EV) output where it is saturated vapor at the known pressure P_H.

State {4}: $$\left.\begin{matrix} P_4 = P_H \\ \text{sat. liq.} \end{matrix}\right\} \rightarrow \begin{matrix} h_4 \\ T_4 \end{matrix} \tag{2.10}$$

To obtain the enthalpies of fluids leaving the superheater (states {5} and {B}) two hypothetical states are specified. At state {5*}, the working fluid reaches the maximum theoretical temperature in the superheater (i.e., T_A), and at state {B*} the geofluid reaches the minimum theoretical temperature in the superheater (i.e., T_4). The enthalpies of these hypothetical states are:

State {5*}: $$\left.\begin{matrix} T_{5*} = T_A \\ P_{5*} = P_H \end{matrix}\right\} \rightarrow h_{5*} \tag{2.11}$$

State {B*}: $$\left.\begin{matrix} T_{B*} = T_4 \\ \text{sat. liq.} \end{matrix}\right\} \rightarrow h_{B*} \tag{2.12}$$

The maximal heat transfer $\dot{Q}_{\max}$ that could occur in the superheater can now be determined. On the geofluid side, the expression for $\dot{Q}_{b,\max}$ is

$$\dot{Q}_{b,\max} = \dot{m}_b (h_A - h_{B*}) = \dot{m}_{wf} R_H (h_A - h_{B*}) = \dot{m}_{wf} \tilde{q}_{b,\max} \tag{2.13}$$

and on the working fluid side, the expression for $\dot{Q}_{wf,\max}$ is

$$\dot{Q}_{wf,\max} = \dot{m}_{wf}(h_{5*} - h_4) = \dot{m}_{wf}\tilde{q}_{wf,\max} \tag{2.14}$$

The value of $\dot{Q}_{\max}$ can be determined by selecting the minimal value between $\tilde{q}_{b,\max}$ and $\tilde{q}_{wf,\max}$, and then using the definition of heat exchanger efficiency provides the expression

$$\varepsilon_H = \frac{\dot{Q}}{\dot{Q}_{\max}} = \frac{\tilde{q}}{\tilde{q}_{\max}} \rightarrow \tilde{q} = \varepsilon_H \tilde{q}_{\max} \tag{2.15}$$

The variable h_5 can be isolated since it is the only unknown and the entropy of state {5} is found as follows:

State {5}:
$$\left.\begin{array}{l} h_5 = h_4 + \varepsilon_H \tilde{q}_{\max} \\ P_5 = P_H \end{array}\right\} \rightarrow s_5 \tag{2.16}$$

In this work, the condensing pressure P_{CO} (pressure at states {6} and {1}) is not given but considered as the lowest pressure respecting the constraints on the condenser: effectiveness lower than $\varepsilon_{\max}$ and approach temperature difference higher than ΔT_{tol} between the working fluid and the cooling water. It means that states {1}, {2}, {2'}, {6} and {6'} must be determined altogether in an iterative or incremental method to find P_{CO}.

Cooling water inlet and outlet temperatures are determined with the wet cooling tower characteristics and the given wet bulb ambient air temperature T_{wb}. The cooling water input temperature in the condenser (state {w1} in Fig. 2) is determined with the definition of the approach A, that to say the difference between this temperature and T_{wb}:

State {$w1$}
$$T_{w1} = T_{wb} + A \tag{2.17}$$

Then, the cooling water outlet temperature (state {w2} in Fig. 2) is known with the range r, i.e. the cooling water temperature difference:

State {$w2$}
$$T_{w2} = T_{w1} + r \tag{2.18}$$

Continuing on the working fluid side, state {1} is first determined knowing the condensing pressure P_{CO}:

State {1} $$\left.\begin{array}{l} P_1 = P_{CO} \\ \text{sat. liq.} \end{array}\right\} \rightarrow \begin{array}{l} h_1 \\ \rho_1 \end{array} \tag{2.19}$$

State {2} is then found calculating the pump work to reach P_H from state {1}:

State {2} $$\begin{array}{l} h_2 = h_1 + w_{PP} \\ w_{PP} = \left(P_H - P_{CO}\right) / \left(\eta_{PP} \rho_1\right) \end{array} \tag{2.20}$$

Next is state {6} at the turbine outlet. The method to determine this state with more accuracy consists in dividing the turbine into several virtual stages, where each stage deals with a small part of the total pressure drop with the appropriate efficiency, determined by the liquid content. When the working fluid is superheated vapor, on uses the turbine dry efficiency η_{dry}, and when it is a saturated mixture, the Baumann efficiency is required to take into account the effect of liquid droplets [30]; [2]. See Chagnon-Lessard et al. [45] for more details on this method.

Stage i outlet enthalpy is thus expressed by Eq. (2.21) when the fluid is superheated vapor, and by the Baumann expression (Eq. (2.22)) when it is a saturated mixture. Stage i enthalpy where the expansion is assumed isentropic is always obtained with Eq. (2.23).

State {i} (dry): $$h_i = h_{i-1} - \eta_{dry}(h_{i-1} - h_{i,s}) \tag{2.21}$$

State {i} (mixture): $$\begin{array}{l} h_i = \dfrac{h_{i-1} - A\left(x_{i-1} - h_{i,f} \big/ \left(h_{i,g} - h_{i,f}\right)\right)}{1 + A \big/ \left(h_{i,g} - h_{i,f}\right)} \\ A = \dfrac{\eta_{dry}}{2}\left(h_{i-1} - h_{i,s}\right) \end{array} \tag{2.22}$$

State $\{i,s\}$: $$\left.\begin{array}{l} P_i \\ s_{i,s} = s_{i-1} \end{array}\right\} \to h_{i,s} \tag{2.23}$$

The enthalpy calculated at the last pressure stage at P_{CO} is h_6, the enthalpy at state {6}, and the turbine work is found with:

$$w_{TB} = \left(h_5 - h_6\right) / R_H \tag{2.24}$$

The condenser cools the working fluid from state {6'} to state {1}, so states {2'} and {6'} at the recuperator outlets are determined with the efficiency method (described for the superheater). T_2 and T_6 are first calculated to determine whether the recuperator can be used:

$$\left.\begin{array}{l} P_2 = P_H \\ h_2 \end{array}\right\} \to T_2 \tag{2.25}$$

$$\left.\begin{array}{l} P_6 = P_{CO} \\ h_6 \end{array}\right\} \to T_6 \tag{2.26}$$

It is important to notice that the authors included a condition on the utilization of the recuperator in the model. For instance, when the difference between T_6 and T_2 is more than 5°C, the recuperator is used. Otherwise, it is not used, i.e., $T_{6'} = T_6$ and $T_{2'} = T_2$, so as to avoid too small temperature differences that would be difficult to achieve in a recuperator. Hypothetical outlet states are:

State {2'*} $$\left.\begin{array}{l} P_{2'*} = P_{P_H} \\ T_{2'*} = T_6 \end{array}\right\} \to h_{2'*} \tag{2.27}$$

State {6'*} $$\left.\begin{array}{l} P_{6'*} = P_{CO} \\ T_{6'*} = T_2 \end{array}\right\} \to h_{6'*} \tag{2.28}$$

The maximum heat transfer in the recuperator is the lowest value between $\tilde{q}_{TB,\max}$ and $\tilde{q}_{PP,\max}$, so the state {6'} may be calculated:

$$\tilde{q}_{TB,\max} = h_6 - h_{6'*}$$
$$\tilde{q}_{PP,\max} = h_{2'*} - h_2 \tag{2.29}$$

State {6'}: $$h_{6'} = h_6 - \varepsilon_H \min\left(\tilde{q}_{TB,\max}, \tilde{q}_{PP,\max}\right) \tag{2.30}$$

In order to determine the net specific output w, the auxiliary power consumption must be subtracted from the gross specific output. In this paper, the considered parasitic loads are the feed pump, the cooling water pump and the cooling tower's fan. The feed pump work is already known by Eq. (2.20) and the others are calculated with a cooling tower analysis. First, the air wet bulb temperature can be read in the psychrometric chart knowing the air dry bulb temperature and relative humidity:

$$\left.\begin{matrix} T_{db} \\ \phi_{air} \end{matrix}\right\} \xrightarrow{Psychrometrics} T_{wb} \tag{2.31}$$

The experimental results of DeFlon (cooling tower patent holder [77]) presented in page 179 of McKelvey and Brooke [78] for mechanical draught towers can be used to estimate the operating power. In the form of a family of curves depending on range and approach, and a correction curve for wet bulb temperatures, they give the work per cooling water volume W_{CT}/V_w, assuming 0.8 pump efficiency. The value obtained in kJ per m^3 of cooling water then needs to be converted in kJ per kg of brine. One may use the heat transfer balance in the condenser (Eq. (2.32)) and two cooling water properties at its mean temperature (Eq. (2.33)) to obtain w_{CT} (corresponding to $w_{in,pump} + w_{in,fan}$ in Fig. 2):

$$\dot{m}_w c_{p,w} r = \dot{m}_{wf}\left(h_{6'} - h_1\right)$$
$$\frac{\dot{m}_w}{\dot{m}_b} = \frac{\left(h_{6'} - h_1\right)}{R_H c_{p,w} r} \tag{2.32}$$

$$\left.\begin{matrix} T_{w,moy} = \left(T_{w1} + T_{w2}\right)/2 \\ P_w = P_{atm} \end{matrix}\right\} \rightarrow \begin{matrix} \rho_w \\ c_{p,w} \end{matrix} \tag{2.33}$$

$$w_{CT} = \frac{W_{CT}}{V_w}\frac{1}{\rho_w}\frac{\dot{m}_w}{\dot{m}_b} = \frac{W_{CT}}{V_w}\frac{\left(h_{6'} - h_1\right)}{\rho_w c_{p,w} R_H r} \tag{2.34}$$

Finally, the net specific output is calculated with:

$$w = w_{TB} - w_{PP} / R_H - w_{CT} \tag{2.35}$$

CHAPITRE 3. MAXIMIZING SPECIFIC WORK OUTPUT EXTRACTED FROM ENGINE EXHAUST WITH NOVEL INVERTED BRAYTON CYCLES OVER A LARGE RANGE OF OPERATING CONDITIONS

3.1. Résumé

La chaleur contenue dans les gaz d'échappement d'un moteur à combustion interne peut être convertie en énergie mécanique en employant un Cycle de Brayton Inversé (IBC). Dans cet article, cinq versions différentes de l'IBC sont modélisées et optimisées pour maximiser leur travail spécifique net : (i) l'IBC de base, (ii) l'IBC avec drainage de l'eau liquide (IBC/D), (iii) l'IBC avec drainage de l'eau liquide et une turbine à vapeur (IBC/D/S), (iv) l'IBC avec drainage de l'eau liquide et un cycle de réfrigération (IBC/D/R), et (v) l'IBC avec drainage de l'eau liquide, une turbine à vapeur et un cycle de réfrigération (IBC/D/S/R). Les trois derniers cycles sont présentés pour la première fois dans la littérature. L'optimisation est exécutée pour une vaste gamme de températures d'entrée des gaz (600 à 1200 K) et de températures du puits de chaleur (280 à 340 K). Parmi les cinq IBCs, l'IBC/D/S/R a le plus grand travail spécifique net pour toute la gamme de températures d'opérations. Une comparaison avec le cycle de Rankine sous-critique et des cycles de Rankine organiques utilisant l'isobutane et le benzène montre qu'un système IBC pourrait être un meilleur choix pour des températures d'opération spécifiques. L'addition d'eau liquide dans l'IBC/D/S/R mène à des solutions optimisées n'utilisant que la turbine à vapeur à des températures élevées d'entrée des gaz, indiquant qu'un cycle de Rankine est mieux approprié pour ces conditions.

3.2. Abstract

The heat contained in internal combustion engine exhaust gases can be converted into mechanical energy by using an Inverted Brayton Cycle (IBC). In this paper, five different versions of the IBC are numerically modeled and optimized to maximize their specific work output: (i) basic IBC, (ii) IBC with liquid water drainage (IBC/D), (iii) IBC with liquid water drainage and a steam turbine (IBC/D/S), (iv) IBC with liquid water drainage and a refrigeration cycle (IBC/D/R), and (v) IBC with liquid water drainage, a steam turbine and a refrigeration cycle (IBC/D/S/R). The three latter are presented for the first time in the literature. The optimization is performed for a wide range of inlet gases temperatures (600 to 1200 K) and heat sink temperatures (280 to 340 K). Among the five IBCs, the IBC/D/S/R has the highest specific work output for the whole range of operating

temperatures. A comparison with the subcritical Rankine cycle and Organic Rankine Cycles using isobutane and benzene shows that an IBC system might be a better choice for specific operating temperatures. Liquid water addition in the IBC/D/S/R leads to optimized designs using only the steam turbine at high inlet gas temperatures, indicating that a Rankine cycle is better suited for these conditions.

3.3. Introduction

Whether for economic reasons or to mitigate global warming, reducing engine fuel consumption is imperative. In internal combustion (IC) engines, approximately 30% of the energy of combustion is lost in exhaust gases [79]. A way to improve their overall energy conversion efficiency is to add a system capable of recovering the waste heat exiting the engine. Although waste heat can also be recovered from other sources, the exhaust gases contain the largest recovery potential [80], and therefore, several waste heat recovery (WHR) technologies for flue gases have been proposed and investigated over the last decades. Some of them are century-old like the turbocharger, but they have been used in practice only recently on engines and require imposing a backpressure on the engine in order to extract thermal energy [81]. Others are more recent like thermoelectric generators, which are receiving more and more attention worldwide thanks to the absence of working fluid and mobile mechanical parts [82]. Yet, among the most studied WHR systems for engines are thermodynamic cycles used as bottoming cycles. The Brayton air cycle is one of the simplest and cost-effective systems [83]. Nevertheless, Organic Rankine cycles (ORC) are presently considered as one of the most promising WHR technologies for their applicability to both high and low-temperature heat sources [84].

A potential bottoming cycle for IC engines that has recently received a lot of attention is the Inverted Brayton Cycle (IBC). Proposed by Wilson [85], it consists in a simple modification to the Brayton Cycle: the exhaust gases expand to a sub-atmospheric pressure, are cooled, and finally compressed to atmospheric pressure. IBC as a bottoming cycle has other applications than engine heat recovery: gas turbine repowering [86], reheat gas turbine [87], low-temperature cogeneration applications [88], microgas turbine [89], just to name a few.

Among the advantages of IBC over other cycles are its simplicity and the availability of the required turbomachinery components. Lower overall efficiency and fouling/corrosion issues are the most commonly mentioned drawbacks of IBCs compared to other technologies, which constitute the challenges currently driving the research efforts related to IBCs. One of the first techno-economic studies of an IBC as an engine heat recovery system was done by Bailey [90] in 1985, where the IBC was referred to as a sub-atmospheric Brayton system. Although the efficiency of the IBC was better than that of pressurized Brayton systems (in which the exhaust provides heat through a heat exchanger to another air stream used as the working fluid), the later was preferred based on cost and potential fouling/corrosion considerations. In 2001, Fujii et al. [91] developed an IBC test rig to demonstrate the concept and measured thermal efficiency values of the order of 1%. This relatively poor performance was due to the low turbine efficiency (~50%), since the turbine had been designed to operate at a larger flow rate than the one used in the test rig.

Selecting the best bottoming cycle for a given application can be quite challenging, which brings to light the need for cycle comparison studies. An influential study by Bianchi and De Pascale [92] compared three bottoming cycles (ORC, Stirling and IBC) for a fixed cold source temperature of 15°C and variable hot source temperatures. In their studies, the ORC offered a specific energy output between 10 and 200 kJ/kg depending on the choice of working fluid and available temperature, whereas the specific energy output of the IBC was in the range 10-70 kJ/kg depending on temperature and condensed water mass fraction. They conclude that “the innovative and not yet developed IBC system is a promising solution but not as performing as the ORC technology, especially in the field of very low temperatures (200–400°C). If instead heat fluxes are available at temperature values above 350–400°C, the IBC technology becomes more interesting in terms of achievable efficiency”.

Despite its observed efficiency often lower than that of ORC, the interest for IBC has continued to grow. Identifying the contexts in which IBCs can be an adequate solution is still an open question and thus, IBCs have been tested in different applications over the last few years. For example, Chen et al. [79] simulated the performance of IBCs when it is coupled with a light-duty automotive engine operating in a real-world driving cycle where the exhaust flow rate varies in time. A reduction of fuel consumption of 3.15% was calculated when the turbine pressure ratio is constantly optimized. Copeland and Chen [93] also showed that IBC is a promising alternative to turbocompounding.

Additionally, another objective of current research on bottoming cycles is to propose improvements or modifications to IBCs that would increase their overall efficiency to a level that would make them more competitive. For example, Fujii et al. [91] proposed an intercooled inverted Brayton cycle or mirror gas turbine concept to improve performance. Kennedy et al. [94] studied the effect of removing condensed water in the exhaust before the compressor. The benefit of this modification is the mass flow rate reduction during gases compression, which improves the overall cycle efficiency.

The present study further develops this idea by proposing two new additional modifications to the IBC and evaluating the associated change of performance. The first modification uses the drained water to perform an open Rankine cycle, where the exhaust gases at the gas turbine outlet heats the water before entering a steam turbine. The second one is the addition of a refrigeration cycle upstream of the separation to increase liquid water formation and obtain a colder temperature at compressor inlet. Determining the best IBC variants requires design optimization to compare maximized performance. While being a promising technology, no open report of IBC optimization for different combinations of temperature conditions (hot and cold sources) was found; hence its most suited applications remain partly unknown compared to other cycles. This study seeks to determine for a large set of temperature conditions how IBC and its variants perform compared to the more widely used Rankine cycles. This work thus investigates and optimizes a total of five variations of the IBC. The first two are the basic IBC and the IBC with liquid water drainage (IBC/D). The three others are novel variations of the IBC/D. More specifically, the first novel cycle (IBC/D/S) sends the separated water to an open Rankine cycle, the second one (IBC/D/R) couples a refrigeration cycle to the IBC/D, and the third one (IBC/D/S/R) couples the IBC/D with the open Rankine cycle and the refrigeration cycle. To summarize, the five systems investigated in this paper are referred to as the IBCs, and they comprise the IBC, IBC/D, IBC/D/S, IBC/D/R, and IBC/D/S/R.

The main goals of the work are to establish new charts that provide guidelines for optimal designs of the IBCs and to compare the performance of the best IBC variants with that offered by well-known Rankine cycle and Organic Rankine Cycles. The analysis presented in this paper covers a large set of operating conditions, i.e., an exhaust temperature from 600 to 1200 K, and a coolant temperature from 280 to 340 K. The objective function to maximize is the specific work output w [kJ/kg], and the design variables depend on the cycle investigated (e.g., operating pressures and utilization rate of the refrigeration system).

The paper is structured as follows: Section 3.4 describes the IBCs and the methodology used to perform the numerical simulations; Section 3.5 explains the modeling method used for each piece of equipment; Section 3.6 describes the optimization problems; Section 3.7 presents the results of the optimization runs by means of design charts; and Sections 3.8 and 3.9, provide example of applications and conclusions.

3.4. Problem statement

A description of the five thermodynamic cycles is first provided in Sections 3.4.1 to 3.4.5 and Section 3.4.6 gives details about the numerical simulations. The systems considered in this paper include two cycles that have already been presented in literature [79] [94]: (i) the basic Inverted Brayton Cycle (IBC) and (ii) the IBC with liquid water drainage (IBC/D). Moreover, three novel cycles are presented in this paper: (iii) the IBC/D with a steam turbine (IBC/D/S), (iv) the IBC/D with a refrigeration cycle (IBC/D/R), and (v) the IBC/D with a steam turbine and a refrigeration cycle (IBC/D/S/R).

3.4.1. *Inverted Brayton Cycle (IBC)*

The Inverted Brayton Cycle is an open cycle built with three main components: an expander, a heat exchanger, and a compressor. An equipment architecture and a thermodynamic diagram of the IBC are given in Fig. 3.1. The exhaust gases exiting the engine enter the IBC at state {1} at atmospheric pressure, expand in the gas turbine (GT) and leave at state {2}. The heat exchanger cools down the gases to state {3} by transferring the heat to a coolant at constant pressure. Part of the water contained in the gases being condensed in some cases, this heat exchanger will be referred to as the condenser (CO) for the rest of the paper. The gas stream is compressed back to atmospheric pressure where it leaves the compressor (CP) at state {4}.

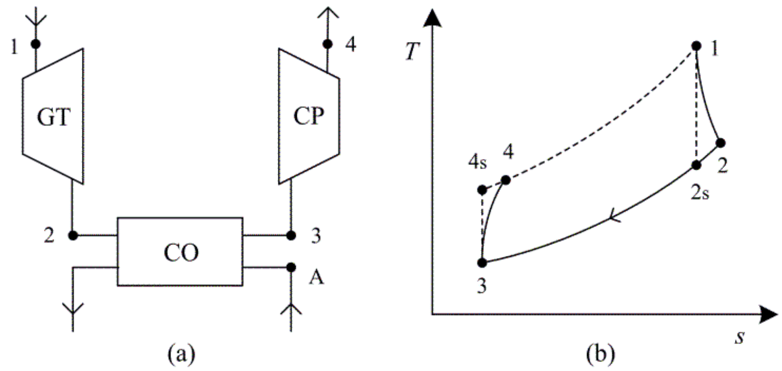

Figure 3.1. Inverted Brayton Cycle (IBC). (a) Equipment architecture. (b) Thermodynamic diagram of exhaust gases.

The fuel used in the upper cycle (engine) is considered to have a hydrogen to carbon ratio equal to 2, and an oxygen to carbon ratio of zero, as for typical hydrocarbon fuels. Assuming a specific humidity of 0.01, the equation for complete combustion considering no excess air is [94]:

$$\begin{aligned} &CH_2 + \frac{3}{2}O_2 + \frac{39}{7}N_2 + \frac{3}{42}Ar + 0.115H_2O \\ &\rightarrow CO_2 + \frac{39}{7}N_2 + \frac{3}{42}Ar + 0.615H_2O \end{aligned} \tag{3.1}$$

It is now possible to calculate molar and mass fractions of each species in the exhaust gases. To complete enthalpy and entropy calculations, the specific heat c_p is determined with the following correlation for ideal gases:

$$\bar{c}_{p,i} = M_i c_{p,i} = M_i \left(a_i + b_i T + c_i T^2 + d_i T^3 \right) \tag{3.2}$$

where $\bar{c}_p$ is the molar specific heat, M the molar mass, c_p the mass specific heat, and letters a_i to d_i are coefficients specific to each species i (see table A.2c of [7]). Eq. (3.2) is used for CO_2, N_2, and vapor H_2O. Ar has a c_p value independent of temperature.

3.4.2. *Inverted Brayton Cycle with liquid water drainage (IBC/D)*

When the gas stream is sufficiently cooled down, condensation occurs in the condenser, and a part of the total water content can be drained before entering the compressor (see Fig. 3.2a). The advantage of this modification is the flow rate reduction in the compressor, leading to a reduced work input for certain conditions. Fig. 3.2b follows the thermodynamic states of the exhaust gases (including water vapor), while Fig. 3.2c shows the water only (liquid and vapor). The exhaust gaseous part undergoes the same evolution as in the IBC, and the liquid water is separated from the gases after state {3} to reach state {6} (or state $\{3_{liq}\}$). It should be noted that the pressure of states {1}, {2}, {4} (or state $\{3_{vap}\}$) and {5} in Fig. 3.2c are the water partial pressure (vapor pressure). State {6} (state $\{3_{liq}\}$) is compressed liquid water at the lowest pressure of the exhaust gases (at states {2}, {3} and {4} in Fig. 3.2b) represented by the line P_2 in Fig. 3.2c. A pump (PP) brings the liquid water to atmospheric pressure at state {7}.

The liquid mass fraction at state {3} is found by first calculating the vapor mass fraction. Using the fact that the pressure ratio is equal to the molar fraction for ideal gases, the vapor pressure P_{vap} can be found with:

$$P_{vap} = P_{tot}\left(N_{H_2O}/N_{tot}\right) \tag{3.3}$$

Then, the saturation pressure P_{sat} tells whether there is liquid water formed or not. When P_{vap} is greater than P_{sat}, the water content at state {3} is larger than what the gas mixture can hold at a given temperature. Thus, a fraction of the water has condensed and can be removed before entering the compressor. The Arden Buck equation for $T > 0$ °C, which is a modified version of the one presented in [95], is used to calculate P_{sat} with an average precision of 0.02%:

$$P_{sat}(T) = 0.61121\exp\left[\left(18.678 - \frac{T}{234.5}\right)\left(\frac{T}{257.14+T}\right)\right] \tag{3.4}$$

The vapor molar fraction in the mixture is found with Eq. (3.5), and the vapor and liquid mass fractions are determined with Eq. (3.6)

$$y_{H_2O,vap} = P_{sat}/P \tag{3.5}$$

$$\begin{aligned} mf_{H_2O,vap} &= y_{H_2O,vap} N_{dry} M_{H_2O} \\ mf_{H_2O,liq} &= mf_{H_2O} - mf_{H_2O,vap} \\ N_{dry} &= \frac{N_{CO_2} + N_{N_2} + N_{Ar}}{1 - y_{H_2O,vap}} \end{aligned} \tag{3.6}$$

where N_{dry} is the number of moles of the species in the mixture apart from water. Eqs. (3.3), (3.5) and (3.6) are taken from Chapter 14 of [7].

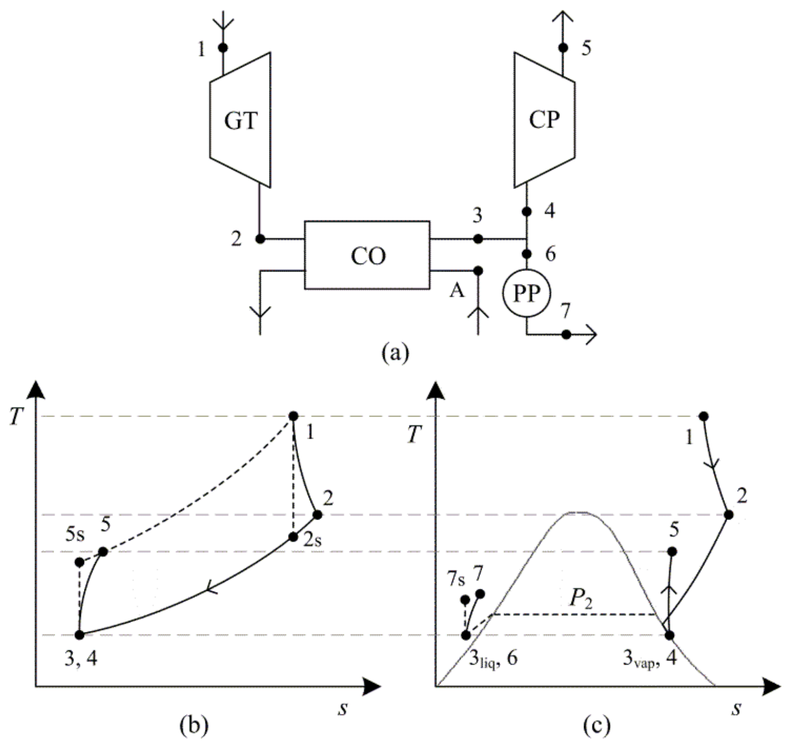

Figure 3.2. Inverted Brayton Cycle with liquid water drainage (IBC/D). (a) Equipment architecture. (b) Thermodynamic diagram of exhaust gases. (c) Thermodynamic diagram of water.

3.4.3. *Inverted Brayton Cycle with liquid water drainage and steam turbine (IBC/D/S)*

Figure 3.3 shows the IBC/D/S, the first novel cycle proposed in this paper. It consists of an IBC with liquid water drainage, where the drained liquid water (state {7} or {4_{liq}} in Fig. 3.3c) flows in an open Rankine cycle to produce work in a steam turbine. More specifically, the condensate is first compressed to state {8} with a pump (PP1 in Fig. 3.3a) and goes through a heat exchanger (EV/S) to receive heat from the exhaust gases at constant pressure and reach a superheated state (state {9}). The vapor is then expended in a steam turbine (ST) and leaves it at state {10}. In order to lower state {10} pressure below atmospheric pressure and produce more work, a condenser (CO/S) brings the water to the saturated liquid state {11} and a second pump (PP2) takes it to atmospheric pressure at state {12}. The achievable pressure at the steam turbine outlet depends on coolant temperature T_A. Solely subcritical open Rankine cycles are considered here.

As for the exhaust gases, their cooling is partly done in the evaporator EV/S and they enter the CO at state {3}. They leave it at state {4}, liquid water is separated to obtain state {5} (and state {4_{vap}} for water), and they are put back to atmospheric pressure at state {6} in the CP. Noticeably, this cycle can only work if there is liquid water formed at state {4} and if pressure and temperature of state {9} are high enough to produce work in the ST. In the model, it was assumed that when the last requirement is not met, the right cycle to use is the IBC/D and that when both requirements are not satisfied, the IBC is the cycle to use.

As this cycle is proposed for the first time in literature, Table 3.4 describes the IBC/D/S thermodynamic states using the optimized design for a specific case of T_1 and T_A.

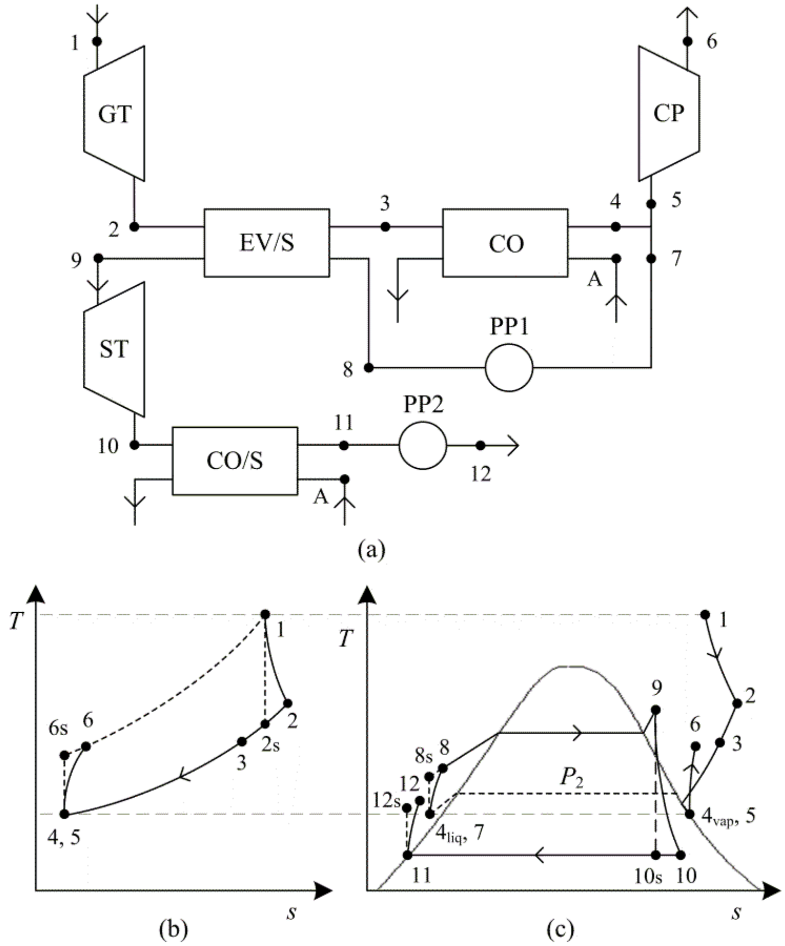

Figure 3.3. Inverted Brayton Cycle with liquid water drainage and steam turbine (IBC/D/S). (a) Equipment architecture. (b) Thermodynamic diagram of exhaust gases. (c) Thermodynamic diagram of water.

3.4.4. *Inverted Brayton Cycle with liquid water drainage and refrigeration cycle (IBC/D/R)*

It may be reminded that the lower the temperature of a fluid at a compressor inlet, the smaller the work needed to reach the compressor outlet pressure. Thus, a refrigeration cycle could be used to cool the gases before entering the compressor. A lower temperature before the compressor may also increase the condensate, which is removed to reduce the mass flow rate hence reducing even more the work consumed.

A vapor-compression cycle is therefore added to the IBC/D just before the drainage, so as to create the IBC/D/R as illustrated in Fig. 3.4a. As in the IBC/D, the gas stream is expanded in the GT until state {2} and is cooled down in the CO to state {3} (see Fig. 3.4b). The refrigerant cools it to state {4} in the evaporator (EV/R), reaching a temperature that depends on the extent to which the refrigeration cycle is used, between T_3 and 273.2 K, corresponding to a 'refrigeration utilization rate' of 0% to 100%, respectively. The separated liquid water (states {7} and {4_{liq}}, see Fig. 3.4c) and the gaseous part (states {5} and {4_{vap}}) are brought back to atmospheric pressure by the PP to state {8}, and the CP to state {6}, respectively.

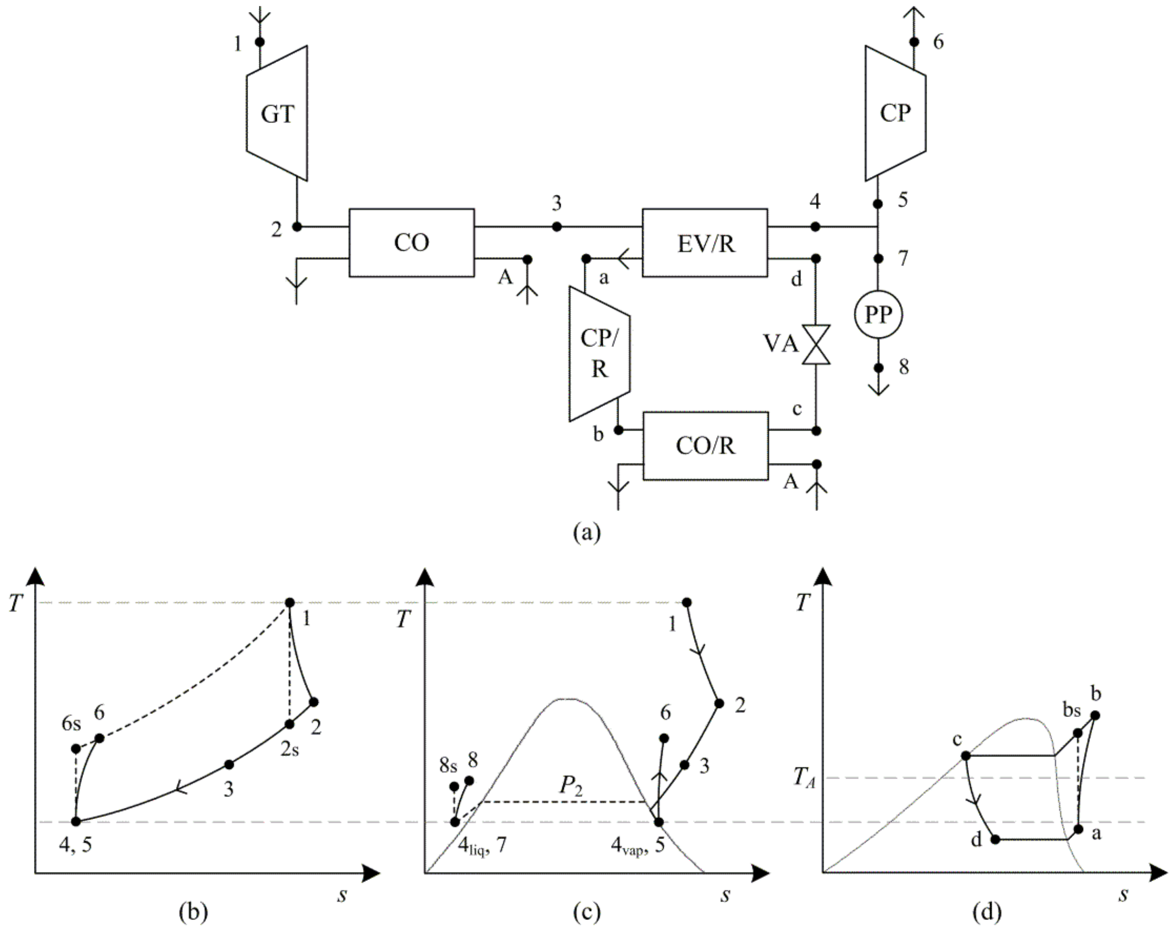

Figure 3.4. Inverted Brayton Cycle with liquid water drainage and refrigeration cycle (IBC/D/R). (a) Equipment architecture. (b) Thermodynamic diagram of exhaust gases. (c) Thermodynamic diagram of water. (d) Thermodynamic diagram of refrigerant.

The refrigerant undergoes a basic vapor-compression cycle. It is evaporated at constant pressure in the evaporator (EV/R) to reach state {a} (see Fig. 3.4d) that has a temperature 3 K higher than the saturated state to ensure it is superheated. The vapor is compressed by a compressor (CP/R) to state {b}, and then it is condensed to saturated liquid (state {c}) at constant pressure in a condenser (CO/R). Finally, the refrigerant goes through an isenthalpic valve to reach state {d} and returns in the EV/R. The fluid employed in this work is R134a, which is widely used and proved to be one of the best fluids in the conditions considered here [96].

Likewise, the IBC/D/R being a new cycle, Table 3.5 describes its optimized design thermodynamic states for a specific case of T_1 and T_A.

3.4.5. *Inverted Brayton Cycle with liquid water drainage, steam turbine and refrigeration cycle (IBC/D/S/R)*

The last novel cycle is the IBC/D/S/R, which consists of an IBC with liquid water drainage, an open Rankine cycle and a refrigeration cycle, as shown in Fig. 3.5a. This cycle increases the liquid water production to a flow rate that would not be possible in the IBC/D/S, thus developing greater power in the steam turbine. Now, the exhaust gases are cooled down by three heat exchangers. The first one (EV/S) uses the hotter part of the exhaust gases after the GT to evaporate the water before the ST, leaving the gaseous mixture at state {3} (see Fig 3.5b). The second heat exchanger CO brings the exhaust gases to state {4}, at a temperature near that of the coolant. Finally, the third heat exchanger EV/R cools the gases to state {5} at a temperature between T_4 and 273.2 K. The refrigeration cycle is the same as the one in the IBC/D/R (see Fig. 3.5d) using R134a. The gaseous part at state {6} (and state {5_{vap}}) is compressed to state {7} and the liquid water at state {8} (state {5_{liq}}) undergoes the same open Rankine cycle than in the IBC/D/S (see Fig. 3.5c) leaving the system at state {13}. It should be noted that the pressure P_2 is lower in Fig. 3.5c than in Fig. 3c because the refrigeration cycle helps reaching lower condensing temperatures. Incidentally, the outlet pressure of the ST is below P_2 in Fig. 3.3c and above P_2 in Fig. 3.5c. Figures 3.1 to 3.5 are not to the scale.

As the last novel cycle, the IBC/D/S/R thermodynamic states are detailed in Table 3.6 using the optimized design for a specific case of T_1 and T_A

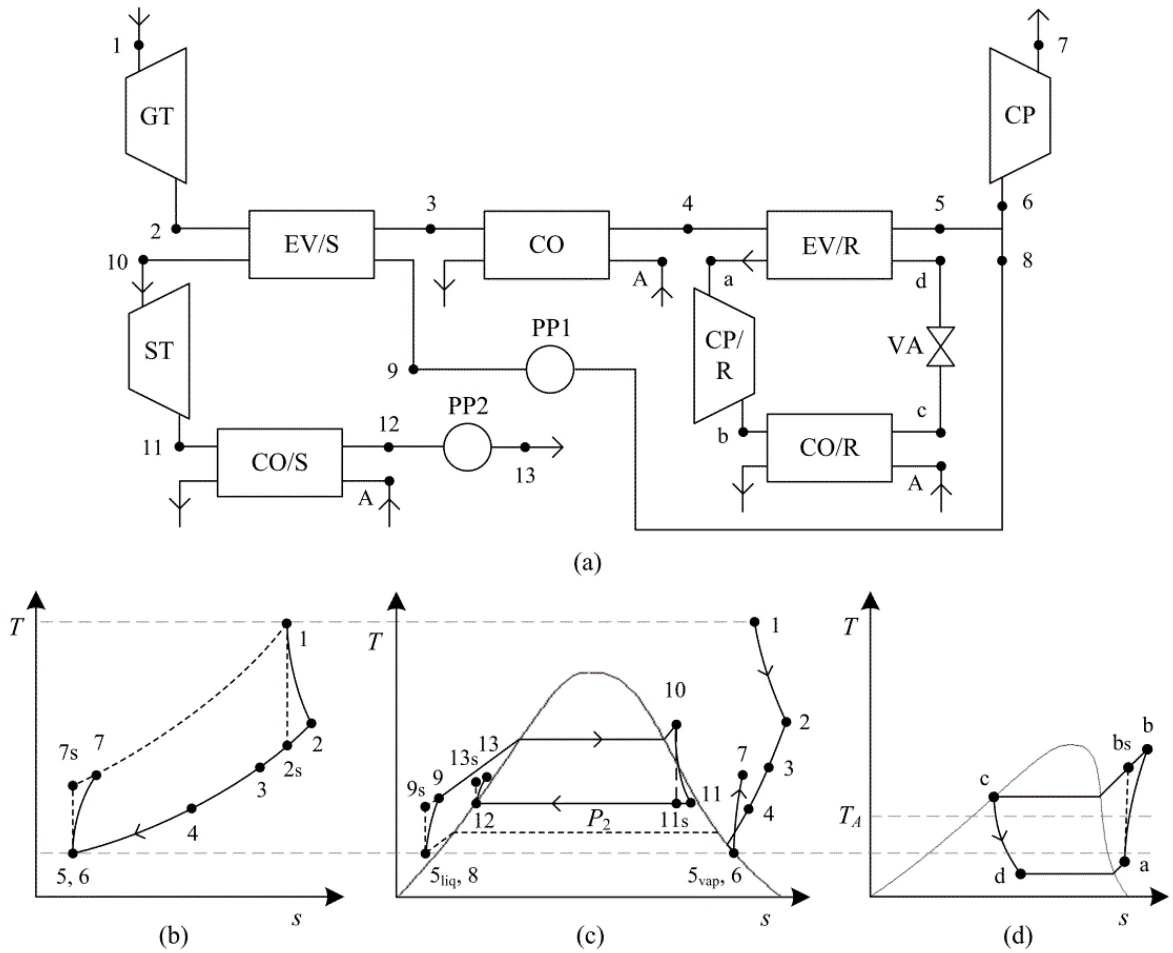

Figure 3.5. Inverted Brayton Cycle with liquid water drainage, steam turbine and refrigeration cycle (IBC/D/S/R). (a) Equipment architecture. (b) Thermodynamic diagram of exhaust gases. (c) Thermodynamic diagram of water. (d) Thermodynamic diagram of refrigerant.

3.4.6. *Numerical simulations*

The modeling and numerical simulations in this project are performed with in-house MATLAB® scripts [35]. The open-source thermophysical property library CoolProp [97] [98] was used to evaluate thermodynamic properties of water and R134.

The present numerical model has been validated by comparing the results with those obtained by two other authors. Available information was found in the work of Fujii et al. (2001) [91] for the IBC. Considering an inlet exhaust gases temperature T_1 of 1140 K, a coolant temperature T_A of 293 K, a turbine expansion ratio of ~1.72 ($P_2 = 59$ kPa), and turbine and compressor isentropic efficiencies of ~0.53 and ~0.69 respectively, the authors' experiment led to a specific work output of ~12.3 kJ/kg (no uncertainty analysis was available in this work for the experimental measurement). Using the same parameters, the model gives a specific work output of 11.5 kJ/kg, corresponding to a 6.5% relative difference. With $T_1 = 500°C$, $T_A = 15°C$ and a turbomachinery polytropic efficiency value of 0.8, Figs. 7a and 10a in the simulation work of Bianchi and De Pascale (2011) [92] show specific work outputs of 25 kJ/kg for the IBC ($P_2 = 30$ kPa), and 35 kJ/kg for the IBC/D ($P_2 = 40$ kPa, $X_{H_2O,in} = 0.1$). Using an isentropic turbomachinery efficiency of 0.8, the present model gives specific work outputs of 24.7 kJ/kg (IBC) and 33.9 kJ/kg (IBC/D), which corresponds respectively to a relative difference of 1.2% and 3.2%. Therefore, the agreement between the present model and results from literature can be qualified of good.

3.5. Equipment modeling methodology

The models developed for this work take into account two features that are often overlooked: the specific heat dependency on temperature, and the evolution of each species' mass fraction. For example, liquid water can form during the cooling of the exhaust gas, thus changing the mixture composition at the outlet. Sections 3.5.1 to 3.5.5 explain the modeling methodology for the gas turbine, condenser, compressor, steam turbine, and other heat exchangers. Section 3.5.6 presents the main conditions and assumptions.

3.5.1. *Gas turbine*

The gas turbine is the first device encountered by the exhaust gas stream. The water content stays completely in vapor state for the entire expansion, for all external conditions considered in this paper. The specific work produced by the gas turbine may be expressed by the enthalpy difference between states {1} and {2}, or the isentropic enthalpy evolution multiplied by the gas turbine efficiency:

$$w_{GT} = h_1 - h_2 = \eta_{GT}(h_1 - h_{2s}) \tag{3.7}$$

By virtue of the Gibbs-Dalton Law for ideal gases [99], the isentropic enthalpy difference can be found for each component and then added together considering their mass fraction mf_i. Each individual enthalpy difference is calculated with the specific heat correlation of Eq. (3.2):

$$\begin{aligned} h_{1,i} - h_{2s,i} &= \int_{T_{2s}}^{T_1} c_{p,i}(T)dT \\ &= a_i(T_1 - T_{2s}) + \frac{b_i}{2}(T_1^2 - T_{2s}^2) + \frac{c_i}{3}(T_1^3 - T_{2s}^3) + \frac{d_i}{4}(T_1^4 - T_{2s}^4) \\ &= \Delta h_i(T_1, T_{2s}) \end{aligned} \tag{3.8}$$

For the sake of conciseness, the method presented in Eq. (3.8) will henceforth be expressed as $\Delta h_i(T_1, T_2)$. Initial temperature T_1 is a known parameter and the method to find T_{2s} involves the entropy variation. According to Gibbs' relation for a closed and reversible system, and assuming an ideal gas, one finds

$$\Delta s = s_2^{\circ} - s_1^{\circ} - R\ln\left(P_2/P_1\right) = 0 \tag{3.9}$$

where R is the ideal gas constant for the mixture, and initial and final pressures are known. The procedure to estimate the absolute entropy variation $\left(s_2^{\circ} - s_1^{\circ}\right)$ is similar to that used above for the enthalpy variation. The absolute entropy variation only depends on T_1 and T_{2s}, and can be calculated by summing the absolute entropy variation of each species weighted by their mass fraction mf_i:

$$\begin{aligned} s_{2,i}^{\circ} - s_{1,i}^{\circ} &= \int_{T_1}^{T_{2s}} \frac{c_{p,i}(T)}{T} dT \\ &= a_i \ln\frac{T_{2s}}{T_1} + b_i(T_{2s} - T_1) + \frac{c_i}{2}(T_{2s}^2 - T_1^2) + \frac{d_i}{3}(T_{2s}^3 - T_1^3) \\ &= \Delta s_i(T_{2s}, T_1) \end{aligned} \tag{3.10}$$

When inserting Eq. (3.10) in Eq. (3.9), it can be observed that the value of T_{2s} is the only unknown in Eq. (3.9), and it can be found by using the bisection iterative method [100].

Finally, once the value of T_{2s} is found, Eqs. (3.7) and (3.8) can be used to calculate w_{GT}. However, the real final temperature T_2 is needed for other calculations in the cycle. The bisection iterative method is used once again to find T_2 knowing that

$$w_{GT} = h_1 - h_2 = \sum_i mf_i \Delta h_i (T_1, T_2) \tag{3.11}$$

where w_{GT} and T_1 have known values, mass fractions can be calculated, and T_2 is the only unknown. Eqs. (3.7) and (3.9) are taken from Chapters 9 and 12 of [7].

3.5.2. *Condenser*

To calculate the state at the condenser outlet (state {3} for IBC/D), the formation of liquid water must be taken into account. The heat transferred to the coolant is expressed by:

$$q = \varepsilon_{CO} q_{\max} \tag{3.12}$$

where ε_{CO} is the condenser effectiveness, and $q_{\max}$, the maximum heat transfer rate that could be exchanged in the condenser. $q_{\max}$ is determined by the limiting fluid in the heat exchanger. In the context of the paper, the limiting side is the gas stream since the coolant can be chosen and its mass flow rate ratio can be as high as desired. With the hypothetical state {3'} where the mixture reaches the minimum theoretical temperature T_A, the maximum potential heat transfer rate is:

$$q_{\max} = h_2 - h_{3'} = \sum_i mf_i \left(h_{2,i} - h_{3',i} \right) \tag{3.13}$$

Eq. (3.8) is used for CO_2, N_2, and H_2O_{vap}, while Ar has a constant c_p and the liquid water enthalpy can be found in thermodynamic tables or specialized software (Section 3.4.6). Due to the fact that the mass fractions change in the process, the enthalpy of formation (at $T_{ref} = 298$ K) of liquid and vapor water need to be used:

$$
\begin{aligned}
q_{\max} = \sum_{i=CO_2,N_2} & mf_i \Delta h_i \left(T_2, T_A\right) + mf_{Ar} c_p (T_2 - T_A) \\
& + mf_{in,vap} \left(h^\circ_{f,vap} + \Delta h_{vap}(T_2, T_{ref})\right) \\
& - mf_{out,vap} \left(h^\circ_{f,vap} + \Delta h_{vap}(T_A, T_{ref})\right) \\
& - mf_{out,liq} \left(h^\circ_{f,liq} + h(T_A, P_2) - h(T_{ref}, P_{atm})\right)
\end{aligned}
\tag{3.14}
$$

Water mass fractions at condenser input and output are calculated with Eqs. (3.3) to (3.6), where the vapor pressure P_{vap} has to be greater than the saturation pressure P_{sat} so that the water may condense. The exhaust stream temperature at the condenser output T_3 is found with the iterative bisection method by equating the real heat transfer rate q with $\varepsilon_{CO} q_{\max}$. In this process, $q_{\max}$, ε_{CO}, T_2, T_{ref}, $h^\circ_{f,vap}$, $h^\circ_{f,liq}$, P_2 and P_{atm} have known values, mass fractions can be calculated, and T_3 is the only unknown. Eq. (3.12) is taken from Chapter 11 of [40] and Eq. (3.13) from Chapter 13 of [7].

3.5.3. *Compressor*

The compressor model is similar to that of the gas turbine, but the process is reversed. The equations shown in this section assume that the inlet is at state $\{3\}$ and the outlet at state $\{4\}$. It follows that:

$$
w_{CP} = h_4 - h_3 = (h_{4s} - h_3) / \eta_{CP} \tag{3.15}
$$

For all the IBC variants that include liquid water drainage, there is no liquid water at the inlet, as well as the outlet because of the increasing temperature. Then Eq. (3.16) is used to find T_{4s} with the iterative bisection method, where $s^\circ_4 - s^\circ_3$ is found with Eq. (3.10), and $h_{4s} - h_3$ is calculated with Eq. (3.8).

$$
R \ln\left(P_4 / P_3\right) = s^\circ_4 - s^\circ_3 \tag{3.16}
$$

Regarding the basic IBC, liquid water may be present in the compressor. The entropy of formation of water must then be used in the developed form of Eq. (3.16):

$$
\begin{aligned}
R\ln\left(P_4/P_3\right) = \sum_{i=CO_2,N_2} & mf_i \Delta s_i\left(T_{4s},T_3\right) + mf_{Ar}c_{p,Ar}\ln(T_{4s}/T_3) \\
& + mf_{out,vap}\left(s^{\circ}_{f,vap} + \Delta s_{vap}(T_{4s},T_{ref})\right) \\
& - mf_{in,vap}\left(s^{\circ}_{f,vap} + \Delta s_{vap}(T_3,T_{ref})\right) \\
& + mf_{out,liq}\left(s^{\circ}_{f,liq} + s(T_{4s},P_{atm}) - s(T_{ref},P_{atm})\right) \\
& - mf_{in,liq}\left(s^{\circ}_{f,liq} + s(T_3,P_2) - s(T_{ref},P_{atm})\right)
\end{aligned} \tag{3.17}
$$

where T_{4s} is the only unknown and all mass fractions can be calculated. Similarly, $h_{4s}-h_3$ is computed using the enthalpy of formation of water. Eqs. (3.15) and (3.16) are taken from Chapters 9 and 12 of [7].

3.5.4. *Steam turbine*

The steam turbine is the main equipment of the open Rankine cycle found in the IBC/D/S and IBC/D/S/R. A schematic representation of the water evolution in the steam turbine between states {9} and {10} is provided in Fig. 3.6. This T – s diagram shows that the water is superheated vapor for the higher pressures, and reaches a saturated mixture state for lower pressures. The superheated state requires the use of the turbine dry efficiency η_{dry} [2] for calculating the intermediary thermodynamic states (open squares in Fig. 3.6). However, the saturated mixture requires the use of the Baumann efficiency η_B [2] [30] to consider the decrease of the turbine efficiency due to the presence of liquid droplets (black squares in Fig. 3.6). Therefore, a method based on differential thermodynamic evolution (see [101] for more details) is used to model the evolution from state {9} to state {10}. Each turbine stage deals with a small part of the total pressure drop, allowing the calculation of the vapor quality at each stage to determine the appropriate efficiency expression to use.

When the water is superheated, the enthalpy h_j at the outlet of the turbine stage j can be expressed as:

$$
h_j = h_{j-1} - \eta_{dry}(h_{j-1} - h_{j,s}) \tag{3.18}
$$

When the water is a saturated mixture, the enthalpy h_j at the outlet of stage j uses the Baumann expression as follows:

$$h_j = \frac{h_{j-1} - A\left(x_j - h_{j,f} \big/ \left(h_{j,g} - h_{j,f}\right)\right)}{1 + A \big/ \left(h_{j,g} - h_{j,f}\right)}$$
$$A = \frac{\eta_{dry}}{2}\left(h_{j-1} - h_{j,s}\right) \tag{3.19}$$

Finally, the steam turbine specific work is expressed by using the enthalpy of the last pressure stage, corresponding to the enthalpy at state {10}:

$$w_{ST} = h_9 - h_{10} \tag{3.20}$$

Eqs. (3.18)-(3.20) are taken from Chapter 5 of [2].

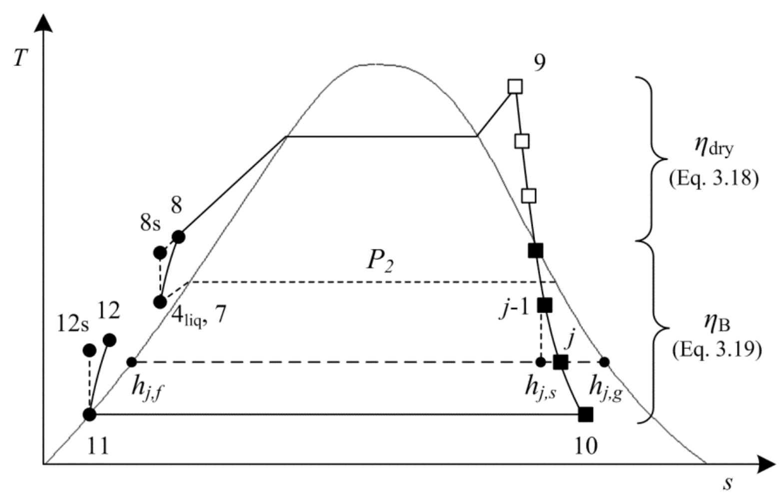

Figure 3.6. Calculation principle of steam turbine intermediate stages on thermodynamic diagram.

3.5.5. *Heat exchangers*

Aside from the condenser (CO) that is present in all cycles, there are four other possible heat exchangers: the refrigeration cycle evaporator (EV/R) and condenser (CO/R), and the open Rankine cycle evaporator (EV/S) and condenser (CO/S). They are all counterflow, but temperature calculations for these pieces of equipment are different. Both condensers use the coolant on the cold side, for which the mass flow rate is unknown. Thus, a temperature difference ΔT_{CO} between the hot side outlet (refrigerant or water) and T_A is assumed. However for the CO/S, ΔT_{CO} allocates the minimum condensing temperature of the water exiting the steam turbine, the minimum vapor quality ultimately deciding the outlet temperature (see constraints in Eqs. (3.26) and (3.30)). Furthermore, the EV/S is divided in three parts for calculation purposes (economizer, evaporator and superheater), see page 43 in [102]. The economizer and evaporator are constrained by a maximum effectiveness $\varepsilon_{\max}$, while the water state at the outlet of the superheater (SH) is determined using $\varepsilon_{\max}$. The limiting side being always the water, the enthalpy at the steam turbine inlet (state {9}) may be calculated as follow:

$$\begin{aligned} q_{SH} &= h_9 - h_{g@P_9} = \varepsilon_{\max} q_{\max} \\ q_{\max} &= h_{9'} - h_{g@P_9} \\ h_9 &= h_{g@P_9} + \varepsilon_{\max}\left(h_{9'} - h_{g@P_9}\right) \end{aligned} \tag{3.21}$$

where $h_{g@P_9}$ is the enthalpy of the saturated vapor at pressure P_9 and $h_{9'}$ is the superheated vapor enthalpy if it could reach T_2, (equivalent to an effectiveness of 100%, see Fig. 3.7a). As an additional verification, the pinch point temperature difference (ΔT_{pp}) located at the economizer output must be higher than a tolerance value ΔT_{tol}. Finally, the same value ΔT_{tol} (see Fig. 3.7b) is imposed in the EV/R between the refrigerant input and exhaust gases output since this is what is limiting the heat exchange. The method used in Eq. (3.21) is taken from Chapter 11 of [40].

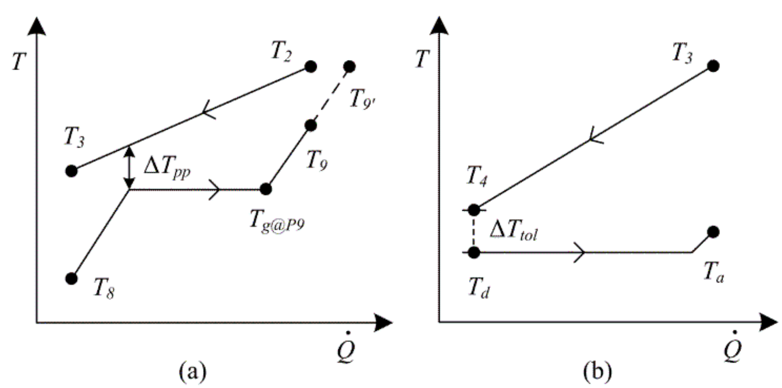

Figure 3.7. Temperature evolution in evaporators. (a) EV/S. (b) EV/R.

3.5.6. *Conditions and assumptions*

The main assumptions considered in this work can be summarized as:

- The models assume steady-state.
- Exhaust gases are considered as a mixture of ideal gases.
- Exhaust gases at system inlet are at atmospheric pressure.
- Turbines, compressors and pumps performances are defined by isentropic efficiencies.
- Steam turbine uses both dry and Baumann efficiencies.
- Liquid water formation is considered in all calculations.
- No pressure losses or heat losses are considered.

Fixed parameters are listed in Table 3.1. Turbomachinery efficiencies have been selected based on typical values used in recent literature. For example, a gas turbine efficiency of 0.795 has been reported in [80] and compressor efficiency of 0.78 in [103] in a Brayton cycle. Bianchi and De Pascale [92] used turbomachinery efficiency of 0.8 for the IBC. Steam turbine and pump isentropic efficiencies of 0.75 and 0.85 were chosen in [83] for a Rankine steam bottom cycle. Vaja et al. [104] states that turbines in ORC have efficiency ranging between 0.8 and 0.88, and uses a pump efficiency of 0.8.

Table 3.1. Values of the fixed parameters in this study

Parameter	Values
Exhaust gases inlet pressure P_1	101.325 kPa
Gas turbine efficiency η_{GT}	0.8
Compressors efficiency η_{CP}	0.75
Pumps efficiency η_{PP}	0.75
Steam turbine dry efficiency η_{ST}	0.75
Minimum tolerated vapor quality x_{tol}	0.9
Condenser (CO) effectiveness ε_{CO}	0.85
Maximum heat exchanger effectiveness $\varepsilon_{\max}$	0.85
Minimum temperature difference ΔT_{tol}	5 K
Temperature difference CO/S and CO/R ΔT_{CO}	10 K
Range of exhaust gases temperature T_1	600 – 1200 K
Range of coolant temperature T_A	280 – 340 K

3.6. Optimization

To properly compare the performance of the different thermodynamic cycles, their operation parameters must be optimized. The objective function used in the present study is the specific work output w, which represents the amount of energy (kJ) produced for each kg of exhaust gases. Other commonly used objective functions include the net power generated, thermal efficiency, exergy destruction and second-law efficiency. Using the specific work as an objective function provides a convenient “reusability” of the results for different exhaust gases mass flow rate. Objective function evaluation, design variables and constraints definition for the five cycles are provided in Sections 3.6.1 to 3.6.4. Three optimization algorithms commonly used for thermodynamic cycles have been tested before making the choice: the function *fmincon.m* with the "interior-point" algorithm, the genetic algorithm function *ga.m*, both from the Optimization Toolbox™ of MATLAB, and an in-house Particle Swarm Optimization (PSO) function. The first algorithm (*fmincon.m*) needed starting points very close to the optimum in order to converge towards it, making the optimization problematic. The second one (*ga.m*) provided better results, but often gave local maxima due to its tendency to converge rapidly. The third one (PSO) was the only one capable of finding near-optimum solutions within three attempts, thus it was selected for this work.

Originally developed by Kennedy [73], the PSO algorithm has been implemented in MATLAB with the help of Yarpiz tutorials [74] for the basic principles and Clarke et al. [105] to consider constraints. The PSO control parameters used in this work are: (i) stop criterion: relative error of 10^{-5} between iterations j and $j-2$; (ii) maximum number of iterations: 30; (iii) swarm size: $35 \cdot n_{dv}$, where n_{dv} is the number of design variables; (iv) inertia coefficient: 1; (v) damping coefficient: 0.7; (vi) personal acceleration coefficient: 1; (vii) social acceleration coefficient 1.25. Three optimization runs were done systematically for each set of exhaust temperature T_1 and coolant temperature T_A, and in the end, the one with the highest maximized specific work was retained.

It is worth to mention that the optimization problems that are described below are relatively "heavy". For optimizing the most complex cycle, ~45 minutes of computational time is required for a single value of T_A and T_1. Since the optimization was repeated for a large number of combinations of T_A and T_1 (in fact 1891 scenarios for each cycle, i.e. 31 T_A values × 61 T_1 values), the computational time required was over 175 days for optimizing all the cycles that were tested. The complexity comes from to the iterative processes in the calculation of the objective function and the presence of many local maxima.

3.6.1. *IBC and IBC/D optimization*

The design variable involved in the optimization of the IBC or the IBC/D is the gas turbine outlet pressure P_2 (see Fig. 3.1). However, the evaluation of the objective function is different for the IBC (Eq. (3.22)), and the IBC/D (Eq. (3.23)):

IBC: $$w = w_{GT} - w_{CP} \tag{3.22}$$

IBC/D: $$w = w_{GT} - (1 - mf_{H_2O,liq}) w_{CP} - mf_{H_2O,liq} w_{PP} \tag{3.23}$$

Nonetheless, the optimization statement of both cycles can be summarized as:

$$\begin{array}{c} \text{IBC} \\ \textit{and} \\ \text{IBC/D} \end{array} \begin{cases} \text{maximize}\left(w\right) \\ \text{optimizing}\left(P_2\right) \\ \text{respecting}\left(T_3 - T_A \geq \Delta T_{tol}\right) \\ \text{fixed values: see Table 3.1} \end{cases} \tag{3.24}$$

There is only one constraint ensuring the physical validity of the evaluated design: the temperature difference in the condenser (CO) between the gas stream outlet and the coolant inlet must be greater than a minimum value ($\Delta T_{tol} = 5\ \text{K}$). The fixed parameters considered in the paper and the bounds of all the design variables are collected in Table 3.1 and Table 3.2, respectively.

Table 3.2 Bounds of the different design variables

Design variable	Inferior limit	Superior limit
Gas turbine outlet pressure P_2	10 kPa	101.325 kPa
Steam turbine inlet pressure P_9	50 kPa	22 000 kPa
Refrigeration utilization rate U_R	0	1

3.6.2. *IBC/D/S optimization*

The IBC/D/S has two design variables: the gas turbine outlet pressure P_2 and the steam turbine inlet pressure P_9 (see Fig. 3.3). Its specific work output (the objective function) is expressed by

$$w = w_{GT} - (1 - mf_{H_2O,liq}) w_{CP} + mf_{H_2O,liq} (w_{ST} - w_{PP1} - w_{PP2}) \tag{3.25}$$

while the optimization problem is formulated by

$$\text{IBC/D/S} \begin{cases} \text{maximize}(w) \\ \text{optimizing}(P_2, P_9) \\ \text{respecting} \begin{cases} T_4 - T_A \geq \Delta T_{tol}, & x_{\min} \geq x_{tol} \\ \Delta T_{pp} \geq \Delta T_{tol}, & \varepsilon_{EC} \leq \varepsilon_{\max} \\ h_9 \geq h_{g@P_9}, & \varepsilon_{EV} \leq \varepsilon_{\max} \end{cases} \\ \text{fixed values: see Table 3.1} \end{cases} \tag{3.26}$$

There are six constraints limiting the design optimization. The first is the same as in Section 3.6.1. The five other constraints concern the open Rankine cycle. First, the pinch point temperature difference ΔT_{pp} must be greater than ΔT_{tol}, and the water at state {9} has to be superheated ($h_9 \geq h_{g@P_9}$). Next, each stage of the steam turbine calculated with the methodology presented in Section 3.5.4 must have a vapor quality greater than a tolerance quality ($x_{tol} = 0.9$) to avoid excess blade wear [7]. Finally, since the efficiencies of the economizer and evaporator are not fixed but determined by post-treatment, they must not exceed a maximum value ($\varepsilon_{\max} = 0.85$).

3.6.3. *IBC/D/R optimization*

The IBC/D/R also has two design variables: the gas turbine outlet pressure P_2 and the refrigeration utilization rate U_R. The latter is such that when T_4 (see Fig. 3.4) is equal to T_3, then $U_R = 0$, and when T_4 is equal to 273.2 K, then $U_R = 1$. The objective function is expressed as

$$w = w_{GT} - (1 - mf_{H_2O,liq})w_{CP} - mf_{H_2O,liq}(w_{PP}) - w_{CP/R} \tag{3.27}$$

and the optimization statement is summarized by

$$\text{IBC/D/R} \begin{cases} \text{maximize}(w) \\ \text{optimizing}(P_2, U_R) \\ \text{respecting} \begin{cases} T_3 - T_A \geq \Delta T_{tol} \\ P_a \leq P_b \end{cases} \\ \text{fixed values: see Table 3.1} \end{cases} \tag{3.28}$$

The first constraint is the one presented in Section 3.6.1. The second constraint ensures that the compressor (CP/R) inlet pressure P_a is lower than its outlet pressure P_b. The limit is $P_a = P_b$, where the refrigeration cycle is not used.

3.6.4. *IBC/D/S/R optimization*

The most complex optimization is for the IBC/D/S/R. Its optimization involves three design variables: the gas turbine outlet pressure P_2, the steam turbine inlet pressure P_9 (see Fig. 3.5) and the refrigeration utilization rate U_R. The specific work output of the IBC/D/R/S is calculated with

$$w = w_{GT} - (1 - mf_{H_2O,liq})w_{CP} + mf_{H_2O,liq}(w_{ST} - w_{PP1} - w_{PP2}) - w_{CP/R} \tag{3.29}$$

and the optimization problem is presented as

$$
\text{IBC/D/S/R}\begin{cases}\text{maximize}\left(w\right)\\ \text{optimizing}\left(P_2,P_9,U_R\right)\\ \text{respecting}\begin{cases}T_4-T_A\geq\Delta T_{tol}, & \varepsilon_{EC}\leq\varepsilon_{\max}\\ \Delta T_{pp}\geq\Delta T_{tol}, & \varepsilon_{EV}\leq\varepsilon_{\max}\\ h_9\geq h_{g@P_9}, & P_a\leq P_b\\ x_{\min}\geq x_{tol}, & \end{cases}\\ \text{fixed values: see Table 3.1}\end{cases} \tag{3.30}
$$

Constraints limiting the optimal design combine the ones for the IBC/D/S and the ones for the IBC/D/R.

3.7. Results

All results of this study are presented here: Section 3.7.1 shows the effect of the outlet gas turbine variable P_2 on the IBC and IBC/D; Section 3.7.2 contains the optimization results of the five systems; Section 3.7.3 compares the best performing variant of the IBC with the Rankine cycle and ORCs; Section 3.7.4 proposes a sensitivity analysis of turbomachinery efficiencies; and Section 3.7.5 investigates the liquid water addition in the IBC/D/S/R.

3.7.1. *Parametric analysis of the IBC and IBC/D*

In order to illustrate the optimization opportunity of IBC, Fig. 3.8 presents a parametric analysis of the specific work w with respect to the design variable P_2 for the IBC and IBC/D systems at a given operating condition (i.e., $T_1 = 800\ \text{K}$ and $T_A = 290\ \text{K}$). The dotted lines in the curves between 16 and 20 kPa indicate the non-respect of the sole condition constraining both cycles (see Eq. (3.24)) for the given pressure P_2. For lower pressures, there is no condensed water, so the specific work output w does not vary between cycles. First, Fig. 3.8 shows that an optimum exists for both cycles. It can be noted that $w_{\max}$ of IBC/D is located at a higher value of P_2 than $w_{\max}$ of IBC (36.5 vs. 28.0 kPa) for this case. This is due to the amount of condensed water increasing with P_2, thus increasing the drainage before the compressor. However, w starts decreasing after $P_{2,\text{opt}}$ because the reduced flow rate in the compressor does not make up for the decreased power produced in the gas turbine. Finally, the negative specific work arising from pressure lower than 16 kPa is justified by the equipment being non-isentropic, i.e., less power is produced by the gas turbine while more power is required by the compressor, resulting in the possibility of a negative net specific work.

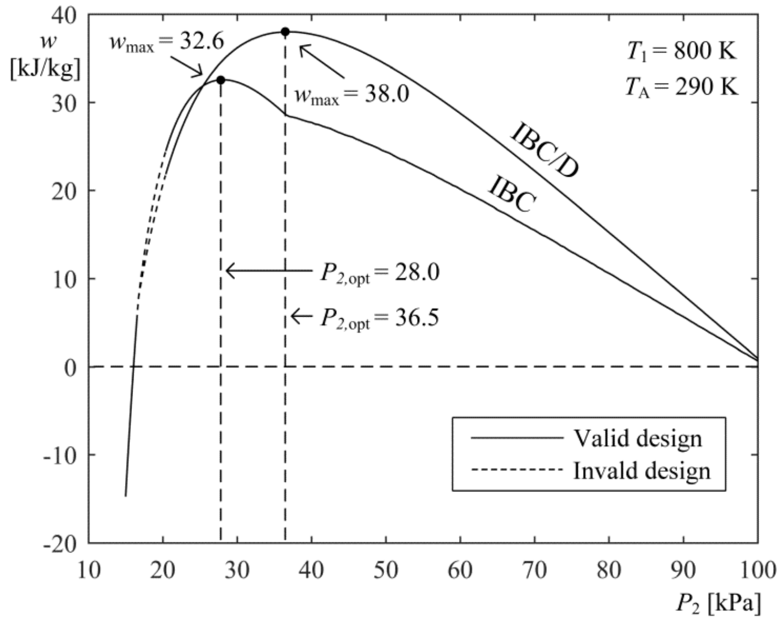

Figure 3.8. Parametric analysis of IBC and IBC/D for a specific case.

3.7.2. *Complete optimization results*

The optimization methodology described in Section 3.6 was used to generate the charts presented in Figure 3.9 and Figure 3.10. More specifically, the maximized specific work output w_{max} for each cycle is shown in Figure 3.9 and the corresponding optimized design variables are displayed in Figure 3.10. The cases considered in this section are exhaust gases temperature T_1 from 600 to 1200 K with 10 K increment and coolant temperature T_A from 280 to 340 K with 2 K increment. Hence, a total of 1891 optimization runs were performed for each cycle, and each datapoint in the charts is the output of an individual optimization for a couple of T_1 (y-axis) and T_A (x-axis) values.

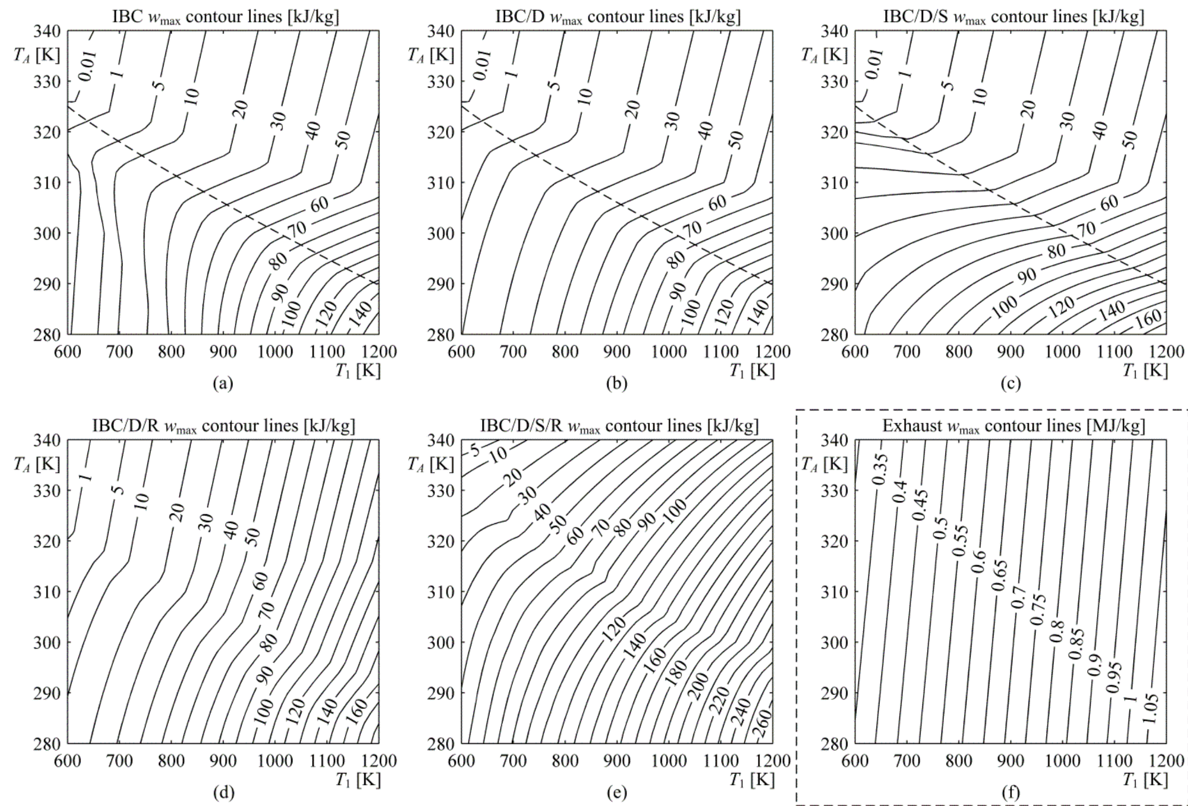

Figure 3.9. Maximized specific work output for each cycle. (a) IBC. (b) IBC/D. (c) IBC/D/S. (d) IBC/D/R. (e) IBC/D/S/R.

Figure 3.9 shows several behaviors of the cycles depending on both temperatures. First, the dotted line in the graphs of the (a) IBC, (b) IBC/D, and (c) IBC/D/S divides the area where there is liquid water drainage (below) and where there is none (above). Indeed, the lower T_1 and T_A, the more condensate there is after the condenser. Notice that there is a section right below the dotted line where w_{max} of IBC and IBC/D is comparable. The liquid water drainage is particularly small there, making no noticeable difference between both cycle performances. However, the combined effect of the removed condensate and the supplementary power produced in the steam turbine can be observed in Figure 3.9c. The contour lines are more 'horizontal' than in the other cycles which means that w_{max} is more strongly dependant on T_A (which determines the condensate mass) than on T_1.

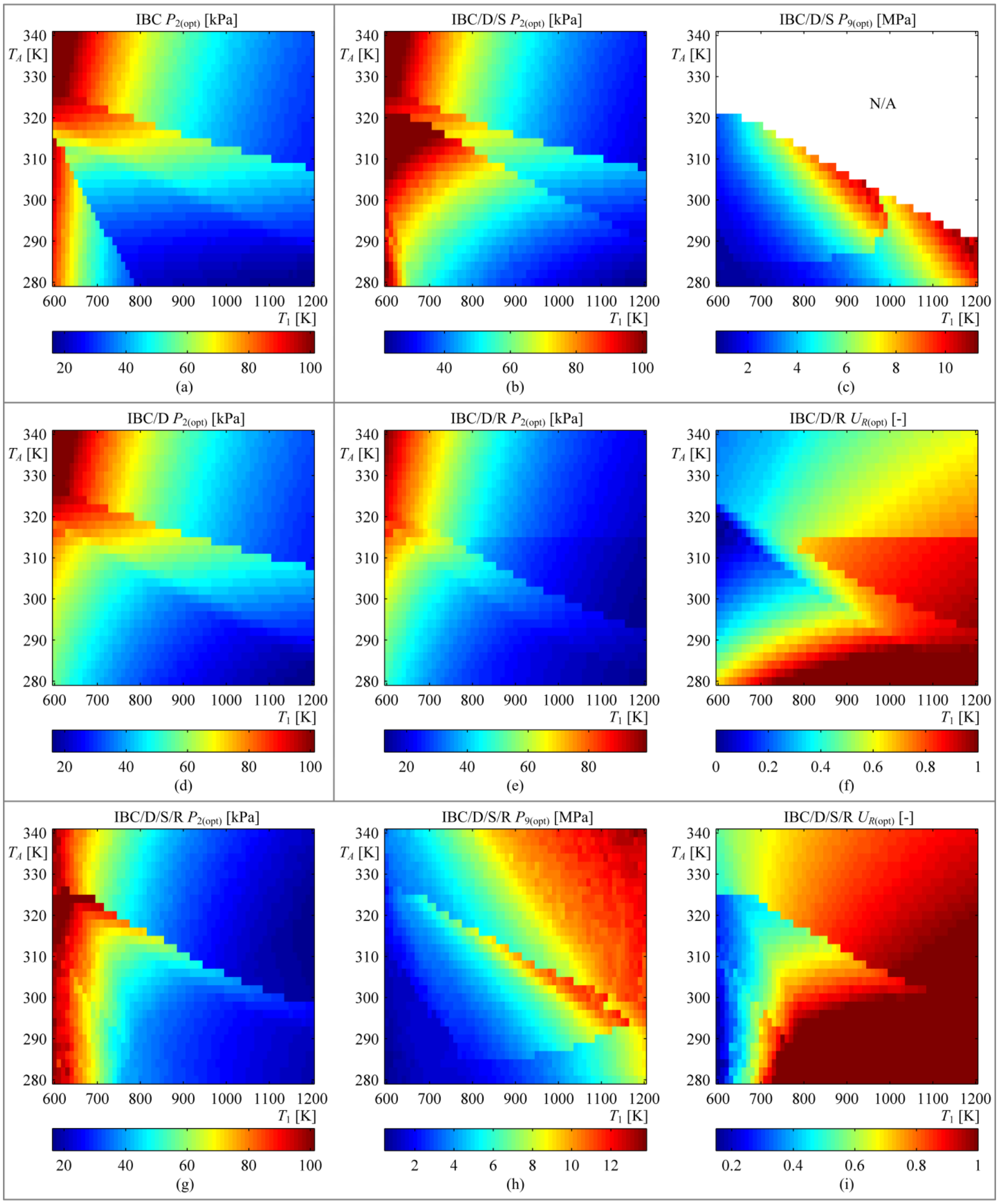

Figure 3.10. Optimized design variables for each cycle. (a) IBC $P_{2(\mathrm{opt})}$. (b) IBC/D/S $P_{2(\mathrm{opt})}$. (c) IBC/D/S $P_{9(\mathrm{opt})}$. (d) IBC/D $P_{2(\mathrm{opt})}$. (e) IBC/D/R $\mathrm{P}_{2(\mathrm{opt})}$. (f) IBC/D/R $U_{R(\mathrm{opt})}$. (g) IBC/D/S/R $P_{2(\mathrm{opt})}$. (h) IBC/D/S/R $P_{9(\mathrm{opt})}$. (i) IBC/D/S/R $U_{R(\mathrm{opt})}$.

Furthermore, it should be observed that the value of $w_{\max}$ for the IBC/D is not always higher than that of the IBC when there is possible condensate drainage. For example,

$w_{max} = 159.6$ kJ/kg for IBC and $w_{max} = 155.6$ kJ/kg for IBC/D at $T_1 = 1200$ K and $T_A = 280$ K. As a rule of thumb, for value of T_1 above 970 K, keeping liquid water in the compressor leads to a better performance. These results are in line with recent literature [106] [107] indicating that the use of water sprays in the compressor proves to decrease its power consumption for certain cases.

Next, it can be observed in Figure 3.9 that the addition of the refrigeration cycle is beneficial for all operating temperatures. The IBC/D/R (Figure 3.9d) does not make a significant difference compared to the IBC/D below the dotted line, but it allows doubling the specific work above the dotted line, where there was originally no condensation. Regarding the IBC/D/S/R, Figure 3.9e shows that the combination of an open Rankine cycle with a refrigeration cycle makes it the most performant cycle of the five presented here, for the whole range of operating temperatures.

Finally, Figure 3.9f shows the specific energy content of the exhaust in kJ per kg of exhaust as a function of T_A and T_1. This figure is presented in order to convert the specific work output from Figure 3.9a to Figure 3.9e into thermal efficiency (based on a heat "consumption" between T_1 and T_A), which is another metrics that is often used to assess the performance of cycles such as IBC. To determine the thermal efficiency of a cycle, its specific work output should be divided by the specific energy content of the exhaust from Figure 3.9f. For example, it is found that the thermal efficiency of the IBC/D/S/R varies from 1% (for low hot source temperature and high cold source temperature, i.e. upper left corner of the figure) to 25% (for high hot source temperature and low cold source temperature, i.e. lower right corner of the figure).

3.7.3. *Comparison with Rankine cycle and Organic Rankine Cycle*

In Section 3.7.2, the IBC/D/S/R was identified as the best performing cycle of the five presented in this work for the operating conditions investigated. In order to compare its potential to other more 'classical' cycles, the subcritical Rankine cycle (with water) and the subcritical ORC with isobutane ($T_1 < 540\ \mathrm{K}$) and benzene ($T_1 > 540\ \mathrm{K}$) have also been simulated and optimized.

The Rankine cycle is the basic steam cycle for power generation, often used as a bottoming cycle for the Brayton Cycle. The ORC is a Rankine cycle using an organic fluid instead of water as working fluid, usually more suitable for heat sources with lower temperatures. Their most simple version consists of a steam turbine to produce work, a condenser to return the fluid to saturated liquid, a pump to reach the evaporating pressure, and a heater (heat exchanger in the context of a WHR system) to obtain the desired thermodynamic state at the turbine inlet. This work employs the same calculation methods found in Section 3.5.5 for all heat exchangers (economizer, evaporator, superheater and condenser) and in Section 3.5.4 for the steam turbine.

Results of the present model have been compared with those of two other studies for specific operation points to validate the Rankine cycles model. In the first study, Larsen et al. (2014) [108] compared optimized design performance for Rankine cycle and ORC with R245ca, among others. They used a model to predict the performance of a marine low speed two-stroke engine. The selected conditions are ambient air temperature of 25°C (298 K) and exhaust gases temperature of 234°C (507 K), where the engine loaded at 85% leads to an exhaust mass flow of 46.2 kg/s. Although benzene is the working fluid used here for an exhaust temperature of 507 K, maximized specific work with R245ca has been calculated for comparison purposes. R245ca was not considered here due to its maximum temperature of applicability of 450 K. Table 3.3 shows that results are fairly similar. Sources of discrepancy include, inter alia, higher component efficiency and higher minimum approaches used in Larsen et al. (2014). In the second comparison, a saturated ORC performance using isobutane is taken from Bianchi and De Pascale (2011) [92]. Since their specific work is based on the working fluid flow rate, the efficiency based on the available exhaust heat is used instead (Fig. 12). With exhaust temperature of 150°C (423 K) and ambient air temperature of 15°C (288 K), one finds an efficiency of 0.62. Comparing to the results of the present model, which calculated 0.65, the relative difference is found to be

4.8%. Based on these comparisons, the present Rankine cycle models were thus found to be adequate.

Table 3.3. Specific work comparison with Larsen et al. (2014) for Rankine cycles

Working fluid	Water	R245ca
Net power (Larsen) [kW]	863	1160
Specific work (Larsen) [kJ/kg]	18.68	25.11
Specific work, present model [kJ/kg]	17.45	26.82
Relative difference [%]	6.6	6.8

The operating conditions investigated in this section are an exhaust temperature T_1 from 400 to 1000 K for the Rankine cycle, from 400 to 700 K for the ORC, and a coolant temperature range T_A from 280 to 340 K. The different range for T_1 (400 to 1000 K) has been selected in order to focus on conditions for which the IBC/D/S/R is better than the ORC or the Rankine cycle. Figure 3.11 shows the ratio between w_{max} for the IBC/D/S/R and that for (a) the ORC w_{max}, and (b) the Rankine cycle w_{max}.

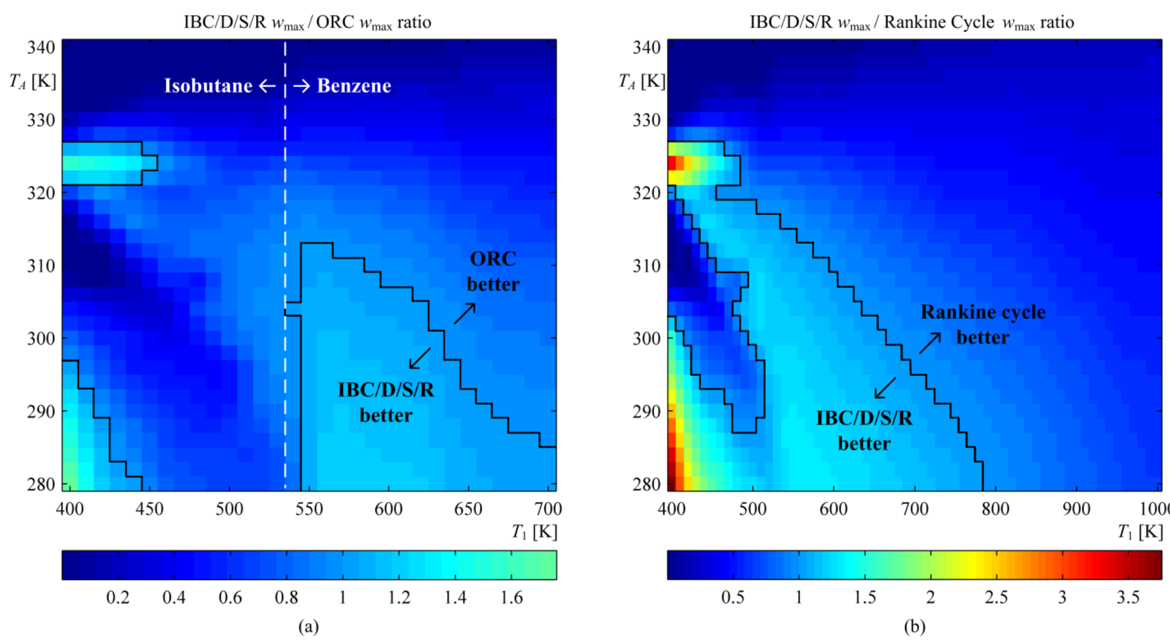

Figure 3.11. Ratio of the cycles' maximized specific work. (a) Between the IBC/D/S/R and two ORCs. (b) Between IBC/D/S/R and the Rankine cycle.

In Fig. 3.11a, it can be observed that the IBC/D/S/R offers a better performance than the ORC with benzene in the specific area, i.e., for T_1 values between 550 and 700 K, and T_A values between 280 and 310 K. Moreover, there are two other identified areas where the IBC/D/S/R is better (for lower T_1 values). In Fig. 3.11b, the area where the IBC/D/S/R is better than the Rankine cycle is also revealed, i.e., for T_1 values between 400 and 800 K, and T_A values between 280 and 330 K.

3.7.4. *Sensitivity analysis with respect to efficiency of turbomachinery*

In the precedent sections, the efficiency values of turbomachinery components were fixed to the values in Table 3.1. However, the overall cycle performance can be affected by these values [109], and therefore a sensitivity analysis is proposed in this section. One specific test case was chosen for this purpose. The cycles were optimized as previously described, but with different values of efficiencies. Figure 3.12 shows the maximized specific work output as a function of the efficiency of (a) compressor(s), (b) gas turbine, and (c) steam turbine when applicable for $T_1 = 800\ \mathrm{K}$ and $T_A = 310\ \mathrm{K}$. For each graph, the efficiency of the piece of equipment is varied between 0.5 and 0.9 while all other parameters remain fixed.

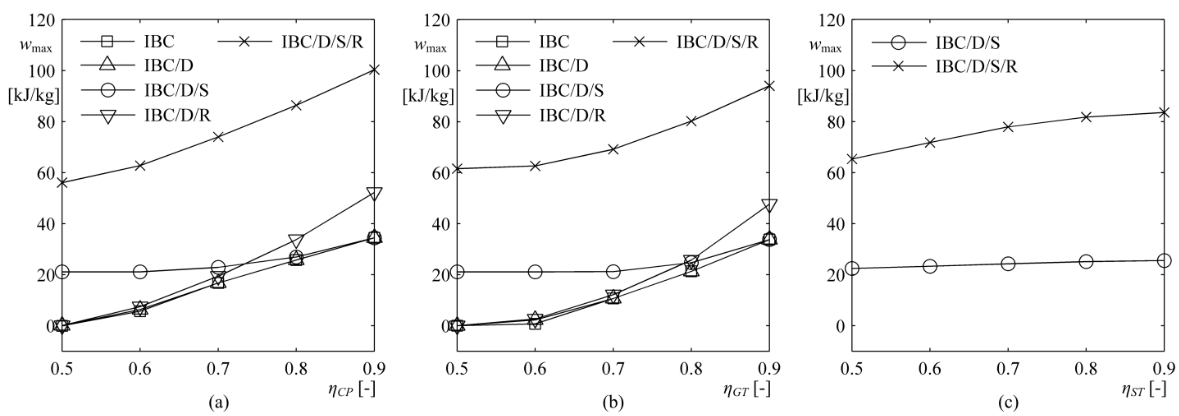

Figure 3.12. Maximized specific work output at T_1 = 800 K & T_A = 310 K with respect to the (a) Compressor(s) efficiency. (b) Gas turbine efficiency. (c) Steam turbine efficiency.

Figures 3.12a and 3.12b show that IBC/D/S is the least affected when the compressor and gas turbine efficiency decreases, since it can rely more and more on the steam turbine to produce work with an increased gas turbine outlet pressure P_2. IBC and IBC/D are affected similarly by a change of compressor and/or gas turbine efficiency. Also, as these efficiency values are decreased, the performance of IBC/D/R eventually becomes equivalent to that of IBC and IBC/D up to a point where not work can be produced when the compressor or the gas turbine efficiency value reaches 0.5. IBC/D/S/R is also affected by the efficiency values, but continues to yield a significant work output even at low efficiency values.

The relatively low impact of the steam turbine efficiency on the performance seen in Fig. 3.12c may be explained by the optimized pressures and the different path taken by the steam. With a low efficiency, the preferred design is a slightly higher P_2 to obtain hotter steam and a much higher steam turbine inlet pressure P_8. Referring to the water T-s diagram, the steam entropy increases more at each turbine stage, traveling further to the right and stays superheated at a lower pressure. The vapor quality constraint ($x_{\min} \geq 0.9$) is then respected everywhere in the turbine and the steam exits at the pressure imposed by the condenser, the greater pressure drop compensating for the poor efficiency.

3.7.5. *Parametric analysis of liquid water addition in the IBC/D/S/R*

The separated liquid water mass is a limiting factor for the work generation in the IBCs with a steam turbine. If there is additional water available in certain applications, for example an engine in a boat, it would then be possible to mix this supplied water with the one that has been separated from the exhaust stream. Then, in this section, the supplied water mass per kg of exhaust gases becomes a new design variable, noted as m_{sw}. Figure 3.13a presents the IBC/D/S/R+ system, the symbol + meaning that supplied water is present.

For each value of m_{sw}, this IBC/D/S/R+ system was optimized with respect to the remaining design variables (P_2, P_9, U_R). The result for each m_{sw} value are presented in Fig. 3.13b, for two distinct cases (i.e., Case #1: $T_1 = 800$ K, $T_A = 290$ K, and Case #2: $T_1 = 1100$ K, $T_A = 320$ K).

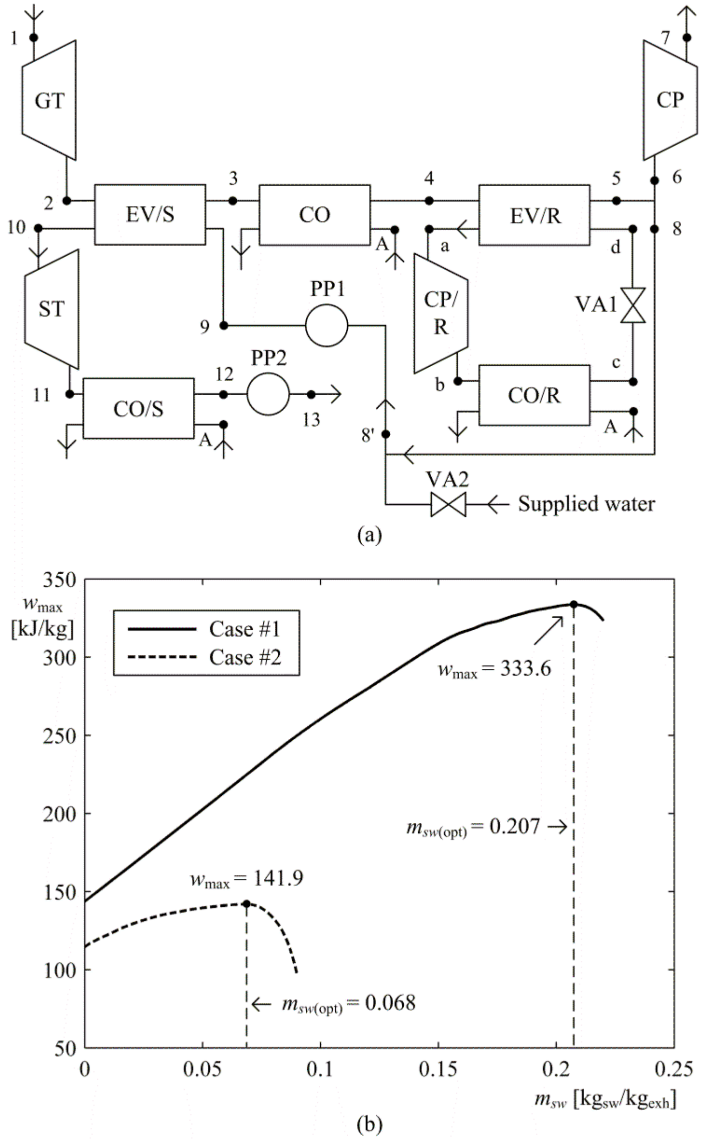

Figure 3.13. Evolution of the IBC/D/R/S+ w_{max} with respect to the supplied water mass m_{sw} for case #1 (T_1 = 800 K & T_A = 290 K) and case #2 (T_1 = 1100 K & T_A = 320 K)

Regarding case #1, it is possible to increase the specific work by a maximum of 23.8% compared to the case without supplied water (i.e., IBC/D/S/R). The maximum is reached at $m_{sw(\mathrm{opt})} = 0.068$, and above this value, w_{max} decreases and becomes even lower than the IBC/D/S/R work. Regarding case #2, it is possible to increase the specific work by a maximum of 132% compared to the IBC/D/S/R. The maximum is reached at $m_{sw(\mathrm{opt})} = 0.207$. For both cases, it was observed that the optimal value of P_2 is almost equal to P_1, which means that there is almost no work performed by the gas thermodynamic cycle. In other words, the system becomes the equivalent of a Rankine cycle only.

3.8. Example of applications

Two concrete scenarios are presented to show how to use the results of this paper. In the first scenario, a diesel engine in a truck rejects exhaust gases with a mean temperature of 800 K and the coolant is the ambient air at 300 K. If there was an IBC system connected to the engine, a supplementary work could be produced, depending on the variant used. The basic IBC would supply a maximum specific work of 30 kJ/kg (see Figure 3.9a); the IBC/D, 31 kJ/kg (Figure 3.9b); the IBC/D/S, 53 kJ/kg (Figure 3.9c); the IBC/D/R, 38 kJ/kg (Figure 3.9d); and the IBC/D/S/R, 100 kJ/kg (Figure 3.9e). The best cycle to select would then depend on an economic trade-off between the cost to the different pieces of equipment and the value of the additional work produced by the selected waste heat recovery cycle. The associated operating parameters of the best cycle (IBC/D/S/R) are $P_{2(\mathrm{opt})} = 45$ kPa (see Fig. 3.10g), $P_{9(\mathrm{opt})} = 3.6$ MPa (Fig. 3.10h), and $U_{R(\mathrm{opt})} = 0.84$ (Fig. 3.10i). However, Fig. 3.11b shows that the Rankine cycle is a better choice for that scenario, where the optimal IBC/D/S/R yields to less than 70% of the optimal Rankine cycle performance.

In the second scenario, a reciprocating diesel engine in a container carrier rejects exhaust gases with a mean temperature of 600 K and the coolant is the sea water at its surface mean temperature, 290 K [110]. The basic IBC would supply a maximum specific work of less than 1 kJ/kg (see Figure 3.9a); the IBC/D, 8 kJ/kg (Figure 3.9b); the IBC/D/S, 49 kJ/kg (Figure 3.9c); the IBC/D/R, 10 kJ/kg (Figure 3.9d); and the IBC/D/S/R, 51 kJ/kg (Figure 3.9e). The refrigeration cycle having only a weak impact on the performance for this scenario, the IBC/D/S would likely be a better choice than the IBC/D/S/R. However, this 4% improvement might be enough to justify the supplementary equipment, especially in a container carrier where the weight is less of a constraint than on land. The associated operating parameters of the IBC/D/S are $P_{2(\mathrm{opt})} = 90$ kPa (see Fig. 3.10b) and $P_{9(\mathrm{opt})} \approx 1$ MPa (Fig. 3.10c). Both cycles have a better performance than an ORC with benzene: by 15% for the IBC/D/S/R and by 11% for the IBC/D/S (see Fig. 3.11a).

To get an estimate of what these numbers represent in terms of the nominal engine work, a theoretical diesel cycle is considered. For the truck example, a compression ratio of 18 leads to an engine specific work of 970 kJ/kg. Thus, the IBC/D/S/R would be able to recover heat corresponding to about 10 % of the engine power. For the container carrier example, a compression ratio of 14 leads to an engine specific work of 560 kJ/kg. The IBC/D/S then would provide about 9 % additional power. These percentages correspond to lower limits of IBC systems performance since exhaust gases are considered at atmospheric pressure when exiting the engine, whereas they can have a higher pressure in practice.

While it would be difficult to incorporate in a cost-effective way a complex system like the IBC/D/S/R in a truck, it could be a more realistic solution in large boats. As stated in Mito et al. (2018) [111], maritime transport has risen over the last decades and CO_2 and NO_x emissions reduction efforts call for fuel consumption reduction. Large ships engines usually have low speed and small compression ratio, resulting in exhaust gases colder than in land transport. Looking at Figure 3.9, IBC/D/S and IBC/D/S/R then would make the best use of low exhaust temperature and ocean water temperature as cold sink. In addition to a higher performance in this range of temperatures, an advantage of IBC/D/S over ORC is the absence of an additional working fluid that can be hazardous and environmentally damaging [108]. Hence, an IBC system with a steam turbine could be a feasible solution to reduce fuel consumption in applications such as large boats. However, at the time of writing, the IBC technology is designed to exploit only the exhaust waste heat, which can be considered as a drawback when compared to other WHR solutions. Engines have other heat sources like scavenger air and jacket water, which the ORC is capable to recover, see the work of Scaccabarozzi et al. [112].

3.9. Conclusion

In this paper, five different Inverted Brayton Cycles are numerically simulated and optimized to various operating conditions (exhaust temperature and coolant temperature). Among these five systems, three are presented for the first time in the literature (i.e., the IBC/D/S, IBC/D/R and IBC/D/S/R). The objective function was the specific work output, and the design variables were the gas turbine outlet pressure (for all cycles), the steam turbine inlet pressure (for IBC/D/S and IBC/D/S/R), and the refrigeration utilization rate (for IBC/D/R and IBC/D/S/R). A PSO script was used to perform the optimization for a range of exhaust temperature from 600 to 1200 K and of coolant temperature from 280 to 340 K.

The optimization results are reported in the form of design charts (Figs. Figure 3.9 to 3.11). For instance, the data presented in Figs. Figure 3.9 and 3.10 allows to perform the predesign of heat recovery systems using the IBC principle. The addition of a refrigeration cycle to the IBC/D turned out beneficial for all operating conditions, especially for exhaust temperature higher than 700 K. Moreover, the data presented in Fig. 3.11 allows to determine for which operating conditions the IBC/D/S/R may be more efficient than a basic ORC or a Rankine cycle. The sensitivity analysis on turbomachinery efficiencies highlighted the impact they have on overall system performance. Finally, the data presented in Fig. 3.13 illustrates the effect of adding supplied liquid water after the separation for two specific cases of operating conditions.

The work presented in this paper could be extended in various ways. An economic analysis of the different IBC cycles would be needed to determine to which extent their specific work output justifies their purchase cost in different contexts, compared with other types of cycles. Multi-objective optimization of the IBC cycles including objective functions such as weight, space or cost could help to identify families of optimal solutions best suited for different applications. The models developed for this study could also be improved. For example, the pressure losses and heat losses could be considered, and the transient behavior of the system that results from the variations of hot and cold source temperatures could also be investigated. Such transient behavior would require mathematical expressions of the performance of each piece of equipment in off-design conditions. Moreover, new cycles using water recirculation could be simulated and optimized. For example, water exiting the steam turbine of the IBC/D/S or IBC/D/R/S could be reinjected in the exhaust gases upstream of the gas turbine, which can potentially increase the specific work output of the cycle.

3.10. Appendix A

Tables 3.4, 3.5 and 3.6 describe the thermodynamic states in each new cycle proposal for a common case of optimized design at $T_1 = 900$ K and $T_A = 300$ K. The reference state to calculate enthalpy and entropy for the exhaust gases is at $T_{ref} = 298$ K and $P_{ref} = P_{atm}$. Notice that state {4} of IBC/D/S and IBC/D/R, and state {5} of IBC/D/S/R are not included in tables: liquid water and "dry" exhaust gases have each their own state after the separation.

Table 3.4. Thermodynamic states of the exhaust gases and separated water in the optimized IBC/D/S system for a specific case.

State	Composition	$\dot{m}/\dot{m}_1$ [%]	T [K]	P [kPa]	h [kJ/kg]	s [kJ/kg·K]
1	Exhaust	100	900.00	101.325	695.515	1.25946
2	Exhaust	100	801.53	54.2602	544.314	1.29776
3	Exhaust	100	754.20	54.2602	517.376	1.22425
5	Exhaust	98.2	310.59	54.2602	13.2834	0.22428
6	Exhaust	98.2	386.07	101.325	93.8581	0.27580
7	Water	1.79	310.59	54.2602	156.881	0.53881
8	Water	1.79	311.47	8184.82	167.797	0.54691
9	Water	1.79	758.46	8184.82	3360.58	6.66594
10	Water	1.79	324.54	13.2313	2382.66	7.40041
11	Water	1.79	324.54	13.2313	215.166	0.72179
12	Water	1.79	324.55	101.325	215.285	0.72188

Table 3.5. Thermodynamic states of the exhaust gases, separated water and R134a in the optimized IBC/D/R system for a specific case.

Point	Composition	$\dot{m}/\dot{m}_1$ [%]	T [K]	P [kPa]	h [kJ/kg]	s [kJ/kg·K]
1	Exhaust	100	900.00	101.325	695.515	1.25946
2	Exhaust	100	730.69	32.7641	489.218	1.33222

3	Exhaust	100	319.53	32.7641	23.0570	0.40123
5	Exhaust	94.8	291.79	32.7641	-6.35141	0.30499
6	Exhaust	94.8	429.86	101.325	137.384	0.38130
7	Water	5.24	291.79	32.7641	78.2407	0.27698
8	Water	5.24	291.79	101.325	78.3323	0.27706
a	R134a	56.0	289.79	467.355	409.210	1.73054
b	R134a	56.0	319.74	933.396	428.637	1.74583
c	R134a	56.0	310.00	933.396	251.731	1.17569
d	R134a	56.0	286.79	467.355	251.731	1.18148

Table 3.6. Thermodynamic states of the exhaust gases, separated water and R134a in the optimized IBC/D/S/R system for a specific case.

Point	Composition	$\dot{m}/\dot{m}_1$ [%]	T [K]	P [kPa]	h [kJ/kg]	s [kJ/kg·K]
1	Exhaust	100	900.00	101.325	695.515	1.25946
2	Exhaust	100	746.18	36.7553	507.760	1.32409
3	Exhaust	100	525.29	36.7553	250.147	0.91539
4	Exhaust	100	305.00	36.7553	7.41948	0.31789
6	Exhaust	92.1	275.75	36.7553	-23.4923	0.21135
7	Exhaust	92.1	392.65	101.325	95.7856	0.27897
8	Water	7.91	275.75	36.7553	10.9571	0.03979
9	Water	7.91	276.20	5717.26	18.5317	0.04668
10	Water	7.91	710.44	5717.26	3276.11	6.70536
11	Water	7.91	322.95	12.2313	2380.59	7.42694
12	Water	7.91	322.95	12.2313	208.515	0.70125
13	Water	7.91	322.97	101.325	208.652	0.70139
a	R134a	74.6	273.75	268.185	399.850	1.73820
b	R134a	74.6	325.75	933.396	434.990	1.76552
c	R134a	74.6	310.00	933.396	251.731	1.17569
d	R134a	74.6	270.75	268.185	251.731	1.19119

Conclusion

Cette thèse avait pour principal objectif d'offrir un outil aidant les ingénieurs au pré-design des systèmes de récupération de la chaleur produisant un travail spécifique net maximisé. Les deux axes de recherche établis étaient le cycle de Rankine organique (ORC) employé dans une centrale géothermique et le cycle de Brayton inversé (IBC) comme système de récupération de la chaleur perdue dans les gaz d'échappement de moteurs. En plus de la production des diagrammes escomptés, d'intéressantes tendances thermodynamiques ont pu être dégagées de tous les résultats obtenus.

La conclusion débute avec une brève récapitulation des travaux de chaque chapitre accompagnée de la mise en évidence des contributions originales et se termine avec des suggestions pour des travaux futurs.

Chapitre 1

Les cycles thermodynamiques simulés et optimisés dans ce chapitre sont l'ORC de base en régime sous-critique et l'ORC de base en régime transcritique. Les résultats sont présentés en fonction de la température d'entrée du géofluide allant de 80 à 180°C, et de la température de condensation allant de 0.1 à 50°C, tous les deux par incrément de 1°C. Les variables optimisées sont la pression à l'entrée de la turbine, le rapport entre le débit massique du géofluide et celui du fluide de travail, et l'efficacité du surchauffeur. Trente-six (36) fluides organiques ont été testés pour l'ensemble des combinaisons de températures.

Les résultats ont montré que 12 fluides sont optimaux pour une certaine plage de combinaisons de températures, et 20 mènent à au moins 95% du travail spécifique net maximisé. Le régime transcritique est le plus souvent optimal, et 10 des 12 meilleurs fluides sont de type rétrograde. Le travail spécifique net maximisé présente une tendance quadratique par rapport à la différence entre les températures maximale et minimale du cycle (c'est-à-dire la différence entre celle du géofluide et celle de condensation du fluide de travail).

Présenter des résultats d'optimisation sous forme de diagrammes d'une aussi grande finesse est une nouveauté dans la littérature sur les cycles thermodynamiques. De nouveaux éléments de modélisation ont aussi été introduits : le calcul de l'efficacité de la turbine et la vérification de la contrainte du point de pincement dans les échangeurs se sont faits avec une méthode différentielle. De plus, la corrélation développée à partir d'une analyse d'ordre de grandeur permet de prédire le travail spécifique net maximal avec une erreur relative moyenne de 4% par rapport aux résultats numériques.

Chapitre 2

Suivant le même axe que le chapitre 1 sur les ORCs, le chapitre 2 a intégré plusieurs améliorations aux modèles : (i) l'ajout de l'ORC avec deux pressions de chauffage en régime sous-critique et transcritique, (ii) l'ajout de la récupération dans tous les cycles, (iii) l'implémentation d'une tour de refroidissement à voie humide, et (iv) l'ajout d'une contrainte sur la température de réinjection. La température de la source froide était alors définie comme étant la température du thermomètre mouillé (bulbe humide) de l'air ambient, pour une plage de valeurs possibles de 10 à 32°C. Les 20 meilleurs fluides identifiés au chapitre 1 ont été testés pour ces cycles améliorés. En plus de l'ajout de variables de design relatives au chauffage à deux pressions, l'écart de température dans la tour de refroidissement (« range » en anglais) faisait aussi partie des variables de conception.

Les chartes de conception présentent premièrement le travail spécifique net maximisé, les meilleurs fluides, les régimes optimaux et les variables de design optimales pour chacun des modes de chauffage (une et deux pressions). Ensuite, les meilleurs cycles sont identifiés et l'impact de la charge auxiliaire est investiguée pour chacun des quatre cycles. Diverses tendances ont été observées :

- Pour les cycles à une pression de chauffage, les designs employant des fluides rétrogrades sont généralement optimaux avec un régime sous-critique, et ceux employant des fluides normaux le sont avec un régime transcritique.

- Les fluides normaux sont optimaux à haute température du puits de chaleur.
- Pour les cycles à deux pressions de chauffage seulement des fluides rétrogrades sont optimaux.
- L'ORC transcritique à deux pressions est le meilleur sur la plus grande plage de température d'opération.
- L'emploi du chauffage à deux pressions est le plus avantageux à basse température de géofluide et à haute température du puits de chaleur.
- Lorsque la température du géofluide est à moins de 120°C, la charge auxiliaire relative augmente significativement, et les valeurs optimales de l'écart de température dans la tour de refroidissement (« range ») diminuent significativement, tout comme pour les designs de l'ORC à une pression de chauffage avec les fluides normaux.

L'analyse de l'impact du « range » de la tour de refroidissement intégrée à l'optimisation de centrales géothermiques est une nouveauté, tout comme l'optimisation du cycle transcritique à deux pressions de chauffage. Ces résultats placent ce dernier comme une option à prendre sérieusement en considération et montrent l'importance du choix du « range » lorsqu'une tour de refroidissement est employée. De plus, les corrélations servant à prédire le travail spécifique maximisé ont été mises à jour pour les cycles à une pression de chauffage et à deux pressions de chauffage.

Chapitre 3

Ce chapitre portait sur l'axe 2 du projet, soit l'étude des variantes de l'IBC appliquées à la récupération de la chaleur des gaz d'échappement de moteurs. Cinq variantes de l'IBC ont été modélisées et optimisées selon des températures des gaz d'échappement de 600 à 1200 K et du puits de chaleur de 280 à 340 K. Ces variantes sont (i) l'IBC de base, (ii) l'IBC avec drainage de l'eau liquide (IBC/D), (iii) l'IBC/D avec une turbine à vapeur (IBC/D/S), (iv) l'IBC/D avec un cycle de réfrigération (IBC/D/R), et (v) l'IBC/D avec une turbine à vapeur et un cycle de réfrigération (IBC/D/S/R). Les diagrammes des résultats montrant le travail spécifique net maximisé et les variables de design optimales répondent à plusieurs questions :

- L'IBC/D/S/R est le cycle le plus performant sur toute la plage de températures d'opérations.
- La performance de l'IBC/D/S se compare à celle de l'IBC/D/S/R à basse températures des gaz d'échappement et du puits de chaleur.
- Il existe des plages de températures d'opération où l'IBC/D/S/R est supérieur à l'ORC et au cycle de Rankine.
- L'application jugée comme la plus appropriée pour un système IBC est sur le moteur de grands bateaux, tel un paquebot ou un porte-conteneur.

La nouveauté apportée par cette étude se trouve dans la présentation de trois nouveaux cycles thermodynamiques, leur simulation numérique et leur optimisation pour une large plage de températures d'opération. Cette étude peut alors servir de base pour des travaux ultérieurs où les modèles des turbomachines et des échangeurs de chaleurs pourront être complexifiés.

Perspectives futures

Le travail amorcé par cette thèse a permis de dégager plusieurs points pouvant orienter divers travaux futurs. Concernant l'axe 1 (chapitres 1 et 2), d'autres configurations de centrales géothermiques peuvent être investiguées, telle la régénération, ainsi que d'autres systèmes de refroidissement, comme le condenseur à air. Le travail sur la tour de refroidissement peut aussi être continué en considérant une modélisation plus poussée. Ensuite, considérer les mélanges de fluides est un élément de recherche nécessaire : ils ont le potentiel de remplacer des fluides toxiques ou nocifs pour l'environnement en présentant des performances similaires. Une suite logique au travail sur les ORCs en régime permanent est de simuler le régime transitoire, ce qui représenterait bien l'opération des centrales géothermiques. On pourrait alors coupler le modèle de l'ORC avec un modèle de réservoir simulant l'écoulement du géofluide à travers un réseau de fractures. Il serait ainsi possible d'optimiser le design de la centrale pour maximiser l'énergie produite durant l'ensemble de sa durée de vie. Les résultats obtenus serviraient à l'évaluation du potentiel de la géothermie profonde au Québec. Finalement, il serait très intéressant de pouvoir adapter et améliorer les modèles d'ORC en comparant les résultats numériques avec les mesures prises sur un montage expérimental.

En ce qui a trait à l'axe 2 (chapitre 3), la complexification des modèles aura pour conséquence d'augmenter le temps de calcul pour l'optimisation. Il serait donc approprié de se concentrer sur une plage réduite de températures d'opération concernant une seule application à la fois pour développer les variantes de l'IBC. Puisqu'il s'agit de nouveaux systèmes, il serait pertinent d'effectuer une analyse économique afin de déterminer dans quelle mesure leur performance justifie leur coût d'achat. Dans la même veine, une optimisation multi-objectif incluant des fonctions objectifs tels le coût et l'espace occupé aiderait à identifier des familles de solutions optimales convenant le mieux selon l'application. Similairement à l'axe 1, le comportement transitoire pourrait être simulé, de même que le contrôleur du système, et les résultats numériques pourraient être comparés avec des mesures expérimentales. Finalement, de nouveaux systèmes IBC incluant la recirculation de l'eau liquide en amont de la turbine à gaz pourraient être simulés et optimisés afin de vérifier s'ils offrent une performance accrue.

References

[1] M.-A. Richard *et al.*, “Intégration de la géothermie profonde dans le portefeuille énergétique canadien,” IREQ, IREQ-2017-0032, 2016.
[2] R. DiPippo, *Geothermal Power Plants: Principles, Applications, Case Studies and Environmental Impact*, Third. Boston: Butterworth-Heinemann, 2012.
[3] A. Kalina, H. Leibowitz, L. Lazzeri, and F. Diotti, “Recent development in the application of Kalina cycle for geothermal plants,” presented at the Proceedings of the World Geothermal Congress, Florence, Italy, International Geothermal Association, Florence, 1995, pp. 2093–2096.
[4] R. Gicquel, *Energy Systems - A New Approach to Engineering Thermodynamics*. London: Taylor & Francis Group, 2012.
[5] L. Pan and H. Wang, “Improved analysis of Organic Rankine Cycle based on radial flow turbine,” *Appl. Therm. Eng.*, vol. 61, no. 2, pp. 606–615, Nov. 2013, doi: 10.1016/j.applthermaleng.2013.08.019.
[6] S. Carnot, *Réflexions sur la puissance motrice du feu et sur les machines propres à développer cette puissance*. Paris: Chez Bachelier Libraire, 1824.
[7] Y. A. Çengel, M. A. Boles, and M. Lacroix, *Thermodynamique: Une Approche Pragmatique*, Sixth. Montréal: Les Éditions de la Chenelière inc., 2008.
[8] H. D. Madhawa Hettiarachchi, M. Golubovic, W. M. Worek, and Y. Ikegami, “Optimum design criteria for an Organic Rankine cycle using low-temperature geothermal heat sources,” *Energy*, vol. 32, no. 9, pp. 1698–1706, Sep. 2007, doi: 10.1016/j.energy.2007.01.005.
[9] “KCORC,” *kcorc.org*. [Online]. Available: kcorc.org. [Accessed: 16-Apr-2017].
[10] D. Wei, X. Lu, Z. Lu, and J. Gu, “Performance analysis and optimization of organic Rankine cycle (ORC) for waste heat recovery,” *Energy Convers. Manag.*, vol. 48, no. 4, pp. 1113–1119, Apr. 2007, doi: 10.1016/j.enconman.2006.10.020.
[11] Y. Dai, J. Wang, and L. Gao, “Parametric optimization and comparative study of organic Rankine cycle (ORC) for low grade waste heat recovery,” *Energy Convers. Manag.*, vol. 50, no. 3, pp. 576–582, Mar. 2009, doi: 10.1016/j.enconman.2008.10.018.
[12] A. Toffolo, A. Lazzaretto, G. Manente, and M. Paci, “A multi-criteria approach for the optimal selection of working fluid and design parameters in Organic Rankine Cycle systems,” *Appl. Energy*, vol. 121, pp. 219–232, May 2014, doi: 10.1016/j.apenergy.2014.01.089.
[13] A. Franco, “Power production from a moderate temperature geothermal resource with regenerative Organic Rankine Cycles,” *Energy Sustain. Dev.*, vol. 15, no. 4, pp. 411–419, Dec. 2011, doi: 10.1016/j.esd.2011.06.002.
[14] G. Cammarata, L. Cammarata, and G. Petrone, “Thermodynamic Analysis of ORC for Energy Production from Geothermal Resources,” *Energy Procedia*, vol. 45, pp. 1337–1343, 2014, doi: 10.1016/j.egypro.2014.01.140.
[15] D. Fiaschi, A. Lifshitz, G. Manfrida, and D. Tempesti, “An innovative ORC power plant layout for heat and power generation from medium- to low-temperature geothermal resources,” *Energy Convers. Manag.*, vol. 88, pp. 883–893, Dec. 2014, doi: 10.1016/j.enconman.2014.08.058.
[16] H. D. Madhawa Hettiarachchi, M. Golubovic, W. M. Worek, and Y. Ikegami, “Optimum design criteria for an Organic Rankine cycle using low-temperature geothermal heat sources,” *Energy*, vol. 32, no. 9, pp. 1698–1706, Sep. 2007, doi: 10.1016/j.energy.2007.01.005.
[17] M. Astolfi, M. C. Romano, P. Bombarda, and E. Macchi, “Binary ORC (organic Rankine cycles) power plants for the exploitation of medium–low temperature geothermal sources – Part A: Thermodynamic optimization,” *Energy*, vol. 66, pp. 423–434, Mar. 2014, doi: 10.1016/j.energy.2013.11.056.
[18] X. Wang, X. Liu, and C. Zhang, “Parametric optimization and range analysis of Organic Rankine Cycle for binary-cycle geothermal plant,” *Energy Convers. Manag.*, vol. 80, pp. 256–265, Apr. 2014, doi: 10.1016/j.enconman.2014.01.026.

[19] T.-C. Hung, "Waste heat recovery of organic Rankine cycle using dry fluids," *Energy Convers. Manag.*, vol. 42, no. 5, pp. 539–553, Mar. 2001, doi: 10.1016/S0196-8904(00)00081-9.
[20] U. Drescher and D. Brüggemann, "Fluid selection for the Organic Rankine Cycle (ORC) in biomass power and heat plants," *Appl. Therm. Eng.*, vol. 27, no. 1, pp. 223–228, Jan. 2007, doi: 10.1016/j.applthermaleng.2006.04.024.
[21] Z. Gu and H. Sato, "Performance of supercritical cycles for geothermal binary design," *Energy Convers. Manag.*, vol. 43, no. 7, pp. 961–971, May 2002, doi: 10.1016/S0196-8904(01)00082-6.
[22] Y.-J. Baik, M. Kim, K.-C. Chang, Y.-S. Lee, and H.-K. Yoon, "A comparative study of power optimization in low-temperature geothermal heat source driven R125 transcritical cycle and HFC organic Rankine cycles," *Renew. Energy*, vol. 54, pp. 78–84, Jun. 2013, doi: 10.1016/j.renene.2012.08.055.
[23] Z. Shengjun, W. Huaixin, and G. Tao, "Performance comparison and parametric optimization of subcritical Organic Rankine Cycle (ORC) and transcritical power cycle system for low-temperature geothermal power generation," *Appl. Energy*, vol. 88, no. 8, pp. 2740–2754, Aug. 2011, doi: 10.1016/j.apenergy.2011.02.034.
[24] H. Chen, D. Y. Goswami, and E. K. Stefanakos, "A review of thermodynamic cycles and working fluids for the conversion of low-grade heat," *Renew. Sustain. Energy Rev.*, vol. 14, no. 9, pp. 3059–3067, Dec. 2010, doi: 10.1016/j.rser.2010.07.006.
[25] S. J. Zarrouk and H. Moon, "Efficiency of geothermal power plants: A worldwide review," *Geothermics*, vol. 51, pp. 142–153, Jul. 2014, doi: 10.1016/j.geothermics.2013.11.001.
[26] J. Clarke and J. T. McLeskey Jr., "Multi-objective particle swarm optimization of binary geothermal power plants," *Appl. Energy*, vol. 138, pp. 302–314, Jan. 2015, doi: 10.1016/j.apenergy.2014.10.072.
[27] S.-Y. Zhao and Q. Chen, "Design criteria of different heat exchangers for the optimal thermodynamic performance of regenerative refrigeration systems," *Appl. Therm. Eng.*, vol. 93, pp. 1164–1174, Jan. 2016, doi: 10.1016/j.applthermaleng.2015.10.031.
[28] S. Jalilinasrabady, R. Itoi, P. Valdimarsson, G. Saevarsdottir, and H. Fujii, "Flash cycle optimization of Sabalan geothermal power plant employing exergy concept," *Geothermics*, vol. 43, pp. 75–82, Jul. 2012, doi: 10.1016/j.geothermics.2012.02.003.
[29] N. A. Pambudi, R. Itoi, S. Jalilinasrabady, and K. Jaelani, "Exergy analysis and optimization of Dieng single-flash geothermal power plant," *Energy Convers. Manag.*, vol. 78, pp. 405–411, Feb. 2014, doi: 10.1016/j.enconman.2013.10.073.
[30] K. Baumann, "Some Recent Developements in Large Steam Turbine Practice," *J. Inst. Electr. Eng.*, vol. 59, pp. 565–623, 1921.
[31] SoftInWay Switzerland LLC, "Heat Balance Design and Analysis Online Tool – AxCYCLE."
[32] Ian H. Bell and the CoolProp Team, "CoolProp," Copyright -2015 2010.
[33] M. Holmgren, "X Steam, Thermodynamic properties of water and steam," 2007.
[34] National Institute of Standards and Technology (NIST), "Transport properties database (REFPROP v9.0)."
[35] MATLAB, "The Mathworks Inc.," 2014.
[36] J. Clarke, L. McLay, and J. T. McLeskey Jr., "Comparison of genetic algorithm to particle swarm for constrained simulation-based optimization of a geothermal power plant," *Adv. Eng. Inform.*, vol. 28, no. 1, pp. 81–90, Jan. 2014, doi: 10.1016/j.aei.2013.12.003.
[37] Matlab Optimization Toolbox, "The Mathworks Inc.," 2014.
[38] MathWorks, "Choosing a Solver - MATLAB & Simulink," 2015.
[39] J.-A. R. Sarr and F. Mathieu-Potvin, "Improvement of Double-Flash geothermal power plant design: A comparison of six interstage heating processes," *Geothermics*, vol. 54, pp. 82–95, Mar. 2015, doi: 10.1016/j.geothermics.2014.12.002.
[40] T. L. Bergman, A. S. Lavine, F. P. Incropera, and D. P. Dewitt, *Fundamentals of heat and mass transfer*, Seventh. Hoboken: John Wiley & Sons, Inc., 2011.
[41] AccuWeather, "Riverside Month Weather - AccuWeather Forecast for CA 92506," 2015.

[42] AccuWeather, “Fermont Month Weather - AccuWeather Forrecast for Quebec Canada,” 2015.
[43] S. Van Erdeweghe, J. Van Bael, B. Laenen, and W. D’haeseleer, “Design and off-design optimization procedure for low-temperature geothermal organic Rankine cycles,” *Appl. Energy*, vol. 242, pp. 716–731, May 2019, doi: 10.1016/j.apenergy.2019.03.142.
[44] S. Lecompte, H. Huisseune, M. van den Broek, B. Vanslambrouck, and M. De Paepe, “Review of organic Rankine cycle (ORC) architectures for waste heat recovery,” *Renew. Sustain. Energy Rev.*, vol. 47, pp. 448–461, Jul. 2015, doi: 10.1016/j.rser.2015.03.089.
[45] N. Chagnon-Lessard, F. Mathieu-Potvin, and L. Gosselin, “Geothermal power plants with maximized specific power output: Optimal working fluid and operating conditions of subcritical and transcritical Organic Rankine Cycles,” *Geothermics*, vol. 64, pp. 111–124, Nov. 2016, doi: 10.1016/j.geothermics.2016.04.002.
[46] B.-S. Park, M. Usman, M. Imran, and A. Pesyridis, “Review of Organic Rankine Cycle experimental data trends,” *Energy Convers. Manag.*, vol. 173, pp. 679–691, Oct. 2018, doi: 10.1016/j.enconman.2018.07.097.
[47] A. Uusitalo, J. Honkatukia, T. Turunen-Saaresti, and A. Grönman, “Thermodynamic evaluation on the effect of working fluid type and fluids critical properties on design and performance of Organic Rankine Cycles,” *J. Clean. Prod.*, vol. 188, pp. 253–263, Jul. 2018, doi: 10.1016/j.jclepro.2018.03.228.
[48] A. Landelle, N. Tauveron, R. Revellin, P. Haberschill, and S. Colasson, “Experimental Investigation of a Transcritical Organic Rankine Cycle with Scroll Expander for Low—Temperature Waste Heat Recovery,” *Energy Procedia*, vol. 129, pp. 810–817, Sep. 2017, doi: 10.1016/j.egypro.2017.09.142.
[49] F. Meng, E. Wang, B. Zhang, F. Zhang, and C. Zhao, “Thermo-economic analysis of transcritical CO2 power cycle and comparison with Kalina cycle and ORC for a low-temperature heat source,” *Energy Convers. Manag.*, vol. 195, pp. 1295–1308, Sep. 2019, doi: 10.1016/j.enconman.2019.05.091.
[50] M.-H. Yang, R.-H. Yeh, and T.-C. Hung, “Thermo-economic analysis of the transcritical organic Rankine cycle using R1234yf/R32 mixtures as the working fluids for lower-grade waste heat recovery,” *Energy*, vol. 140, pp. 818–836, Dec. 2017, doi: 10.1016/j.energy.2017.08.059.
[51] L.-H. Zhi, P. Hu, L.-X. Chen, and G. Zhao, “Multiple parametric analysis, optimization and efficiency prediction of transcritical organic Rankine cycle using trans-1,3,3,3-tetrafluoropropene (R1234ze(E)) for low grade waste heat recovery,” *Energy Convers. Manag.*, vol. 180, pp. 44–59, Jan. 2019, doi: 10.1016/j.enconman.2018.10.086.
[52] K. Kurtulus, A. Coskun, S. Ameen, C. Yilmaz, and A. Bolatturk, “Thermoeconomic analysis of a CO2 compression system using waste heat into the regenerative organic Rankine cycle,” *Energy Convers. Manag.*, vol. 168, pp. 588–598, Jul. 2018, doi: 10.1016/j.enconman.2018.05.037.
[53] P. J. Mago, L. M. Chamra, K. Srinivasan, and C. Somayaji, “An examination of regenerative organic Rankine cycles using dry fluids,” *Appl. Therm. Eng.*, vol. 28, no. 8, pp. 998–1007, Jun. 2008, doi: 10.1016/j.applthermaleng.2007.06.025.
[54] R.-J. Xu and Y.-L. He, “A vapor injector-based novel regenerative organic Rankine cycle,” *Appl. Therm. Eng.*, vol. 31, no. 6, pp. 1238–1243, May 2011, doi: 10.1016/j.applthermaleng.2010.12.026.
[55] K. Braimakis and S. Karellas, “Energetic optimization of regenerative Organic Rankine Cycle (ORC) configurations,” *Energy Convers. Manag.*, vol. 159, pp. 353–370, Mar. 2018, doi: 10.1016/j.enconman.2017.12.093.
[56] Z. Ge *et al.*, “Main parameters optimization of regenerative organic Rankine cycle driven by low-temperature flue gas waste heat,” *Energy*, vol. 93, pp. 1886–1895, Dec. 2015, doi: 10.1016/j.energy.2015.10.051.
[57] A. Javanshir, N. Sarunac, and Z. Razzaghpanah, “Thermodynamic analysis of a regenerative organic Rankine cycle using dry fluids,” *Appl. Therm. Eng.*, vol. 123, pp. 852–864, Aug. 2017, doi: 10.1016/j.applthermaleng.2017.05.158.

[58] O. A. Oyewunmi, S. Lecompte, M. De Paepe, and C. N. Markides, “Thermoeconomic analysis of recuperative sub- and transcritical organic Rankine cycle systems,” *Energy Procedia*, vol. 129, pp. 58–65, Sep. 2017, doi: 10.1016/j.egypro.2017.09.187.
[59] J. Li, Z. Ge, Y. Duan, Z. Yang, and Q. Liu, “Parametric optimization and thermodynamic performance comparison of single-pressure and dual-pressure evaporation organic Rankine cycles,” *Appl. Energy*, vol. 217, pp. 409–421, May 2018, doi: 10.1016/j.apenergy.2018.02.096.
[60] G. Manente, A. Lazzaretto, and E. Bonamico, “Design guidelines for the choice between single and dual pressure layouts in organic Rankine cycle (ORC) systems,” *Energy*, vol. 123, pp. 413–431, Mar. 2017, doi: 10.1016/j.energy.2017.01.151.
[61] M. Wang, Y. Chen, Q. Liu, and Z. Yuanyuan, “Thermodynamic and thermo-economic analysis of dual-pressure and single pressure evaporation organic Rankine cycles,” *Energy Convers. Manag.*, vol. 177, pp. 718–736, Dec. 2018, doi: 10.1016/j.enconman.2018.10.017.
[62] J. Li, Z. Ge, Q. Liu, Y. Duan, and Z. Yang, “Thermo-economic performance analyses and comparison of two turbine layouts for organic Rankine cycles with dual-pressure evaporation,” *Energy Convers. Manag.*, vol. 164, pp. 603–614, May 2018, doi: 10.1016/j.enconman.2018.03.029.
[63] J. Li, Z. Ge, Y. Duan, and Z. Yang, “Design and performance analyses for a novel organic Rankine cycle with supercritical-subcritical heat absorption process coupling,” *Appl. Energy*, vol. 235, pp. 1400–1414, Feb. 2019, doi: 10.1016/j.apenergy.2018.11.062.
[64] E. Macchi and M. Astolfi, *Organic Rankine Cycle (ORC) Power Systems: Technologies and Applications*, First edition. Woodhead Publishing, 2016.
[65] Z. Guzović, P. Rašković, and Z. Blatarić, “The comparision of a basic and a dual-pressure ORC (Organic Rankine Cycle): Geothermal Power Plant Velika Ciglena case study,” *Energy*, vol. 76, pp. 175–186, Nov. 2014, doi: 10.1016/j.energy.2014.06.005.
[66] A. Jakobsen, B. D. Rasmussen, and S. E. Andersen, “CoolPack – Simulation tools for refrigeration systems,” *Scan Ref*, vol. 28, no. 4, pp. 7–10, 1999.
[67] Weather and Climate, “Average monthly humidity in Bjelovar (Bjelovar-Bilogora County), Croatia,” *Weather and Climate*, 2019. [Online]. Available: https://weather-and-climate.com/. [Accessed: 19-Jul-2019].
[68] J. G. Andreasen, A. Meroni, and F. Haglind, “A Comparison of Organic and Steam Rankine Cycle Power Systems for Waste Heat Recovery on Large Ships,” *Energies*, vol. 10, no. 4, p. 547, Apr. 2017, doi: 10.3390/en10040547.
[69] R. Yadav, *Steam and Gas Turbines and Power Plant Engineering*, Seventh. Allahabad: Central Publishing House, 2000.
[70] A. Rivera Diaz, E. Kaya, and S. J. Zarrouk, “Reinjection in geothermal fields − A worldwide review update,” *Renew. Sustain. Energy Rev.*, vol. 53, pp. 105–162, Jan. 2016, doi: 10.1016/j.rser.2015.07.151.
[71] B. Buecker, “Cooling Tower Heat Transfer Fundamentals,” *Power Engineering*, 2017. [Online]. Available: https://www.power-eng.com/articles/print/volume-121/issue-7/features/cooling-tower-heat-transfer-fundamentals.html. [Accessed: 25-Oct-2018].
[72] “Certification Annual Report,” Cooling Technology Institute, 2018.
[73] J. Kennedy and R. Eberhart, “Particle swarm optimization,” in , *IEEE International Conference on Neural Networks, 1995. Proceedings*, 1995, vol. 4, pp. 1942–1948 vol.4, doi: 10.1109/ICNN.1995.488968.
[74] Yarpiz, “Video Tutorial of PSO implementation in MATLAB,” *Yarpiz*, 23-May-2016. [Online]. Available: http://yarpiz.com/440/ytea101-particle-swarm-optimization-pso-in-matlab-video-tutorial. [Accessed: 11-Jul-2018].
[75] G. Myhre *et al.*, “Climate Change 2013: The Physical Science Basis. Contribution of Working Group I to the Fifth Assessment Report of the Intergovernmental Panel on Climate Change.,” Cambridge University Press, Cambridge, 2013.
[76] C. J. Noriega Sanchez, L. Gosselin, and A. K. da Silva, “Designed binary mixtures for subcritical organic Rankine cycles based on multiobjective optimization,” *Energy Convers. Manag.*, vol. 156, pp. 585–596, Jan. 2018, doi: 10.1016/j.enconman.2017.11.050.

[77] J. G. DeFlon, “Cooling towers,” US3333835A, 01-Aug-1967.
[78] K. K. McKelvey and M. Brooke, *The Industrial Cooling Tower*. Londres: Elsevier Publishing Company, 1959.
[79] Z. Chen, C. Copeland, B. Ceen, S. Jones, and A. A. Goya, “Modeling and Simulation of an Inverted Brayton Cycle as an Exhaust-Gas Heat-Recovery System,” *J. Eng. Gas Turbines Power-Trans. Asme*, vol. 139, no. 8, p. 081701, Aug. 2017, doi: 10.1115/1.4035738.
[80] A. Uusitalo, A. Ameli, and T. Turunen-Saaresti, “Thermodynamic and turbomachinery design analysis of supercritical Brayton cycles for exhaust gas heat recovery,” *Energy*, vol. 167, pp. 60–79, Jan. 2019, doi: 10.1016/j.energy.2018.10.181.
[81] D. F. Webster, “Turbocharger system for internal combustion engine,” US3557549A, 26-Jan-1971.
[82] T. Durand, P. D. Eggenschwiler, Y. Tang, Y. Liao, and D. Landmann, “Potential of energy recuperation in the exhaust gas of state of the art light duty vehicles with thermoelectric elements,” *Fuel*, vol. 224, pp. 271–279, Jul. 2018, doi: 10.1016/j.fuel.2018.03.078.
[83] J. P. Liu, J. Q. Fu, C. Q. Ren, L. J. Wang, Z. X. Xu, and B. L. Deng, “Comparison and analysis of engine exhaust gas energy recovery potential through various bottom cycles,” *Appl. Therm. Eng.*, vol. 50, no. 1, pp. 1219–1234, Jan. 2013, doi: 10.1016/j.applthermaleng.2012.05.031.
[84] A. T. Hoang, “Waste heat recovery from diesel engines based on Organic Rankine Cycle,” *Appl. Energy*, vol. 231, pp. 138–166, Dec. 2018, doi: 10.1016/j.apenergy.2018.09.022.
[85] D. G. Wilson, “Design of high-efficiency turbomachinery and gas turbines,” Jan. 1983.
[86] M. Bianchi, G. N. di Montenegro, A. Peretto, and P. R. Spina, “A feasibility study of inverted brayton cycle for gas turbine repowering,” *J. Eng. Gas Turbines Power-Trans. Asme*, vol. 127, no. 3, pp. 599–605, Jul. 2005, doi: 10.1115/1.1765121.
[87] N. Iki, H. Furutani, and S. Takahashi, *Potential of a reheat gas turbine system using inverted Brayton cycle*. New York: Amer Soc Mechanical Engineers, 2005.
[88] M. Bianchi, G. N. di Montenegro, and A. Peretto, “Inverted Brayton cycle employment for low-temperature cogenerative applications,” *J. Eng. Gas Turbines Power-Trans. Asme*, vol. 124, no. 3, pp. 561–565, Jul. 2002, doi: 10.1115/1.1447237.
[89] M. Henke, T. Monz, and M. Aigner, “Inverted Brayton Cycle With Exhaust Gas Recirculation-A Numerical Investigation,” *J. Eng. Gas Turbines Power-Trans. Asme*, vol. 135, no. 9, p. 091203, Sep. 2013, doi: 10.1115/1.4024954.
[90] M. M. Bailey, “Comparative Evaluation of Three Alternative Power Cycles for Waste Heat Recovery From the Exhaust of Adiabatic Diesel Engines,” NASA Lewis Reasearch Center, Cleveland, OH, United States, Technical Report No. NASA-TM-86953, 1985.
[91] S. Fujii, K. Kaneko, K. Otani, and Y. Tsujikawa, “Mirror gas turbines: A newly proposed method of exhaust heat recovery,” *J. Eng. Gas Turbines Power-Trans. Asme*, vol. 123, no. 3, pp. 481–486, Jul. 2001, doi: 10.1115/1.1366324.
[92] M. Bianchi and A. De Pascale, “Bottoming cycles for electric energy generation: Parametric investigation of available and innovative solutions for the exploitation of low and medium temperature heat sources,” *Appl. Energy*, vol. 88, no. 5, pp. 1500–1509, May 2011, doi: 10.1016/j.apenergy.2010.11.013.
[93] C. D. Copeland and Z. Chen, “The Benefits of an Inverted Brayton Bottoming Cycle as an Alternative to Turbocompounding,” *J. Eng. Gas Turbines Power-Trans. Asme*, vol. 138, no. 7, p. 071701, Jul. 2016, doi: 10.1115/1.4031790.
[94] I. Kennedy, Z. Chen, B. Ceen, S. Jones, and C. D. Copeland, *Inverted Brayton Cycle with Exhaust Gas Condensation*. New York: Amer Soc Mechanical Engineers, 2017.
[95] A. Buck, “New Equations for Computing Vapor-Pressure and Enhancement Factor,” *J. Appl. Meteorol.*, vol. 20, no. 12, pp. 1527–1532, 1981, doi: 10.1175/1520-0450(1981)020<1527:NEFCVP>2.0.CO;2.
[96] C. Zilio, J. S. Brown, G. Schiochet, and A. Cavallini, “The refrigerant R1234yf in air conditioning systems,” *Energy*, vol. 36, no. 10, pp. 6110–6120, Oct. 2011, doi: 10.1016/j.energy.2011.08.002.

[97] I. H. Bell, J. Wronski, S. Quoilin, and V. Lemort, “Pure and Pseudo-pure Fluid Thermophysical Property Evaluation and the Open-Source Thermophysical Property Library CoolProp,” *Ind. Eng. Chem. Res.*, vol. 53, no. 6, pp. 2498–2508, Feb. 2014, doi: 10.1021/ie4033999.
[98] “Welcome to CoolProp — CoolProp 6.1.0 documentation.” [Online]. Available: http://www.coolprop.org/. [Accessed: 08-Oct-2018].
[99] L. J. Gillespie, “The Gibbs-Dalton Law of Partial Pressures,” *Phys. Rev.*, vol. 36, no. 1, pp. 121–131, Jul. 1930, doi: 10.1103/PhysRev.36.121.
[100] G. B. Arfken, *Mathematical Methods for Physicists*, Third. Orlando: Academic Press, Inc., 1985.
[101] N. Chagnon-Lessard, F. Mathieu-Potvin, and L. Gosselin, “Geothermal power plants with maximized specific power output: Optimal working fluid and operating conditions of subcritical and transcritical Organic Rankine Cycles,” *Geothermics*, vol. 64, pp. 111–124, Nov. 2016, doi: 10.1016/j.geothermics.2016.04.002.
[102] P. K. Nag, *Power Plant Engineering*, Third. New Delhi: Tata McGraw Hill Education Private Limited, 2008.
[103] W. B. Nader, C. Mansour, C. Dumand, and M. Nemer, “Brayton cycles as waste heat recovery systems on series hybrid electric vehicles,” *Energy Convers. Manag.*, vol. 168, pp. 200–214, Jul. 2018, doi: 10.1016/j.enconman.2018.05.004.
[104] I. Vaja and A. Gambarotta, “Internal Combustion Engine (ICE) bottoming with Organic Rankine Cycles (ORCs),” *Energy*, vol. 35, no. 2, pp. 1084–1093, Feb. 2010, doi: 10.1016/j.energy.2009.06.001.
[105] J. Clarke, L. McLay, and J. T. McLeskey, “Comparison of genetic algorithm to particle swarm for constrained simulation-based optimization of a geothermal power plant,” *Adv. Eng. Inform.*, vol. 28, no. 1, pp. 81–90, Jan. 2014, doi: 10.1016/j.aei.2013.12.003.
[106] J. GuanWei, C. MaoLin, X. WeiQing, and S. Yan, “Energy conversion characteristics of reciprocating piston quasi-isothermal compression systems using water sprays,” *Sci. China-Technol. Sci.*, vol. 61, no. 2, pp. 285–298, Feb. 2018, doi: 10.1007/s11431-017-9175-3.
[107] Y. Tian, J. Shen, C. Wang, Z. Xing, and X. Wang, “Modeling and performance study of a water-injected twin-screw water vapor compressor,” *Int. J. Refrig.-Rev. Int. Froid*, vol. 83, pp. 75–87, Nov. 2017, doi: 10.1016/j.ijrefrig.2017.04.008.
[108] U. Larsen, O. Sigthorsson, and F. Haglind, “A comparison of advanced heat recovery power cycles in a combined cycle for large ships,” *Energy*, vol. 74, pp. 260–268, Sep. 2014, doi: 10.1016/j.energy.2014.06.096.
[109] B. Deng, Q. Tang, and M. Li, “Study on the steam-assisted Brayton air cycle for exhaust heat recovery of internal combustion engine,” *Appl. Therm. Eng.*, vol. 125, pp. 714–726, Oct. 2017, doi: 10.1016/j.applthermaleng.2017.07.039.
[110] “Temperature of Ocean Water - Windows to the Universe.” [Online]. Available: https://www.windows2universe.org/?page=/earth/water/temp.html. [Accessed: 10-Oct-2018].
[111] M. T. Mito, M. A. Teamah, W. M. El-Maghlany, and A. I. Shehata, “Utilizing the scavenge air cooling in improving the performance of marine diesel engine waste heat recovery systems,” *Energy*, vol. 142, pp. 264–276, Jan. 2018, doi: 10.1016/j.energy.2017.10.039.
[112] R. Scaccabarozzi, M. Tavano, C. M. Invernizzi, and E. Martelli, “Comparison of working fluids and cycle optimization for heat recovery ORCs from large internal combustion engines,” *Energy*, vol. 158, pp. 396–416, Sep. 2018, doi: 10.1016/j.energy.2018.06.017.